Accepted Manuscript
Version of record at: https://doi.org/10.1063/5.0091699

A three-dimensional numerical model for the motion of liquid drops by the particle finite element method

Elaf Mahrous,[1, a)] R. Valéry Roy,[2, b)] Alex Jarauta,[3, c)] and Marc Secanell[3, d)]
[1)]*Corresponding author; Department of Mechanical Engineering, Jubail Industrial College, Jubail Industrial City 31961, Saudi Arabia*
[2)]*Department of Mechanical Engineering, University of Delaware, Newark, DE 19716, USA*
[3)]*Energy Systems Design Lab (ESDLab), University of Alberta, Edmonton, AB T6G 2G8, Canada*

Analysis of drop spreading and sliding on solid substrates is critical for many industrial applications, such as microfluidic devices, cooling towers, and fuel cells. A new three-dimensional model is proposed for droplet dynamics. Its numerical solution is obtained by the particle finite element method, based on an updated Lagrangian framework to accurately track the deformation of the droplet. The model hinges on boundary conditions at the solid-liquid interface to account for viscous dissipation and retention forces. These conditions are essential to obtain mesh-independent solutions and a realistic spatio-temporal evolution of the droplet deformation. Several numerical simulations are performed to assess the performance of the model for spreading and sliding drops, and results are compared to experimental data found in the literature. Good agreement is obtained with the available data. Simulations performed in two dimensions show striking discrepancies with the experimental data, thus demonstrating the need for three-dimensional simulations.

Keywords: Droplet spreading. Droplet sliding. Surface tension. Lagrangian. Young's stress. Wetting. Capillary wavelength. PFEM.

I. INTRODUCTION

There are numerous computational studies in the literature for modeling droplet dynamics[1–4]. The number of publications continues to increase every year due to the relevance of this field in countless industrial applications[5–7], e.g., water transport in fuel cell porous media[8–11] and gas channels[12,13], air-water heat exchange in cooling towers[14,15], blood drop dynamics within biomedical devices[16,17], and self-cleaning applications, such as on solar panels[18,19].

The driving forces in the above-mentioned applications are capillary effects, gravity, and, in some of the applications, the drag force exerted by an external airflow. From a modeling perspective, numerical models for droplet dynamics are confronted with several challenges: air-water interface tracking[20,21], characterization of the interfacial solid-liquid forces[22,23], regularization of the contact line singularity[24–26], mesh-independence of the solution[24,25,27,28], and time step reductions due to the propagation of capillary waves[2,20].

Most drop dynamics models found in the literature are based on simplifying assumptions based on quasi-static or axisymmetric conditions[29–31]. In the majority of real-life applications, however, drops experience large asymmetric deformations under the effect of gravity and/or external shear flow[20,32,33]. Such simplifications are not acceptable for such physical conditions as i) liquid drop injection, ii) liquid drop sliding, or iii) two-phase flow, which are of interest in this work.

Many models found in the literature have been proposed for the regularization of the contact line singularity. Models based on the lubrication theory have low computational cost[34], but are limited to small contact angles. Other numerical models have been presented to include hydrophobic effects, however the contact angle condition is based on a static contact angle value[35–37], which is physically unacceptable in most dynamic conditions. This can be addressed by models which include a dynamic contact angle condition[2,12], along with a slip boundary condition imposed at the moving contact line. This leads to non-physical results due to the absence of energy dissipation at the contact line. This issue was resolved by several models that include a dissipative force term at the solid-liquid interface[25,38–40], and still produce mesh-independent solutions[41]. A novel formulation based on a moving mesh is proposed in ref.[41], with the advantage of accurate tracking of the evolution of the liquid domain boundary. However, the model is limited to two-dimensional analysis. A model for contact line dynamics using a combination of hydrodynamics and molecular kinetic theory in a three-dimensional enriched finite element/level set framework has been recently proposed by Hashemi *et al.*[11,42]. More details on the modeling challenges of wetting phenomena can be found in[43].

The sliding of droplets on solid substrates due to the action of gravity or external gas flow has also been considered in the past. Some analytical models have been proposed[44,45], however they rely on simplifying assumptions. For instance, the model of ElSherbini and Jacobi[44] does not consider hydrophobic surfaces with advancing contact angles larger than 115°. Several numerical models have been developed to predict contact line pinning and drop motion employing the level set (LS) method[46], the volume of fluid-continuous surface force (VOF-CSF) approach[47], or the Arbitrary Lagrangian–Eulerian (ALE) formulation[48]. However, all the above-mentioned models are limited to

---

[a)] Electronic mail: mahrouse@ucj.edu.sa
[b)] Electronic mail: vroy@udel.edu
[c)] Electronic mail: jarautaa@ualberta.ca
[d)] Electronic mail: secanell@ualberta.ca

Accepted Manuscript
Version of record at: https://doi.org/10.1063/5.0091699

two-dimensional analysis, thus ignoring out-of-plane forces. Moreover, these models lack a thorough experimental validation.

An alternative approach based on the particle finite element method (PFEM) has been recently developed by the authors, thus far limited to two dimensions in Cartesian coordinates[26]. Two-dimensional droplet models cannot adequately produce axisymmetric drop in Cartesian coordinates, and replicate the full shape of sliding drops. Therefore, in order to successfully predict their temporal evolution, geometric characteristics, such the mean curvature, the contact line perimeter, and the solid-liquid interfacial area, had to be normalized in our previously proposed 2D model[26,41]. This article aims at extending our 2D drop dynamics model to 3D in order to remedy the issues discussed above. In addition to predicting the actual geometric characteristics of the drop, the model should also estimate the temporal evolution of both its spreading rate and its dynamic contact angle. Likewise, the model should be capable of providing the steady-state velocity of a sliding drop.

The main advantage of PFEM is its inherent ability to accurately track the air-water interface, without experiencing numerical diffusion and the need of interface reconstruction methods. Furthermore, the numerical model is fully implicit in space and time, thus allowing for the use of large time steps. These two advantages are critical for simulations of wetting phenomena[2].

The proposed 3D PFEM-based model extends our two previously published studies[26,41] by developing an algorithm: a) to accurately track the contact line, b) to calculate the contact angle and its the normal/tangential vectors, which are necessary to impose the boundary conditions, and c) to create or delete nodes at the contact line and the liquid-solid interface to avoid mesh deterioration. Experimental data in the literature is leveraged to validate the model and assess the discrepancies between the two- and three-dimensional treatments of droplets. The paper is organized as follows: Section II describes the mathematical model governing drop spreading, with attention given to the dissipative forces acting on the solid-liquid interface. This section also introduces the 3D sliding model under the effect of gravity, and describes its numerical implementation. Section III includes several numerical examples, as well as the experimental validation for the 3D spreading and sliding models under a wide variety of fluid properties, drop sizes, and physicochemical conditions.

II. PHYSICAL MODEL

A. Governing equations

Let Ω represent a liquid drop in contact with a solid substrate, as shown in Fig. 1. The boundary of the domain is divided into three regions $\partial\Omega = \Gamma_I \cup \Gamma_S \cup \partial\Gamma$. Γ_S represents the domain boundary corresponding to the liquid in contact with the substrate, excluding the contact line, Γ_I corresponds to the drop's free-surface, and $\partial\Gamma$ represents the contact line.

The governing equations for the liquid phase are the momentum and mass conservation equations. The fluid is assumed to be incompressible and Newtonian. Accordingly, the governing equations are expressed as follows[2,20]:

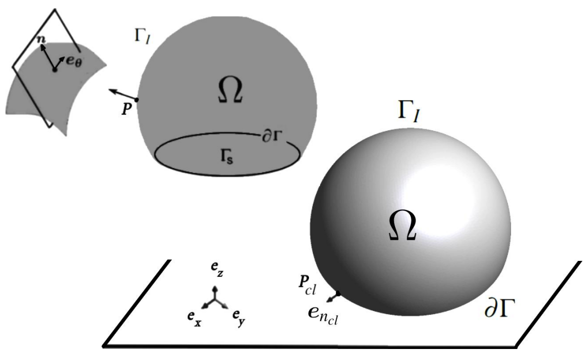

FIG. 1. Schematic representation of the 3D Lagrangian domain.

$$\rho \frac{D\boldsymbol{v}}{Dt} - \mu\nabla\cdot\left(\nabla\boldsymbol{v} + \nabla^T(\boldsymbol{v})\right) + \nabla p = \rho\boldsymbol{g} \qquad \text{on } \Omega \tag{1}$$

$$\nabla\cdot\boldsymbol{v} = 0 \qquad \text{on } \Omega \tag{2}$$

where ρ is the fluid density, $\frac{D\boldsymbol{v}}{Dt} = \frac{\partial\boldsymbol{v}}{\partial t} + \boldsymbol{v}\cdot\nabla\boldsymbol{v}$ is the total material derivative, $\boldsymbol{v}$ is velocity, t is time, μ is the fluid dynamic viscosity, p is pressure, and $\boldsymbol{g}$ is the gravitational acceleration. Note that the Lagrangian formulation is adopted and, thus, the nonlinear convective term is absent in the numerical treatment of Eq. (1)[49].

B. Boundary conditions at the free-surface Γ_I

At the free-surface, Γ_I, a Cauchy stress boundary condition in the normal direction is applied corresponding to the surface tension force:

$$\boldsymbol{f}_{\Gamma_I} = \boldsymbol{\sigma}\boldsymbol{n} = \gamma\kappa_H\boldsymbol{n} \qquad \text{at } \Gamma_I \tag{3}$$

where $\boldsymbol{f}_{\Gamma_I}$ is the surface tension force, $\boldsymbol{\sigma}$ is the Cauchy stress tensor, $\boldsymbol{n}$ is the outer unit normal to Γ_I (see Fig. 1), γ is the surface tension coefficient, and κ_H is the mean curvature of the free-surface. The Cauchy stress tensor $\boldsymbol{\sigma}$ is expressed as:

$$\boldsymbol{\sigma} = -p\mathbb{I} + \mu(\nabla\boldsymbol{v} + \nabla^T\boldsymbol{v}) \tag{4}$$

According to eq. (3), the normal stress is balanced by the surface tension force[20,50,51]. Decomposing eq. (3) into normal and tangential components yields:

$$\boldsymbol{n}\cdot(\boldsymbol{\sigma}\boldsymbol{n}) = \gamma\kappa_H \qquad \text{at } \Gamma_I \tag{5}$$

and

$$\boldsymbol{e}_\theta\cdot(\boldsymbol{\sigma}\boldsymbol{n}) = 0 \qquad \text{at } \Gamma_I \tag{6}$$

where $\boldsymbol{e}_\theta$ represents any unit vector tangent to surface Γ_I (Fig. 1). Assuming a stationary exterior fluid and substitut-

Accepted Manuscript
Version of record at: https://doi.org/10.1063/5.0091699

ing eq. (4) into eq. (5) yields:

$$p - \mu \boldsymbol{n} \cdot ([\nabla \boldsymbol{v} + \nabla^T \boldsymbol{v}]\boldsymbol{n}) = \gamma \kappa_H \qquad \text{at } \Gamma_I \tag{7}$$

$$\mu \boldsymbol{e}_\theta \cdot ([\nabla \boldsymbol{v} + \nabla^T \boldsymbol{v}]\boldsymbol{n}) = 0 \qquad \text{at } \Gamma_I \tag{8}$$

Note that the viscous stress term projected on the normal direction in Eq. (7) can be neglected[12].

C. Forces acting on the contact line, $\partial\Gamma$

At the contact line, an effective slip boundary condition is applied in terms of an effective slip coefficient which accounts for i) the capillary effect (ζ), ii) normal stress coefficient (β_n), and iii) Navier-slip coefficient (β_s). This effective slip boundary condition is defined in terms of a dissipative force $\boldsymbol{f}_{\partial\Gamma}$ applied to the contact line, and is proportional to the velocity of the contact line[25,40,52,53] as follows:

$$\boldsymbol{f}_{\partial\Gamma} = -\beta_{\partial\Gamma} \boldsymbol{v} \qquad \text{at } \partial\Gamma \tag{9}$$

where $\beta_{\partial\Gamma}$ is the effective slip coefficient at the contact line, and $\boldsymbol{v}$ is the slip velocity of the fluid at the contact line.

As the drop starts to move, the velocity of the contact line can be related to the Young's stress acting on it as follows:

$$\boldsymbol{v} \cdot \boldsymbol{e}_{n_{cl}} \propto \gamma(\cos\theta_e - \cos\theta_d) \tag{10}$$

where θ_e is the static contact angle, θ_d is the dynamic contact angle, and $\boldsymbol{e}_{n_{cl}}$ is the unit normal vector at the point P_{cl} of the contact line, see Fig. 1. The proportionality coefficient between the contact line velocity and Young's stress is the effective slip boundary condition defined as follows[40]:

$$\beta_{\partial\Gamma}(\boldsymbol{v} \cdot \boldsymbol{e}_{n_{cl}}) = \gamma(\cos\theta_e - \cos\theta_d) \tag{11}$$

where $\beta_{\partial\Gamma}$ is the effective slip coefficient, and is defined as[24,25,39,40,52–56]:

$$\beta_{\partial\Gamma} = \zeta + \beta_S|_{\partial\Gamma} + \beta_n \tag{12}$$

where ζ is the capillary effect coefficient (see reference[41] for more details), $\beta_S|_{\partial\Gamma}$ is the Navier-slip coefficient, and β_n is the normal stress coefficient. They are expressed, according to Jiang's model[41,57], as follows:

$$\zeta = \frac{\gamma}{\boldsymbol{v} \cdot \boldsymbol{e}_{n_{cl}}}(\cos\theta_e + 1)\ \tanh\left(4.96 Ca^{0.702}\right) \tag{13}$$

$$\beta_S|_{\partial\Gamma} = \frac{1}{\boldsymbol{v} \cdot \boldsymbol{e}_{n_{cl}}} \mu \nabla(\boldsymbol{v} \cdot \boldsymbol{e}_{n_{cl}}) \cdot \boldsymbol{e}_z \tag{14}$$

$$\beta_n = \frac{1}{\boldsymbol{v} \cdot \boldsymbol{e}_{n_{cl}}} \mu \nabla(\boldsymbol{v} \cdot \boldsymbol{e}_{n_{cl}}) \cdot \boldsymbol{e}_{n_{cl}} \tag{15}$$

By accounting for the contributions of the capillary effects, the Navier-slip as well as the normal stresses in eq. (12), the coefficient $\beta_{\partial\Gamma}$ is used to obtain the total dissipative force and to apply the boundary condition defined by eq. (9).

As the drop starts to slide, the effect of a retention force acting on the contact line must be included. The magnitude of this retention force is known to be a function of i) the drop size, ii) the aspect ratio of the wetting perimeter, iii) the surface tension coefficient, and iv) the contact angle hysteresis, as follows[44,48,58–61]:

$$F_{retention} = \gamma k a(\cos\theta_R - \cos\theta_A) \tag{16}$$

where k is a function of the aspect ratio of the drop footprint, a is the wetting radius of the liquid drop, θ_R is the receding contact angle, and θ_A is the advancing contact angle. The parameters θ_A and θ_R are the maximum and minimum contact angles along the contact line, respectively[41,62]. For a liquid drop sliding under the effect of gravity, the retention force opposes the effect of the gravitational force.

The effect of the retention force is added to eqs. (9)-(15). Accordingly, for the case of sliding liquid drop, an additional coefficient $\beta_{\partial\Gamma}$ is defined as follows:

$$\beta_{\partial\Gamma} = \zeta + \beta_n + \beta_S + \beta_{retention} \tag{17}$$

The coefficient $\beta_{retention}$ accounts for the effect of the retention force and it is given by:

$$\beta_{retention} = \frac{\gamma k a}{\boldsymbol{v} \cdot \boldsymbol{e}_{n_{cl}}}(\cos\theta_R - \cos\theta_A) \tag{18}$$

D. Forces acting on the solid-liquid interface away from the contact line, Γ_S

At the solid-liquid interface excluding the contact line, Γ_S, the applied boundary condition is obtained by projecting the Cauchy stress tensor on the normal direction of Γ_S[25,40]:

$$\boldsymbol{f}_{\Gamma_S} = \boldsymbol{\sigma} \cdot \boldsymbol{e}_z = -\beta_{\Gamma_s} \boldsymbol{v} \qquad \text{at } \Gamma_S \tag{19}$$

where $\boldsymbol{f}_{\Gamma_S}$ and β_{Γ_s} are the dissipative force and the slip coefficient applied at the solid-liquid interface, respectively, and $\boldsymbol{v}$ is the slip velocity of the fluid on the solid-liquid interface. The Navier-slip model is considered in this work, and it corresponds to the viscous dissipation along the solid-liquid interface as the drop deforms[24,40,52,53]. Therefore, the slip coefficient β_{Γ_s} at the solid-liquid interface Γ_S is obtained as follows:

$$\beta_{\Gamma_s} = \beta_s = \frac{1}{\boldsymbol{v}\cdot\boldsymbol{e}_{n_{cl}}}\mu\nabla(\boldsymbol{v}\cdot\boldsymbol{e}_{n_{cl}})\cdot\boldsymbol{e}_z \tag{20}$$

Eq. (20) is used in combination with eq. (19) to apply the boundary condition at the solid-liquid interface.

E. Mesh size and time step criteria

1. Droplet spreading

As the drop spreads, capillary waves are generated at the contact line and propagate from $\partial\Gamma$ towards Γ_I[63,64]. Numerically, the mesh size at the contact line is restricted by the wavelength of the capillary wave propagation. The values of the mesh size, h, and the time step, Δt, are estimated as follows[41]:

$$h = \frac{\gamma}{2\rho v_{max}^2} \tag{21}$$

and

$$\Delta t_{cap} \leq \sqrt{\frac{2}{\pi}\frac{\gamma}{4\rho|v_{max}^3|}} \tag{22}$$

where v is the magnitude of the slip velocity of the fluid on the solid-liquid interface, i.e. $v = \|\boldsymbol{v}\|$, and v_{max} is the magnitude of the maximum slip velocity of the liquid at the contact line.

2. Droplet sliding

The adopted mesh size, h, is estimated as a function of the wetting radius, a, as follows[26]:

$$h \sim \frac{a}{10} \tag{23}$$

Our previous numerical work on drop spreading demonstrated that the implementation of the proposed model results in physically and quantitatively acceptable behavior.

The constraint for choosing the time step is derived by guaranteeing the range of applicability of Jiang's model, that is $0 < Ca \leq 0.03$. The time step criterion is calculated based on the Weber number (We) defined as[65]:

$$We = \frac{\rho R v_{max}^2}{\gamma} \tag{24}$$

where R is the radius of the drop. The time step can be calculated as follows:

$$\Delta t \leq \begin{cases} \sqrt{\frac{2}{\pi}\frac{\gamma}{4\rho|v_{max}^3|}} & \text{for } We \geq 1 \\ \frac{CFL}{\frac{|v_{max}|}{h}+\frac{2\mu}{h^2}} & \text{for } We < 1 \end{cases} \tag{25}$$

where CFL is the Courant-Friedrichs-Lewy number. The range of CFL is practically found to be between 0.5 and 0.9. In 3D, the computations become unwieldy for smaller mesh sizes and time steps. Thus, for free-surface problems, i.e., $We < 1$, we will take advantage of the following time step criteria devised by Sussman and Ohta[66]:

$$\Delta t_{crit} \leq \sqrt{\frac{(\rho_L+\rho_g)h^3}{\gamma(2\pi)^3}} \tag{26}$$

F. Discretized governing equations

The particle finite element method (PFEM)[49,67–71] is used in the present work to discretize eqs. (1) and (2) in space. The PFEM adopts the updated Lagrangian description of the governing equations. The fluid domain is discretized by a standard finite element mesh. The nodes can be interpreted as immaterial particles that move according to their velocity. At each computational step, the domain deforms. Thus, in order to avoid excessive mesh degradation, re-meshing is performed at each time step using Delaunay triangulation. For droplet dynamics problems, the re-meshing procedure ensures that the domain boundaries are reconstructed in accordance with the new nodal positions obtained on the velocity field and time step. Linear interpolation functions for both velocity and pressure are used over tetrahedral elements. In the present implementation, the discretization in time is performed using the Backward Difference Formula of second-order (BDF2)[72]. This method is an unconditionally stable time integration scheme with second-order accuracy. However, for the sake of clarity, it is expressed here using the Backward-Euler scheme[49]. Given a known $\bar{\boldsymbol{v}}_n$ and $\bar{p}_n$ at time t_n (overbarred letters represent quantities obtained after space discretization), the values of these variables at time t_{n+1} are obtained by solving the following governing equations in their residual form:

$$\bar{\mathbf{r}}_m = \bar{\boldsymbol{F}} + \bar{\boldsymbol{F}}_{st} + \bar{\boldsymbol{F}}_{\partial\Gamma} + \bar{\boldsymbol{F}}_{\Gamma_S} - \left(\boldsymbol{M}\frac{\bar{\boldsymbol{v}}_{n+1}-\bar{\boldsymbol{v}}_n}{\Delta t} + \mu\boldsymbol{L}\bar{\boldsymbol{v}}_{n+1} + \boldsymbol{G}\bar{p}_{n+1}\right) \tag{27}$$

$$\bar{\mathbf{r}}_c = \boldsymbol{D}\bar{\boldsymbol{v}}_{n+1} \tag{28}$$

where the nonlinear dependence on the unknown configuration, $\boldsymbol{X}_{n+1}$, is dealt with by using a Newton method. Δt is the time step; $\boldsymbol{M}$, $\boldsymbol{L}$, $\boldsymbol{G}$, and $\boldsymbol{D}$ are the mass, Laplacian, gradient, and divergence matrices, respectively; and $\bar{\boldsymbol{F}}$, $\bar{\boldsymbol{F}}_{st}$, $\bar{\boldsymbol{F}}_{\partial\Gamma}$, and $\bar{\boldsymbol{F}}_{\Gamma_S}$ are the vectors of the external forces, the surface tension force, the dissipative force acting on the contact line, and the dissipative force acting on the solid-liquid interface away from the contact line, respectively. These vectors are evaluated at time step t_{n+1}. Local cell matrices and vectors are defined in A.

Eqs. (27) and (28) are then linearized, and the system is solved iteratively. The resulting linearized system of governing equations reads:

$$\begin{pmatrix} \boldsymbol{M}\frac{1}{\Delta t}+\mu\boldsymbol{L}+\boldsymbol{H}_{st} & \boldsymbol{G} \\ \boldsymbol{D} & 0 \end{pmatrix}\begin{pmatrix} \delta\bar{v} \\ \delta\bar{p} \end{pmatrix} = \begin{pmatrix} \bar{\mathbf{r}}_m \\ \bar{\mathbf{r}}_c \end{pmatrix} \qquad (29)$$

where $\boldsymbol{H}_{st}$ originates from the linearization of the surface tension force term, $\bar{\boldsymbol{F}}_{st}$. This term is responsible for the implicit treatment of the surface tension, and it allows for the use of large time steps. The derivation of this term, as well as the stabilization terms, can be found in reference[2]. The linear velocity-pressure elements used in our model do not fulfill the compatibility condition[73] and therefore pressure must be stabilized. In this work, the algebraic sub-grid scales (ASGS)[74–76] stabilization technique is used (see reference[2] for details). Once the system in eq. (29) has been solved for $\delta\bar{\boldsymbol{v}}$ and $\delta\bar{p}$, the primary variables are updated according to $\bar{\boldsymbol{v}}^{k+1}_{n+1} = \bar{\boldsymbol{v}}^{k}_{n+1} + \delta\bar{\boldsymbol{v}}$ and $\bar{p}^{k+1}_{n+1} = \bar{p}^{k}_{n+1} + \delta\bar{p}$, where k is the nonlinear iteration index, until convergence is achieved. As a final step, the nodal position in the moving mesh is updated according to the employed time integration scheme. In case of Backward Euler integration, this yields $\boldsymbol{X}^{k+1}_{n+1} = \boldsymbol{X}_n + \Delta t\ \bar{\boldsymbol{v}}^{k+1}_{n+1}$. The solution algorithm is further illustrated in B.

G. Numerical implementation

1. *Mesh enhancements in 3D*

One of the main challenges to extend our previous two-dimensional models[26,41] to three dimensions is the treatment of the discretized geometry. In the PFEM scheme, the initial configuration of the domain consists of mesh nodes which are treated as particles. Mathematical information and physical quantities are assigned to each node. The finite element mesh is generated and connected by a Delaunay triangulation/tetrahedralization[77,78]. Mesh connectivity is the main role of the Delaunay triangulation/tetrahedralization. However, it does not recover the domain boundaries. To do so, the alpha shape technique is implemented in our PFEM scheme[79]. The alpha shape technique is a key ingredient to determine the boundary in problems involving free surface flows.

For wetting problems, an accurate representation of the contact line and the liquid/solid interface is paramount for the correct application of the boundary conditions. Therefore, nodes may have to be added or deleted depending on the problem. Let us consider a droplet in contact with a hydrophobic surface, with an initial geometry in the form of a cube or prism (see Fig. 5). Since the substrate is hydrophobic, the nodes at the contact line will move inwards in order to fulfill the contact angle condition. However, the nodes that are in contact with the solid substrate (marked in red in Fig. 2) but do not belong to the contact line might have a zero velocity. Thus, when nodes at the contact line approach these *static* nodes, the elements may become distorted. In order to avoid this problem, a new routine is implemented in the re-meshing function that deletes a static node located at a distance to a contact line node smaller than $0.5h$, where h is the initial mesh size (more details about PFEM criterion for nodal addition/removal can be found in reference[78]). This can be observed, for example, in Fig. 2, where a static node is deleted after the contact line nodes are at a distance which is below a certain threshold value.

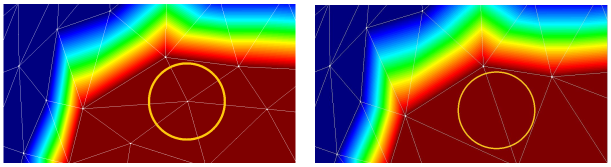
(a) (b)

FIG. 2. Node deletion for problems where contact line nodes approach other nodes at the liquid/solid interface (view from below, nodes at the liquid/solid interface are noted in red, which are contained in the xy-plane in Fig. 1): (a) before deleting a node, and (b) after deleting a node.

The opposite situation occurs with droplets in contact with hydrophilic substrates. In this case, the nodes at the contact line move outwards. Therefore, if two nodes of the contact line are located at a distance from a static node greater than $2h$, where h is the initial mesh size, a new node is inserted in the considered face. Figure 3 shows the resulting mesh after inserting a node in an element's face.

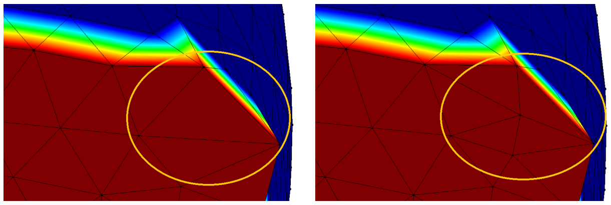
(a) (b)

FIG. 3. Node addition for problems where contact line nodes move away from other nodes at the liquid/solid interface (view from below, nodes at the liquid/solid interface are noted in red, which are contained in the xy-plane in Fig. 1): (a) before adding a node, and (b) after adding a node.

An additional problematic situation observed in droplets in contact with hydrophilic substrates is when the distance between two nodes of the contact line is greater than some threshold value. In this case, a new node is inserted in the segment between these two nodes. Once the computational mesh is created, the normal vector at the contact line nodes and the contact angle are obtained. Fig. 4 shows the resulting mesh after inserting a node in an element's segment.

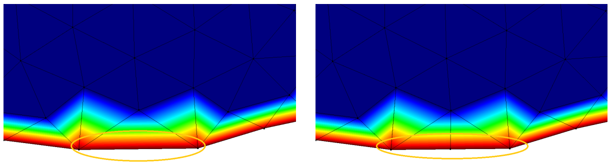

(a) (b)

FIG. 4. Node addition at the contact line where two contact line nodes move away from each other (view from above, nodes at the liquid/solid interface are noted in red, which are contained in the *xy*-plane in Fig. 1, and nodes in blue represent the liquid/gas interface): (a) before adding a node, and (b) after adding a node.

TABLE I. Input parameters used in the solver for monolithic scheme

Parameter	Value
Newton solver max number of iterations	500
Linear solver iterative tolerance	10^{-6}
Linear solver max number of iterations	5000

2. *Implementation and numerical details*

Table I shows the input parameters used in the model. Implementation is done using the updated Lagrangian fluid (ULF) application within Kratos Multi-Physics, a C++ object-oriented finite element open source framework[80]. The discretization in time is performed using the Backward Difference Formula of second-order (BDF2)[72]. A quasi-Newton method is used to solve Eqs. (27) and (28). The resulting system of equations is solved using the bi-conjugate gradient stabilized method (BiCGStab). This method is known for its ability to solve non-symmetric matrices with improved rate of convergence and low computational cost when compared to other iterative methods, such as conjugate gradient squared (CGS), bi-conjugate gradient (BiCG) or generalized method of minimum residuals (GMRES)[81].

Results are obtained using a Linux operating system with an Intel® Core™ i7-8750H CPU @ 2.20GHz, 12 processors, and 32 GB RAM. Depending on the droplet size, simulations took between 1 and 4 hours.

III. RESULTS AND DISCUSSION

A. Droplet spreading

1. *Spreading of arbitrary-shaped droplets*

The effects of adding a dissipative force on a moving contact line are assessed in this example. The spreading motion is simulated for different initial arbitrarily-shaped drops. This example demonstrates the success of our 3D drop dynamics model in i) regularizing the contact line singularity, ii) tracking the deformed boundaries, and iii) reaching the equilibrium configuration. The domain initial configuration is set to be a prismatic (nominal) drop of height $H = 0.02$ cm and of two different cross-sections: (a) a square of side length 0.05 cm, and b) a triangle of 0.05 cm per side. The considered substrates are (i) a kapton-coated surface with static contact angle value of 75 degrees[82] (hydrophilic), and (ii) a polytetrafluoroethylene (PTFE)-coated surface with static contact angle of 108 degrees[83] (hydrophobic).

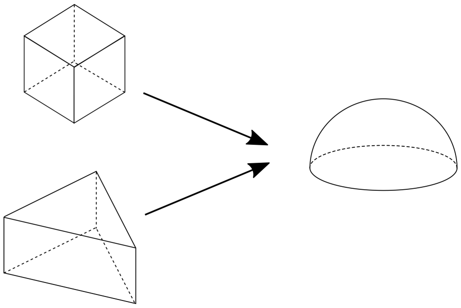

FIG. 5. Initial and steady-state configurations for sessile drops starting with two different prismatic initial configurations.

The driving forces acting on the drop are those of surface tension and gravity directed normal to the substrate. Fluid density, viscosity and surface tension coefficient are set to $\rho = 1000$ kg m^{-3}, $\mu = 8.90 \times 10^{-4}$ kg m^{-1} s^{-1}, $\gamma = 0.072$ N m^{-1}, respectively, representative of a water drop. Initial pressure in the liquid is set to $p_0 = 0$ Pa. The domains of the squared-prismatic and triangular-prismatic droplets are meshed using tetrahedral elements of sizes 0.003 cm and 0.002 cm, respectively, and a time step size of $\approx 1 \times 10^{-6}$ seconds is used. The predicted drop geometry at various times during the simulation is shown in Figure (6).

In both configurations, the steady-state solution is achieved in less than 4 ms. The solution is considered steady-state when the average contact line velocity is zero. Table II shows the obtained value of the contact angle for each configuration and substrate, where θ_{ave} is the node-averaged contact angle. It can be observed that in all cases, the computed relative error was less than 7% for kapton, and 3% for PTFE.

The simulated drops evolved in accordance with the proposed mathematical model and boundary conditions presented in Sec. II, until they successfully reached their equilibrium configurations. Our numerical results converged to the equilibrium configuration of a smooth spheroidal drop with the prescribed static contact angle, regardless of the initial shape.

2. *Equilibrium configuration for viscous drops on a smooth surface*

Replicating the exact shape of a drop is the ultimate goal of a spreading simulation. In this section, the equilibrium configuration of a viscous drop is examined both in 2D and 3D. We aim at reproducing the experimental work by Abolghasemibizaki *et al.*[84] for viscous glycerol drops on smooth polyethylene terephthalate glycol (PETG) surface.

Two drop sizes of 1.1 and 2.15 mm radii, i.e., 5.6 and 41.6μL respectively, are considered. The gravitational field

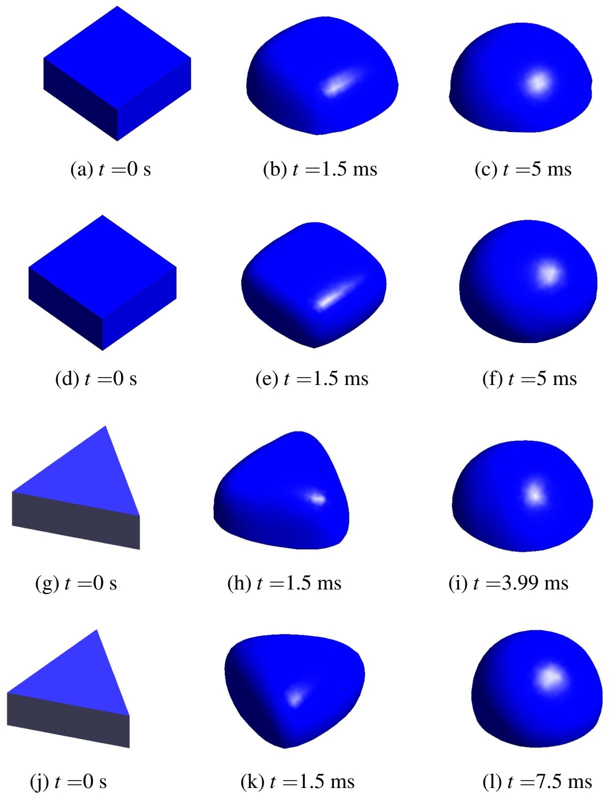
(a) t =0 s (b) t =1.5 ms (c) t =5 ms

(d) t =0 s (e) t =1.5 ms (f) t =5 ms

(g) t =0 s (h) t =1.5 ms (i) t =3.99 ms

(j) t =0 s (k) t =1.5 ms (l) t =7.5 ms

FIG. 6. Spreading evolution for two different initial geometries, on two different substrates: (a)-(c) water droplet of an initial squared-prismatic configuration spreading on kapton substrate, (d)-(f) water droplet of an initial squared-prismatic configuration spreading on PTFE substrate, (g)-(i) water droplet of an initial triangular-prismatic configuration spreading on kapton substrate, and (j)-(l) water droplet of an initial triangular-prismatic configuration spreading on PTFE substrate.

TABLE II. Contact angles values obtained numerically (θ_{ave}) for water drops on kapton and PTFE substrates, and the corresponding error with respect to the prescribed equilibrium angle θ_e.

Configuration	Substrate	θ_{ave}, (deg)	Error ($\lvert\theta_{ave}-\theta_e\rvert$) / θ_e, (%)
Square	kapton	79.9	6.5
	PTFE	105.0	2.8
Triangle	kapton	79.3	5.7
	PTFE	104.5	3.2

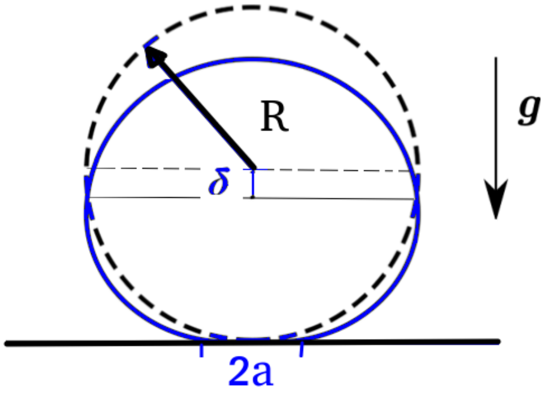

FIG. 7. schematic representation of the initial configuration (dashed line) and the equilibrium configuration (solid line) of a viscous liquid drop[84].

TABLE III. Dimensions of glycerine drops at equilibrium configuration.

Initial radius R, (mm)	δ, eq. (30) (mm)	δ, numerically (2D) (mm)	Difference in δ (2D), %	δ, numerically (3D) (mm)	Difference in δ (3D), %
1.1	0.25	0.2	20.0%	0.23	8.0%
2.15	1.9	1.1	42.1%	1.5	21.1%

acts normal to the flat substrate. The drop is lowered from its center by a value of δ, forming a wetting radius of a (shown in Fig. 7) due to its own weight. At equilibrium, the center of mass displacement, δ, is estimated as[84]:

$$\delta \approx \rho g R^3/\gamma \tag{30}$$

The simulations are performed using the physical properties of glycerol on PETG substrate, θ_e =169.1°. Fluid density, viscosity and surface tension coefficient are set to ρ = 1261 kg m^{-3}, μ = 1.076 kg m^{-1} s^{-1}, γ = 0.0646 N m^{-1}, respectively. The mesh sizes are chosen to be 0.15 and 0.3 mm for the 5.6μL and 41.6μL drops, respectively. The capillary waves at the moving contact line are neglected compared to the dominant surface tension force. Hence, the time step is chosen based on the implicit criteria devised by Jarauta *et al.*[2] as $\Delta t \approx 5 \times 10^{-3}$ s.

Figure 8 show the equilibrium configuration of each drop. Figure 8(f) shows a transparent view, indicating both the distribution and the total number of particles (~2,808 mesh nodes) for the 2.15 mm radius drop. The mesh is refined at the contact line and, thus, crude meshing is avoided.

In both cases, i.e., for 1.1 mm and 2.15 mm radii drops, the drop profiles in 3D are found to be in better agreement with the experimental profiles than in 2D. The corresponding change in δ is shown in Table III for each drop size. As indicated by eq. (30), the value of δ increases as the drop size increases. The error between numerical and experimental values of δ increases as the weight of the drop increases. The 3D model, however, provides more reliable results than the 2D model, especially for larger drops. This is hypothesized to be due to the limitation of 2D simulations in Cartesian coordinates to properly replicate the full shape of the drop.

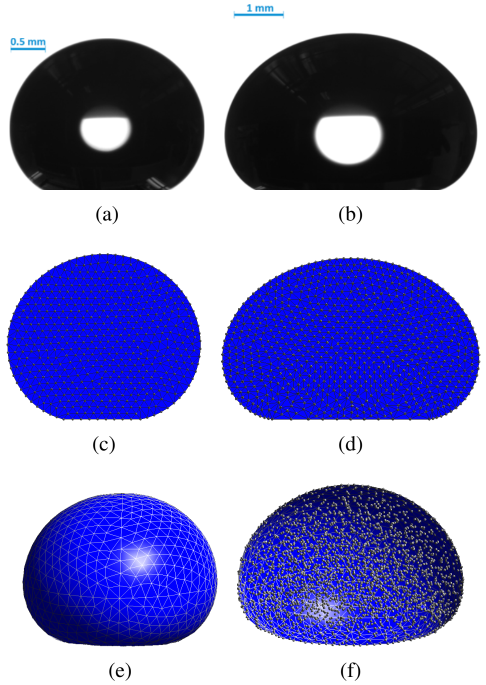

(a) (b) (c) (d) (e) (f)

FIG. 8. Equilibrium configuration for a 1.35 mm-radius (left) and 2.3 mm-radius (right) glycerol drop on smooth PETG surfaces observed (a)-(b) experimentally, (reproduced from [84], with the permission of AIP Publishing), (c)-(d) numerically in 2D, and (e)-(f) numerically in 3D.

3. Water drop spreading on a hydrophobic substrate

In this numerical study, we simulate the sessile water drop deposition experiments performed by Bird *et al.*[85]. In their study, a drop was placed on the triethoxysilane substrate through a needle. The drop contacts the substrate at a diameter of 1.64 mm, and was allowed to spread spontaneously over the substrate until equilibrium was reached, i.e., until the value $\theta = \theta_e = 117^\circ$ is reached. Spreading displacement (a) was measured over the time of spreading.

In order to reproduce this experiment, a drop is placed on the substrate with an initial radius $R = 0.82$ mm, contact angle nearly equal to 180°, and liquid pressure of $p_0 = 0$ Pa. The drop is allowed to deform until equilibrium is achieved, i.e., $\theta_e = 117^\circ$. Fluid density, viscosity and surface tension coefficient are set to $\rho = 1000$ kg m^{-3}, $\mu = 8.90\times10^{-4}$ kg m^{-1} s^{-1}, $\gamma = 0.072$ N m^{-1}, respectively. The time step and mesh size are chosen to be $h = 8\times10^{-5}$ m and 10^{-7} s, respectively.

Fig. 9 and Table IV show that the experimental and numerical profiles are in very good agreement. In addition, the time evolution of the spreading radius is found to replicate the experimental data. Initial deviation between the numerical and experimental data is observed due to the difference in the initial drop configuration and spreading conditions, i.e., a drop with a spherical configuration was relaxed experimentally while it was attached to a needle.

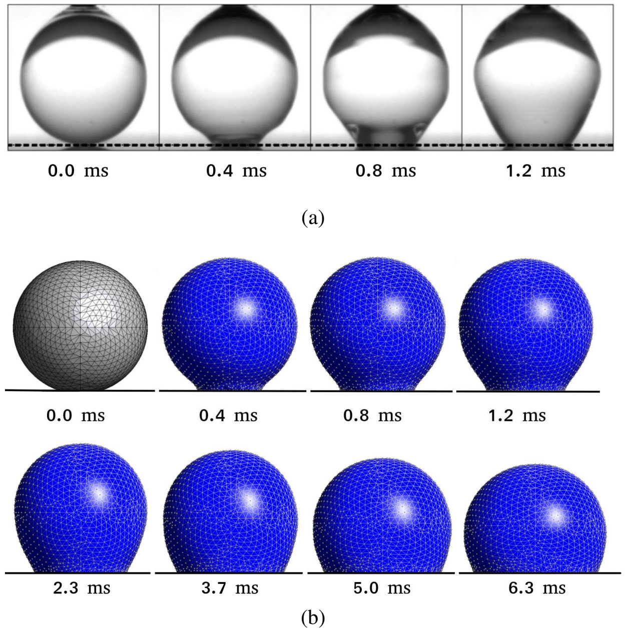

(a)

(b)

FIG. 9. Water drop of radius 0.82 mm spreading on triethoxysilane, for $0 < t \leq 1.2$ ms, with a dominant capillary wave propagation at the contact line (a) experimentally[85], (reproduced with permission from J. Phys. Rev. Lett. 100, 234501 (2008). Copyright 2008 American Physical Society), and (b) numerically.

TABLE IV. Comparison between numerical and experimental spreading evolution for a water drop of 0.82 radius spreading on a triethoxysilane substrate (based on Fig. 9).

Time, (ms)	Experimental spreading diameter $(2a)$, (mm)	Numerical spreading diameter $(2a)$, (mm)	Error in $2a$, (%)
0.4	0.705	0.77	9.2 %
0.8	0.82	0.9	9.75 %
1.2	0.9	0.93	3.3 %

Our numerical results of the spreading radius evolution can be further compared with a scaling law obtained experimentally. Bird *et al.*[85] showed that the spreading radius evolution, $r(t)$, of a water drop deposited on a triethoxysilane substrate scales to the following power law (see reference [85] for details):

$$r(t) = 0.7R(t/\tau)^{0.3} \tag{31}$$

where $\tau = (\rho R^3/\gamma)^{1/2}$. The predicted spreading radius using the scaling law (Eq. (31)) and the numerical model (Fig. 9) are shown in Table V. Both results are found to be in good agreement, with an average error of less than 10%.

The inertial regime characterized by the capillary waves can be predicted using the scaling laws [86–88]:

$$\left(\frac{\rho R^3}{\gamma}\right)^{0.5} < T_t < \left(\frac{\rho R^3}{\gamma}\right)^{0.5}\left(\frac{\rho\gamma R}{\mu^2}\right)^{0.125} \tag{32}$$

TABLE V. Comparison between scaled (Eq. 31[85]) and numerical (Fig. 9) spreading evolution for a water drop of radius 0.8 mm spreading on a triethoxysilane substrate.

Time (ms)	Spreading radius, Eq. (31), (mm)	Numerical spreading radius (mm)	Difference (%)
0.8	0.4	0.45	12.5 %
1.2	0.45	0.465	3.3 %
2.3	0.54	0.55	1.9 %
5	0.69	0.7	1.5 %
6.3	0.736	0.74	0.5 %

where T_t is the transition time elapsed between the inertial and viscous regimes. Eq. (32) implies that the inertial regime, T_i, for a water droplet of radius 0.8 mm is in the range of $T_i < 2.7$ ms. The scaled inertial regime is found to be in agreement with Fig. 9, both experimentally[85] and numerically. Inertial-dominated regime, viscous-dominated regime, and transition time interval of different spreading liquid drops were simulated using the PFEM scheme and verified with published experimental studies in our previous work[41].

B. Droplet sliding

Three different experimental scenarios obtained from the published literature are examined to validate the proposed sliding drop model for a variety of liquid and substrate properties. We examine only the steady-state profiles due to the lack of experimental data during the unsteady initial drop motion, which typically lasts a few milliseconds. Our proposed three-dimensional model is further compared with two-dimensional PFEM numerical results published in[26].

1. *Drop on an omniphilic substrate*

We examine the sliding experiment performed by Kim *et al.*[60] for an ethylene glycol drop sliding on an inclined polycarbonate substrate. The drop of volume 29.2 μL slides over the substrate until it reaches its steady-state velocity. An inclination angle of $\alpha = 20°$ is considered. The steady-state velocities were found experimentally to be 1.557×10^{-3} m s^{-1}[60].

The simulation is performed using the physical properties for case #1 of Table VI. The wetting radius is $a = 0.00283$ m (see Fig. 13 in C). Thus, the mesh size and time step are calculated to be $h = 4 \times 10^{-4}$ m and $\Delta t \approx 1 \times 10^{-6}$ s. The Weber number is found to be < 1 for the given steady-state velocity, i.e., 1.557×10^{-3} m s^{-1}[60]. Hence, we are able to utilize eq. (26). Therefore, the time step used here is $\Delta t \approx 8 \times 10^{-5}$ s.

TABLE VI. Physical properties of the sliding liquid drops for different liquid/solid pairs.

Case #	Liquid	Substrate	ρ (kg.m^{-1})	μ (Pa.s)	γ (N.m^{-1})	θ_e (°)	Volume (μL)	α (°)	k
1[60]	ethylene glycol	polycarbonate	1114	0.0209	0.0484	70.2	29.2	20	1.41
2[46]	water	PTFE	997	0.00089	0.0728	120	7.5	60	1.35
3[89]	PEG	smooth glass	1080	0.285	0.0533	34.0	100	27	2.0

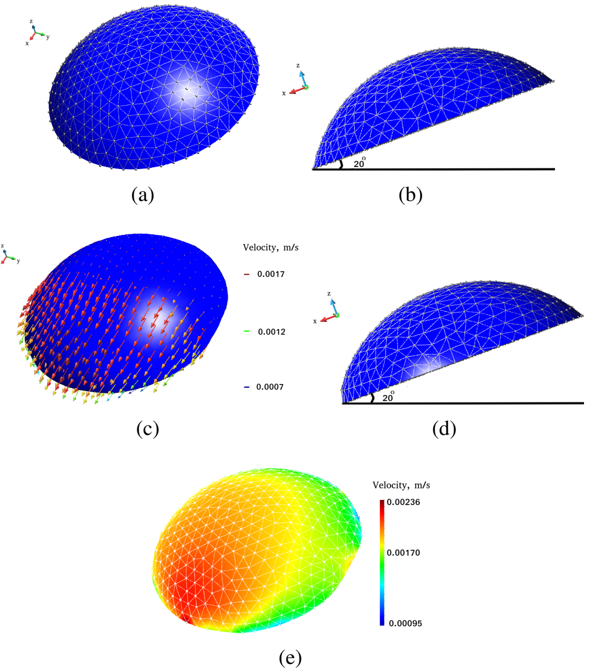

(a) (b) (c) (d) (e)

FIG. 10. Case #1: sliding profiles for EG drop on an omniphilic polycarbonate substrate: (a) initial configuration, (b) initial configuration, side view, (c) steady-state configuration, (d) steady-state configuration, side view, and (e) steady-state velocity profile.

The value of parameter k in the retention force term in equation (16) is chosen by using experimental results for a sliding ethylene glycol sliding drop. It is found to be 1.41[59]. The numerical value of the steady-state velocity is found to be 1.65×10^{-3} m s^{-1}. The error between the experimental and numerical results is found to be $\approx 6\%$, as shown in the first case of Table VII.

Results were also computed using the two-dimensional analog of the problem using the same computational algorithm. The retention force constant used was the one recommended for the two-dimensional approximation in the literature, i.e., $\frac{k}{\pi}$[59]. In this case, the error increases to 19.1% as shown in Table VII.

TABLE VII. Numerical vs. experimental steady-state velocities (u_{ss}) in 2D and 3D.

Case #	Volume (μL)	α (°)	k (3D)	Experimental u_{ss} (m s^{-1})	Numerical (3D) u_{ss} (m s^{-1})	Error in u_{ss} (%)	Numerical (2D) u_{ss} (m s^{-1})	Error in u_{ss} (%)
1	29.2	20	1.41[59]	1.557E-3	1.65E-3	5.97 %	1.26E-3	19.1%
2	7.5	60	1.35[59]	0.12	0.105	12.5 %	0.11	8.3%
3	100	27	2[89]	7.75E-4	8.1E-4	4.52 %	8.7E-4	12.3%

2. *Water drop on a hydrophobic substrate*

The second validation considers the experiments performed by Annapragada *et al.*[46]. In this experiment, a water drop of volume 7.5 μL slides on an inclined PTFE substrate. Under equilibrium condition, the contact angle θ_e is 120°. The drop is sliding on a tilted plate at an inclination angle of 60°. The steady-state sliding velocity was experimentally found to be 0.12 m s^{-1}.

Using the physical properties for case #2 of Table VI, the simulation is performed with corresponding mesh size of $h = 1.1 \times 10^{-4}$ m. The value of the parameter k was found experimentally to be 1.35[59]. The limiting time step can be predicted by assuming the steady-state sliding velocities, u_{ss}, based on the experimental results found in[46] to be 0.12 m s^{-1}. We is found to be ≤ 1 and, therefore, the time step used here is $\Delta t \approx 1 \times 10^{-5}$ s (eq. 26).

The error between the experimental and numerical results is found to be $\approx 12.5\%$, as shown in the second case of Table VII. Physically, it has been observed that high contact line velocity leads to higher capillary action[65] and viscous dissipation along the contact line. Due to the nature of the PFEM, minor numerical fluctuations are expected when the mesh nodes are added or deleted, as the domain undergoes large deformation. Mesh addition/deletion is performed at each time step as needed to avoid crude meshing and mesh deterioration.

3. *Viscous drop on an omniphilic smooth substrate*

The last scenario aims to simulate the experimental steady-state velocity obtained by Xu *et al.*[89]. In this experiment, a polyethylene glycol (PEG) drop slides on an omniphilic smooth glass, with contact angle $\theta_e = 34°$. The volume of the drop is 100 μL. The drop slides at an inclination angle of $\alpha = 27°$. The steady-state velocity was experimentally found to be 7.75×10^{-4} m s^{-1}. The value of k is chosen to be 2.0[89].

The simulation is performed using the physical properties for case #3 of Table VI. Adaptive mesh size is used with an initial grid size $h = 9 \times 10^{-4}$ m, and refined to $h = 6 \times 10^{-4}$ m near the boundaries. The time step is set to $\Delta t = 1 \times 10^{-4}$ s.

The numerical value of the steady-state velocity is found to be 8.1×10^{-4} m s^{-1}. As shown in Table VII, the difference between the experimental and numerical results is 4.52%.

The steady-state sliding velocity obtained numerically is

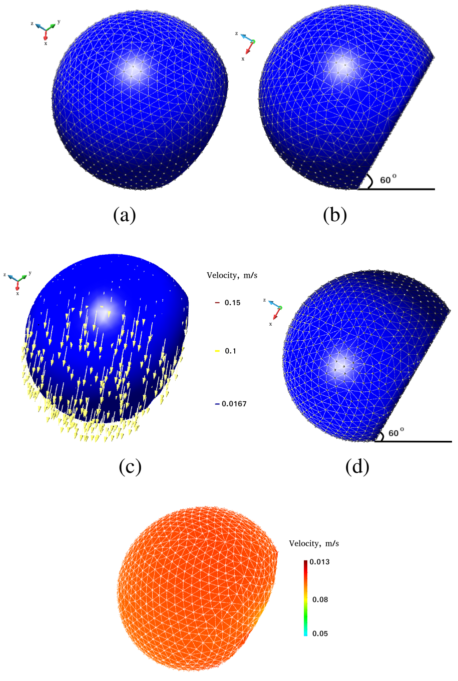

(a) (b)

(c) (d)

(e)

FIG. 11. Case #2: sliding profiles for water drop sliding on PTFE substrate: (a) initial configuration, (b) initial configuration, side view, (c) steady-state configuration, (d) steady-state configuration, side view, and (e) steady-state velocity profile.

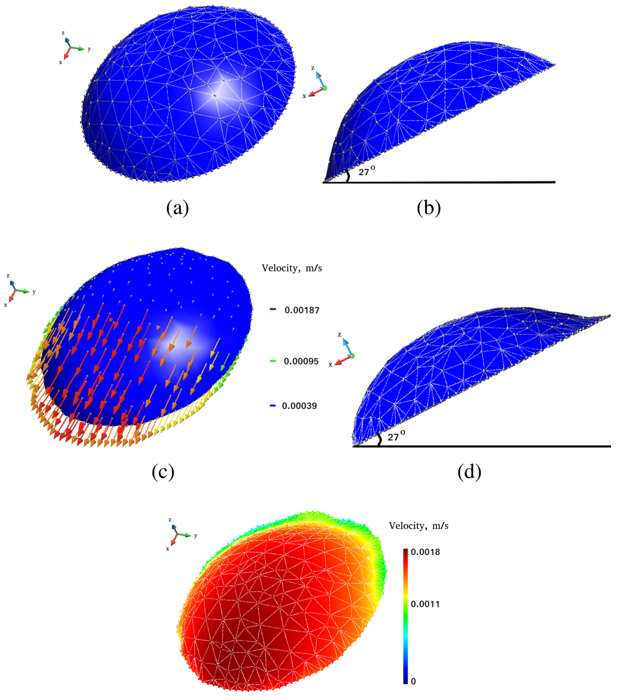

(a) (b)

(c) (d)

(e)

FIG. 12. Case #3: sliding profiles for viscous Newtonian fluid on an omniphilic smooth glass: (a) initial configuration, (b) initial configuration, side view, (c) steady-state configuration, (d) steady-state configuration, side view, and (e) steady-state velocity profile.

found to be in very good agreement with the experiment (Table VII). In 3D, compared to 2D, the accuracy of steady-state sliding velocity increased for the case of viscous Newtonian fluid. The 3D model demonstrates its ability to replicate the full geometry of a sliding liquid drop and to account for the out-of-plane forces.

IV. CONCLUSION

This article presents a new three-dimensional model for liquid drop spreading and sliding. The model is an extension of two previously presented models for two-dimensional analysis to account for the out-of-plane forces and replicate the full shape of a moving droplet. The extension to three dimensions required an algorithm to detect the contact line, to perform accurate numerical evolution of the contact angle, and to allow mesh enhancements at liquid-solid interface, including the contact line. The model is based on the PFEM and includes a Navier-slip boundary condition applied at the liquid-solid interface, a dissipative force at the contact line as a function of capillary effects and the stresses acting on the contact line, as well as a retention force dependent on the contact line deformation, surface tension force, and contact angle hysteresis.

The numerical implementation of the model is first tested on droplets of arbitrary initial shape, deposited on two different substrates. The final configuration proved to be independent of the initial configuration, whereby the contact line singularity was successfully regularized and the deformed boundaries were accurately tracked. To test the validity of the model for drop spreading, several simulations were performed for a variety of liquids on hydrophobic and hydrophilic substrates. The results of the center of mass displacements, δ, of spreading viscous liquid drops are compared with experimental data available in the literature. The simulations in 2D exhibit a discrepancy of 40% relative to the experimental data, while the three-dimensional model yields errors below 22%. Thus, the out-of-plane forces cannot be neglected in drop spreading simulations. Numerical results of the spreading rate of drops are also in good agreement with the available experimental data.

The sliding model is validated for three different experimental conditions that are found in the literature, encompassing a variety of viscous fluids and substrates, both hydrophilic and hydrophobic. During the numerical simulations, the computational mesh is adapted in the vicinity of the contact line, where large deformations occur. Nodes are added/deleted at each time step to avoid mesh deterioration. The steady-state sliding velocity of the droplets obtained numerically is compared with the available experimental data. Overall, the numerical results show good agreement with the experimental data, with relative errors for the predicted velocities between 4 and 12%. The same simulations repeated in 2D lead to a 20% increase in the errors in the simulated steady-state velocity. This proves again that the out-of-plane forces play an important role in drop sliding simulations and three-dimensional simulations are required.

Our PFEM-based model for droplet spreading and sliding in three dimensions is successfully validated. The model is capable of capturing the spatio-temporal evolution of the contact line for droplets with gravity as the driving force. However, the model is limited to a single phase and the possible effects of the surrounding gas phase are not taken into account. The model is limited to the study of droplets on smooth surfaces. Future work will include two-phase flow and rolling motion. Further validation of the numerical framework could include 2D and 3D capillary rise studies, as well as spreading on rough substrates such as pillar-arrayed surfaces[90,91].

DATA AVAILABILITY STATEMENTS

The data that support the findings of this study can be provided upon request.

Compliance with ethical standards

Acknowledgment EM acknowledges the financial support by the educational sector of the Royal Commission for Jubail and Yanbu of Saudi Arabia. MS and AJ acknowledge financial support from the Natural Science and Engineering Research Council of Canada (NSERC) Collaborative Research and Development grant: NSERC CRDPJ 445887-12 and NSERC Discovery grant.

Conflict of interest The authors declare that they have no conflict of interest.

Appendix A: Elemental contribution to matrix entries of the 3D Lagrangian model

Eqs. (27), (28), (19), and (9) are assembled using the local matrices and vectors, with components defined as:

$$M^{ab} = \rho \int_{\Omega_X} N^a N^b \, \mathrm{d}\Omega_{\boldsymbol{X}} = \rho \int_{\Omega} N^a N^b J(\boldsymbol{X}) \, \mathrm{d}\Omega \tag{A1}$$

$$L^{ab} = \int_{\Omega_X} \frac{\partial N^a}{\partial X_i} \frac{\partial N^b}{\partial X_i} \Omega_{\boldsymbol{X}} = \int_{\Omega} \frac{\partial N^a}{\partial x_i} \frac{\partial N^b}{\partial x_i} J(\boldsymbol{X}) \, \mathrm{d}\Omega \tag{A2}$$

$$G_i^{ab} = -\int_{\Omega_X} \frac{\partial N^a}{\partial X_i} N^b d\Omega_{\boldsymbol{X}} = -\int_{\Omega} \frac{\partial N^a}{\partial x_i} N^b J(\boldsymbol{X}) \, \mathrm{d}\Omega \tag{A3}$$

$$f_i^a = \rho \int_{\Omega_X} N^a g_i d\Omega_{\boldsymbol{X}} = \rho \int_{\Omega} N^a g_i J(\boldsymbol{X}) \, \mathrm{d}\Omega \tag{A4}$$

$$D_i^{ab} = \int_{\Omega_X} N^a \frac{\partial N^b}{\partial X_i} d\Omega_{\boldsymbol{X}} = \int_{\Omega} N^a \frac{\partial N^b}{\partial x_i} J(\boldsymbol{X}) \, \mathrm{d}\Omega \tag{A5}$$

$$f_{st,i}^a = -\int_{\Gamma_{l,\mathrm{X}}} \gamma\kappa N^a n_i d\Gamma_{\boldsymbol{X}} = -\int_{\Gamma_l} \gamma\kappa N^a n_i J_\Gamma(\boldsymbol{X}) \, \mathrm{d}\Gamma \tag{A6}$$

$$f_{\partial\Gamma,i}^a = -\int_{\partial\Gamma_{\mathrm{X}}} \beta_{\partial\Gamma} \boldsymbol{v} \cdot \Big(\boldsymbol{v} \cdot (\boldsymbol{e}_x + \boldsymbol{e}_y) \Big)_i N^a d\partial\Gamma_{\boldsymbol{X}} =$$

$$-\int_{\partial\Gamma} \beta_{\partial\Gamma} \Big(\boldsymbol{v} \cdot (\boldsymbol{e}_x + \boldsymbol{e}_y) \Big)_i N^a J_\Gamma(\boldsymbol{X}) \, \mathrm{d}\partial\Gamma \tag{A7}$$

$$f_{\Gamma_S,i}^a = -\int_{\Gamma_{S,\mathrm{X}}} \beta_{\Gamma_s} \Big(\boldsymbol{v} \cdot (\boldsymbol{e}_x + \boldsymbol{e}_y) \Big)_i N^a d\Gamma_{\boldsymbol{X}} =$$

$$-\int_{\Gamma_S} \beta_{\Gamma_s} \Big(\boldsymbol{v} \cdot (\boldsymbol{e}_x + \boldsymbol{e}_y) \Big)_i N^a J_\Gamma(\boldsymbol{X}) \, \mathrm{d}\Gamma \tag{A8}$$

where N^a represents the standard finite element shape function at node a, and the index i is used for the spatial components. The present model is based on the updated Lagrangian formulation (ULF), and therefore the integration domains in eqs. (A1)-(A5), $\Omega_{\boldsymbol{X}}$, correspond to the updated configuration. The transformation between the reference configuration, Ω, and the updated one is performed using the Jacobians $J(\boldsymbol{X})$ and $J_\Gamma(\boldsymbol{X})$. Details on the determination of the mean curvature in three dimensions (κ in Eq. (A6)) can be found in reference[2].

Appendix B: Solution algorithm of the 3D Lagrangian model

Given a known configuration $\boldsymbol{X}_n$, velocity $\bar{\boldsymbol{v}}_n$, and pressure $\bar{p}_n$, at time t_n, the procedure for obtaining the values of these variables at the next time step t_{n+1} is summarized in Algorithm 1.

Algorithm 1. Simulation algorithm of the liquid phase problem using a PFEM formulation.

```
for $t = t_{n+1}$ do
    Current configuration is the known configuration, such that: $\boldsymbol{X}_{n+1}^{k} = \boldsymbol{X}_n$
    for nonlinear iteration $k$ do
        Obtain curvature at $\boldsymbol{X}_{n+1}^{k}$;
        Update discrete operators;
        Compute $f_{st,i}^{a}$, $f_{\partial\Gamma,i}^{a}$, and $f_{\Gamma_S,i}^{a}$;
        Solve system of equations for liquid phase, eq. (29);
        Update both velocity and pressure, such that: $\bar{\boldsymbol{v}}_{n+1}^{k+1} = \bar{\boldsymbol{v}}_{n+1}^{k} + \delta\bar{\boldsymbol{v}}$ and $\bar{p}_{n+1}^{k+1} = \bar{p}_{n+1}^{k} + \delta\bar{p}$, respectively
        Update configuration, such that: $\boldsymbol{X}_{n+1}^{k+1} = \boldsymbol{X}_{n+1}^{k} + \Delta t \cdot \delta\bar{\boldsymbol{v}}$
        Remesh;
    end for
    $\boldsymbol{X}_{n+1} = \boldsymbol{X}_n + \Delta t \cdot \bar{\boldsymbol{v}}_{n+1}$
end for
```

Appendix C: Geometry of spherical drops

The equations which relate the volume and contact angle to the geometrical parameters of a drop in contact with an omniphilic or an omniphobic surface are presented here (see references[62,92] for more details). The initial shape of the drop is considered as i) a spherical cap on an omniphilic substrate or ii) a spherical drop on an omniphobic substrate, as shown in Fig.13(a) and 13(b), respectively. This assumption might produce up to 15% error when the gravitational force is considered for a drop size of the order of 10 μL[60].

i) Starting with a known liquid drop volume and equilibrium contact angle condition of a spherical cap, the drop height (H), drop radius (R), and wetting radius (a) are obtained using the following equations:

$$R = \left(\frac{V}{\frac{\pi}{3}(2 - 3\cos\theta + \cos^3\theta)} \right)^{\frac{1}{3}} \tag{C1}$$

$$a = R\sin\theta \tag{C2}$$

$$H = R(1 - \cos\theta) \tag{C3}$$

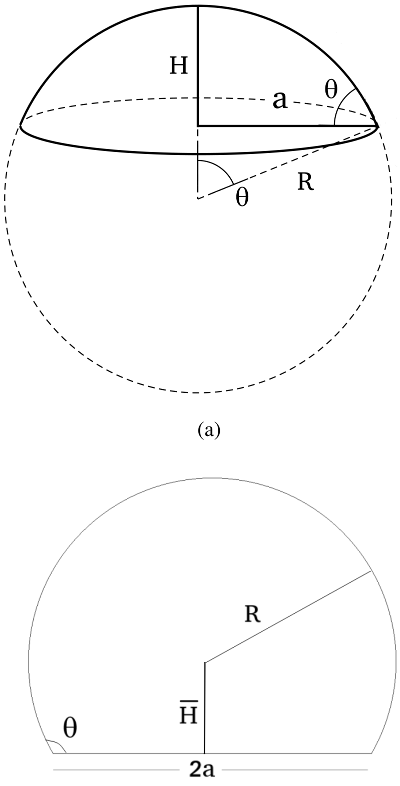

(a)

(b)

FIG. 13. Geometrical parameters of a drop (a) on an omniphilic substrate and (b) on an omniphobic substrate.

ii) Starting with a known liquid drop volume and equilibrium contact angle condition, the geometrical parameters of a spherical drop are obtained as follows:

$$R = \left(\frac{V}{\frac{4\pi}{3} - \frac{\pi}{3}(1 + \cos\theta)^2(2 - \cos\theta)} \right)^{\frac{1}{3}} \tag{C4}$$

$$\bar{H} = -R\cos\theta \tag{C5}$$

REFERENCES

[1] T. Hattori, M. Sakai, S. Akaike, S. Koshizuka, Numerical simulation of droplet sliding on an inclined surface using moving particle semi-implicit method, Computational Particle Mechanics 5 (4) (2018) 477–491.

[2] A. Jarauta, P. Ryzhakov, J. Pons-Prats, M. Secanell, An implicit surface tension model for the analysis of droplet dynamics, Journal of Computational Physics 374 (2018) 1196–1218.

[3] M. Kostoglou, T. D. Karapantsios, An analytical two-dimensional linearized droplet shape model for combined tangential and normal body forces, Colloids and Interfaces 4 (3) (2020) 35.

[4] K. Yong, P. B. Ganesan, M. S. N. Kazi, S. Ramesh, I. A. Badruddin, N. M. Mubarak, Sliding behavior of droplet on a hydrophobic surface with hydrophilic cavities: A simulation study, Physics of Fluids 30 (12) (2018) 122006.

[5] M. Liu, X.-P. Chen, Numerical study on the stick-slip motion of contact line moving on heterogeneous surfaces, Physics of Fluids 29 (8) (2017) 082102.

Accepted Manuscript
Version of record at: https://doi.org/10.1063/5.0091699

[6] Y. Tian, Y. Tian, G. Shi, B. Zhou, C. Zhang, L. He, Experimental study on oil droplet breakup under the action of turbulent field in modified concentric cylinder rotating device, Physics of Fluids 32 (8) (2020) 087105.

[7] S. Bhardwaj, A. Dalal, G. Biswas, P. P. Mukherjee, Analysis of droplet dynamics in a partially obstructed confinement in a three-dimensional channel, Physics of Fluids 30 (10) (2018) 102102.

[8] M. Sabharwal, J. Gostick, M. Secanell, Virtual liquid water intrusion in fuel cell gas diffusion media, Journal of The Electrochemical Society 165 (7) (2018) F553–F563.

[9] J. Zhou, D. Stanier, A. Putz, M. Secanell, A mixed wettability pore size distribution based mathematical model for analyzing two-phase flow in porous electrodes II. Model validation and analysis of micro-structural parameters, Journal of The Electrochemical Society 164 (6) (2017) F540–F556.

[10] M. Andersson, V. Vukčević, S. Zhang, Y. Qi, H. Jasak, S. Beale, W. Lehnert, Modeling of droplet detachment using dynamic contact angles in polymer electrolyte fuel cell gas channels, International Journal of Hydrogen Energy 44 (21) (2019) 11088–11096.

[11] M. R. Hashemi, P. B. Ryzhakov, R. Rossi, Toward droplet dynamics simulation in polymer electrolyte membrane fuel cells: Three-dimensional numerical modeling of confined water droplets with dynamic contact angle and hysteresis, Physics of Fluids 33 (12) (2021) 122109.

[12] A. Jarauta, P. Ryzhakov, M. Secanell, P. Waghmare, J. Pons-Prats, Numerical study of droplet dynamics in a polymer electrolyte fuel cell gas channel using an embedded eulerian-lagrangian approach, Journal of Power Sources 323 (2016) 201–212.

[13] A. Santamaria, P. Das, J. MacDonald, A. Weber, Liquid-water interactions with gas-diffusion-layer surfaces, Journal of The Electrochemical Society 161 (12) (2014) F1184–F1193.

[14] A. Klimanek, Numerical modelling of natural draft wet-cooling towers, Archives of Computational Methods in Engineering 20 (1) (2013) 61–109.

[15] M. H. Mantelli, Development of porous media thermosyphon technology for vapor recovering in cross-current cooling towers, Applied Thermal Engineering 108 (2016) 398–413.

[16] K. Bartlet, S. Movafaghi, A. Kota, K. C. Popat, Superhemophobic titania nanotube array surfaces for blood contacting medical devices, RSC advances 7 (56) (2017) 35466–35476.

[17] A. Milionis, K. G. Krishnan, E. Loth, M. Lawrence, Dynamic wetting of human blood and plasma on various surfaces, Colloids and Surfaces B: Biointerfaces 166 (2018) 218–223.

[18] G. Hassan, B. S. Yilbas, A. Al-Sharafi, H. Al-Qahtani, Self-cleaning of a hydrophobic surface by a rolling water droplet, Scientific reports 9 (1) (2019) 1–14.

[19] D. Sun, K. F. Böhringer, An active self-cleaning surface system for photovoltaic modules using anisotropic ratchet conveyors and mechanical vibration, Microsystems & Nanoengineering 6 (1) (2020) 1–12.

[20] A. Jarauta, P. Ryzhakov, Challenges in computational modeling of two-phase transport in polymer electrolyte fuel cells flow channels: A review, Archives of Computational Methods in Engineering 25 (4) (2018) 1027–1057.

[21] M. Wörner, Numerical modeling of multiphase flows in microfluidics and micro process engineering: a review of methods and applications, Microfluidics and nanofluidics 12 (6) (2012) 841–886.

[22] A. M. Boelens, J. J. de Pablo, Generalised Navier boundary condition for a volume of fluid approach using a finite-volume method, Physics of Fluids 31 (2) (2019) 021203.

[23] J. Zhang, M. K. Borg, J. M. Reese, Multiscale simulation of dynamic wetting, International Journal of Heat and Mass Transfer 115 (2017) 886–896.

[24] S. Afkhami, S. Zaleski, M. Bussmann, A mesh-dependent model for applying dynamic contact angles to VOF simulations, Journal of computational physics 228 (15) (2009) 5370–5389.

[25] G. Buscaglia, R. Ausas, Variational formulations for surface tension, capillarity and wetting, Computer Methods in Applied Mechanics and Engineering 200 (45-46) (2011) 3011–3025.

[26] E. Mahrous, R. V. Roy, A. Jarauta, M. Secanell, A two-dimensional numerical model for the sliding motion of liquid drops by the particle finite element method, Physics of Fluids 33 (3) (2021) 032117.

[27] K. J. Vachaparambil, K. E. Einarsrud, Comparison of surface tension models for the volume of fluid method, Processes 7 (8) (2019) 542.

[28] T. Yamamoto, Y. Okano, S. Dost, Validation of the S-CLSVOF method with the density-scaled balanced continuum surface force model in multiphase systems coupled with thermocapillary flows, International Journal for Numerical Methods in Fluids 83 (3) (2017) 223–244.

[29] K. Chen, M. Hickner, D. Noble, Simplified models for predicting the onset of liquid water droplet instability at the gas diffusion layer/gas flow channel interface, International Journal of Energy Research 29 (12) (2005) 1113–1132.

[30] A. Jarauta, M. Secanell, J. Pons-Prats, P. Ryzhakov, S. Idelsohn, E. Oñate, A semi-analytical model for droplet dynamics on the GDL surface of a PEFC electrode, international journal of hydrogen energy 40 (15) (2015) 5375–5383.

[31] E. Kumbur, K. Sharp, M. Mench, Liquid droplet behavior and instability in a polymer electrolyte fuel cell flow channel, Journal of Power Sources 161 (1) (2006) 333–345. `doi:https://doi.org/10.1016/j.jpowsour.2006.04.093`.
URL `https://www.sciencedirect.com/science/article/pii/S037877530600663X`

[32] C. M. Oishi, F. P. Martins, R. L. Thompson, Gravitational effects in the collision of elasto-viscoplastic drops on a vertical plane, Fluids 5 (2) (2020) 61.

[33] A. F. Stalder, T. Melchior, M. Müller, D. Sage, T. Blu, M. Unser, Low-bond axisymmetric drop shape analysis for surface tension and contact angle measurements of sessile drops, Colloids and Surfaces A: Physicochemical and Engineering Aspects 364 (1-3) (2010) 72–81.

[34] M. Eres, L. Schwartz, R. Roy, Fingering phenomena for driven coating films, Physics of Fluids 12 (6) (2000) 1278–1295.

[35] S. C. Cho, Y. Wang, K. Chen, Droplet dynamics in a polymer electrolyte fuel cell gas flow channel: Forces, deformation and detachment. II: Comparisons of analytical solution with numerical and experimental results, Journal of Power Sources 210 (2012) 191–197.

[36] A. Theodorakakos, T. Ous, M. Gavaises, J. Nouri, N. Nikolopoulos, H. Yanagihara, Dynamics of water droplets detached from porous surfaces of relevance to PEM fuel cells, Journal of Colloid and Interface Science 300 (2006) 673–687.

[37] X. Zhu, Q. Liao, P. Sui, N. Djilali, Numerical investigation of water droplet dynamics in a low-temperature fuel cell microchannel: Effect of channel geometry, Journal of Power Sources 195 (2010) 801–812.

[38] P. Spelt, A level-set approach for simulations of flows with multiple moving contact lines with hysteresis, Journal of Computational Physics 207 (2) (2005) 389–404.

[39] S. Manservisi, R. Scardovelli, A variational approach to the contact angle dynamics of spreading droplets, Computers & Fluids 38 (2) (2009) 406–424.

[40] W. Ren, W. E, Boundary conditions for the moving contact line problem, Physics of fluids 19 (2) (2007) 022101.

[41] E. Mahrous, A. Jarauta, T. Chan, P. Ryzhakov, A. Z. Weber, R. V. Roy, M. Secanell, A particle finite element-based model for droplet spreading analysis, Physics of Fluids 32 (4) (2020) 042106.

[42] M. Hashemi, P. Ryzhakov, R. Rossi, Three dimensional modeling of liquid droplet spreading on solid surface: An enriched finite element/level-set approach, Journal of Computational Physics 442 (2021) 110480.

[43] S. Afkhami, Challenges of numerical simulation of dynamic wetting phenomena: a review, Current Opinion in Colloid & Interface Science 57 (2022) 101523.

[44] A. ElSherbini, A. Jacobi, Retention forces and contact angles for critical liquid drops on non-horizontal surfaces, Journal of colloid and interface science 299 (2) (2006) 841–849.

[45] J. Xie, J. Xu, W. Shang, K. Zhang, Mode selection between sliding and rolling for droplet on inclined surface: Effect of surface wettability, International Journal of Heat and Mass Transfer 122 (2018) 45–58.

[46] S. R. Annapragada, J. Y. Murthy, S. V. Garimella, Prediction of droplet dynamics on an incline, International Journal of Heat and Mass Transfer 55 (5-6) (2012) 1466–1474.

[47] S. P. Thampi, R. Adhikari, R. Govindarajan, Do liquid drops roll or slide on inclined surfaces?, Langmuir 29 (10) (2013) 3339–3346.

[48] B. S. Yilbas, A. Al-Sharafi, H. Ali, N. Al-Aqeeli, Dynamics of a water droplet on a hydrophobic inclined surface: influence of droplet size and surface inclination angle on droplet rolling, Rsc Advances 7 (77) (2017) 48806–48818.

[49] P. Ryzhakov, R. Rossi, S. Idelsohn, E. Oñate, A monolithic Lagrangian approach for fluid–structure interaction problems, Computational mechanics 46 (6) (2010) 883–899.

[50] P. Ryzhakov, A. Jarauta, An embedded approach for immiscible multi-fluid problems, International Journal for Numerical Methods in Fluids 81 (6)

Accepted Manuscript
Version of record at: https://doi.org/10.1063/5.0091699

(2016) 357–376.

[51] P. Ryzhakov, A. Jarauta, M. Secanell, J. Pons-Prats, On the application of the pfem to droplet dynamics modeling in fuel cells, Computational Particle Mechanics 4 (3) (2017) 285–295.

[52] J. Venkatesan, S. Ganesan, On the navier-slip boundary condition for computations of impinging droplets, in: 2015 IEEE 22nd International Conference on High Performance Computing Workshops, IEEE, 2015, pp. 2–11.

[53] J. Venkatesan, S. Ganesan, Computational modeling of impinging viscoelastic droplets, Journal of Non-Newtonian Fluid Mechanics 263 (2019) 42–60.

[54] I. S. Bayer, C. M. Megaridis, Contact angle dynamics in droplets impacting on flat surfaces with different wetting characteristics, Journal of Fluid Mechanics 558 (2006) 415–449.

[55] D. Bonn, J. Eggers, J. Indekeu, J. Meunier, E. Rolley, Wetting and spreading, Reviews of modern physics 81 (2) (2009) 739.

[56] Y. Yoon, D. Kim, J.-B. Lee, Hierarchical micro/nano structures for superhydrophobic surfaces and super-lyophobic surface against liquid metal, Micro and Nano Systems Letters 2 (1) (2014) 3.

[57] T.-S. Jiang, O. Soo-Gun, J. C. Slattery, Correlation for dynamic contact angle, Journal of Colloid and Interface Science 69 (1) (1979) 74–77.

[58] R. Brown, F. Orr Jr, L. Scriven, Static drop on an inclined plate: analysis by the finite element method, Journal of Colloid and Interface Science 73 (1) (1980) 76–87.

[59] C. W. Extrand, Y. Kumagai, Liquid drops on an inclined plane: the relation between contact angles, drop shape, and retentive force, Journal of colloid and interface science 170 (2) (1995) 515–521.

[60] H.-Y. Kim, H. J. Lee, B. H. Kang, Sliding of liquid drops down an inclined solid surface, Journal of Colloid and Interface Science 247 (2) (2002) 372–380.

[61] C.-W. Yao, S. Tang, D. Sebastian, R. Tadmor, Sliding of water droplets on micropillar-structured superhydrophobic surfaces, Applied Surface Science 504 (2020) 144493.

[62] A. Jarauta, Modeling of droplet dynamics in a proton exchange fuel cell electrode channel, Ph.D. thesis, Universitat Politècnica de Catalunya (2016).

[63] L. Chen, G. K. Auernhammer, E. Bonaccurso, Short time wetting dynamics on soft surfaces, Soft Matter 7 (19) (2011) 9084–9089.

[64] J. B. Keller, P. A. Milewski, J.-M. Vanden-Broeck, Merging and wetting driven by surface tension, European Journal of Mechanics-B/Fluids 19 (4) (2000) 491–502.

[65] Y. Renardy, S. Popinet, L. Duchemin, M. Renardy, S. Zaleski, C. Josserand, M. Drumright-Clarke, D. Richard, C. Clanet, D. Quéré, Pyramidal and toroidal water drops after impact on a solid surface, Journal of Fluid Mechanics 484 (2003) 69–83.

[66] M. Sussman, M. Ohta, A stable and efficient method for treating surface tension in incompressible two-phase flow, SIAM Journal on Scientific Computing 31 (4) (2009) 2447–2471.

[67] S. Idelsohn, J. Marti, A. Souto-Iglesias, E. Oñate, Interaction between an elastic structure and free-surface flows: experimental versus numerical comparisons using the PFEM, Computational Mechanics 43 (1) (2008) 125–132.

[68] J. Marti, P. Ryzhakov, An explicit–implicit finite element model for the numerical solution of incompressible navier–stokes equations on moving grids, Computer Methods in Applied Mechanics and Engineering 350 (2019) 750–765.

[69] J. Marti, P. Ryzhakov, An explicit/implicit Runge–Kutta-based PFEM model for the simulation of thermally coupled incompressible flows, Computational Particle Mechanics 7 (1) (2020) 57–69.

[70] E. Oñate, S. R. Idelsohn, F. Del Pin, R. Aubry, The particle finite element method—an overview, International Journal of Computational Methods 1 (02) (2004) 267–307.

[71] E. Oñate, S. R. Idelsohn, M. A. Celigueta, R. Rossi, J. Marti, J. M. Carbonell, P. Ryzhakov, B. Suárez, Advances in the particle finite element method (PFEM) for solving coupled problems in engineering, in: Particle-Based Methods, Springer, 2011, pp. 1–49.

[72] J. Guermond, P. Minev, J. Shen, An overview of projection methods for incompressible flows, Computer methods in applied mechanics and engineering 195 (44-47) (2006) 6011–6045.

[73] J. Donea, A. Huerta, Finite element methods for flow problems, John Wiley & Sons, 2003.

[74] M. Chowdhury, B. R. Kumar, On subgrid multiscale stabilized finite element method for advection-diffusion-reaction equation with variable coefficients, Applied Numerical Mathematics 150 (2020) 576–586.

[75] R. Codina, A stabilized finite element method for generalized stationary incompressible flows, Computer Methods in Applied Mechanics and Engineering 190 (20-21) (2001) 2681–2706.

[76] E. Moreno, A. Larese, M. Cervera, Modelling of Bingham and Herschel–Bulkley flows with mixed P1/P1 finite elements stabilized with orthogonal subgrid scale, Journal of Non-Newtonian Fluid Mechanics 228 (2016) 1–16.

[77] M. Cremonesi, A. Franci, S. Idelsohn, E. Oñate, A state of the art review of the particle finite element method (pfem), Archives of Computational Methods in Engineering 27 (5) (2020) 1709–1735.

[78] P. Ryzhakov, R. Rossi, S. R. Idelsohn Barg, Lagrangian FE methods for coupled problems in fluid mechanics, International Centre for Numerical Methods in Engineering (CIMNE), 2010.

[79] N. Akkiraju, H. Edelsbrunner, M. Facello, P. Fu, E. Mucke, C. Varela, Alpha shapes: definition and software, in: Proceedings of the 1st international computational geometry software workshop, Vol. 63, 1995.

[80] P. Dadvand, R. Rossi, E. Oñate, An object-oriented environment for developing finite element codes for multi-disciplinary applications, Archieves of Computational Methods in Engineering 17/3 (2010) 253–297.

[81] C. T. Kelley, Iterative methods for linear and nonlinear equations, SIAM, 1995.

[82] F. D. Egitto, L. J. Matienzo, Plasma modification of polymer surfaces for adhesion improvement, IBM Journal of Research and Development 38 (4) (1994) 423–439.

[83] D. K. Owens, R. Wendt, Estimation of the surface free energy of polymers, Journal of applied polymer science 13 (8) (1969) 1741–1747.

[84] M. Abolghasemibizaki, C. J. Robertson, C. P. Fergusson, R. L. McMasters, R. Mohammadi, Rolling viscous drops on a non-wettable surface containing both micro-and macro-scale roughness, Physics of Fluids 30 (2) (2018) 023105.

[85] J. C. Bird, S. Mandre, H. A. Stone, Short-time dynamics of partial wetting, Physical review letters 100 (23) (2008) 234501.

[86] L. Chen, E. Bonaccurso, M. E. Shanahan, Inertial to viscoelastic transition in early drop spreading on soft surfaces, Langmuir 29 (6) (2013) 1893–1898.

[87] A.-L. Biance, C. Clanet, D. Quéré, First steps in the spreading of a liquid droplet, Physical Review E 69 (1) (2004) 016301.

[88] L. Courbin, J. C. Bird, M. Reyssat, H. A. Stone, Dynamics of wetting: from inertial spreading to viscous imbibition, Journal of Physics: Condensed Matter 21 (46) (2009) 464127.

[89] H. Xu, A. Clarke, J. Rothstein, R. Poole, Viscoelastic drops moving on hydrophilic and superhydrophobic surfaces, Journal of colloid and interface science 513 (2018) 53–61.

[90] Q. Yuan, Y.-P. Zhao, Multiscale dynamic wetting of a droplet on a lyophilic pillar-arrayed surface, Journal of Fluid Mechanics 716 (2013) 171–188.

[91] Q. Yuan, X. Huang, Y.-P. Zhao, Dynamic spreading on pillar-arrayed surfaces: Viscous resistance versus molecular friction, Physics of Fluids 26 (9) (2014) 092104.

[92] A. Esposito, P. Polverino, C. Pianese, Y. G. Guezennec, A lumped model of single droplet deformation, oscillation and detachment on the gdl surface of a PEM fuel cell, in: International Conference on Fuel Cell Science, Engineering and Technology, Vol. 44045, 2010, pp. 581–592.

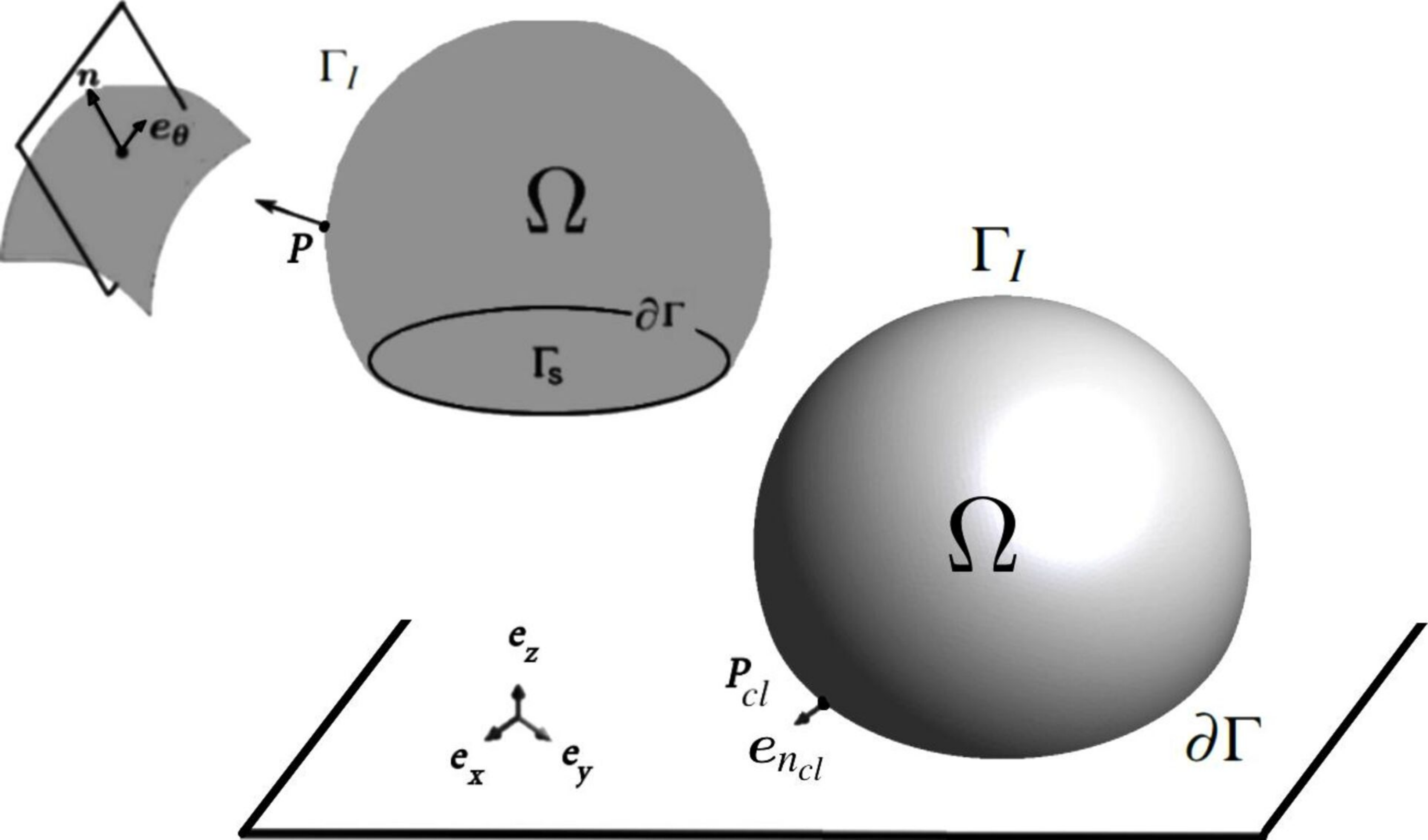
n
e_θ
Γ_l
Ω
P
$\partial\Gamma$
Γ_s
Γ_l
Ω
e_z
P_{cl}
e_x
e_y
$e_{n_{cl}}$
$\partial\Gamma$

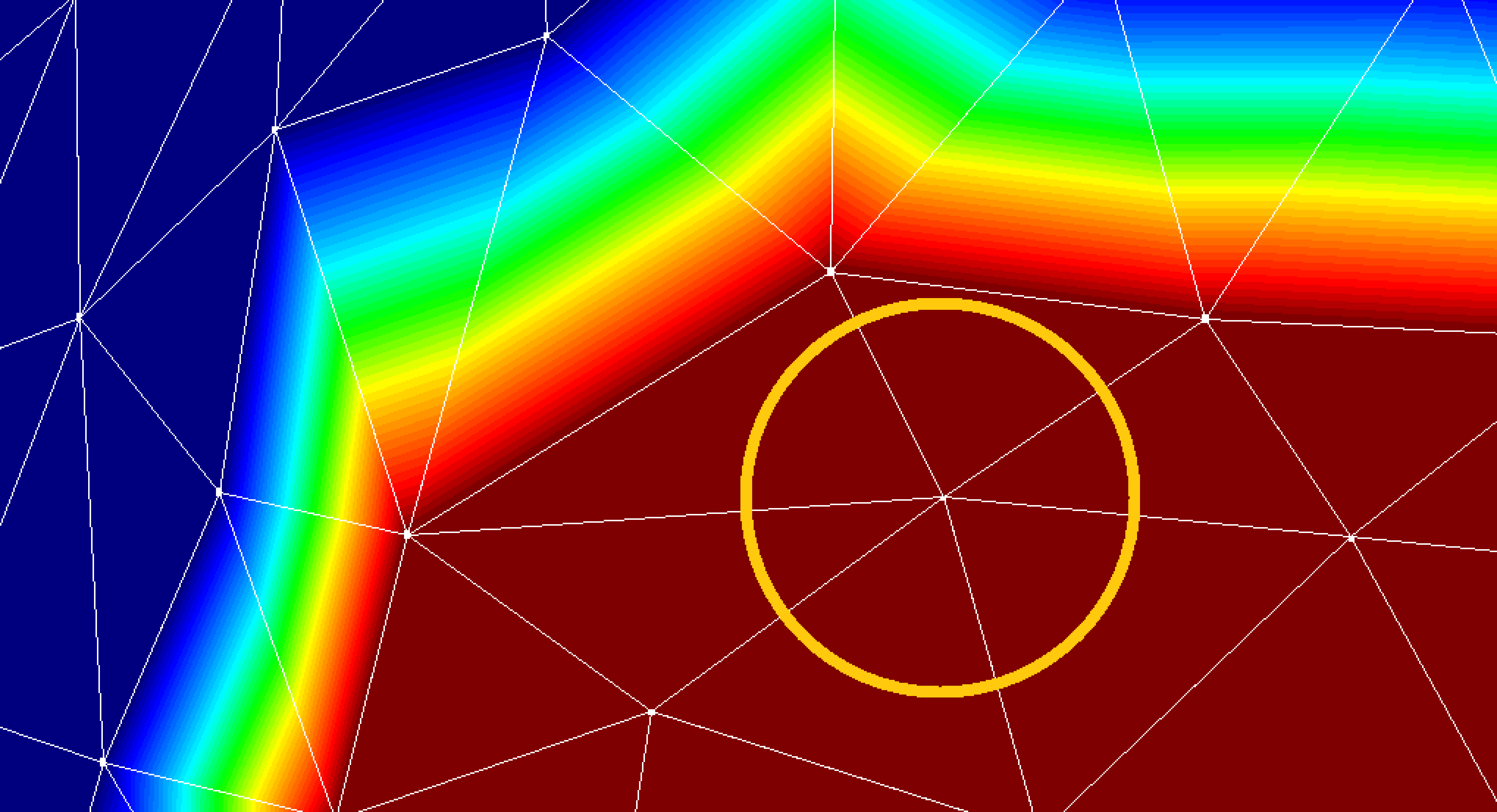

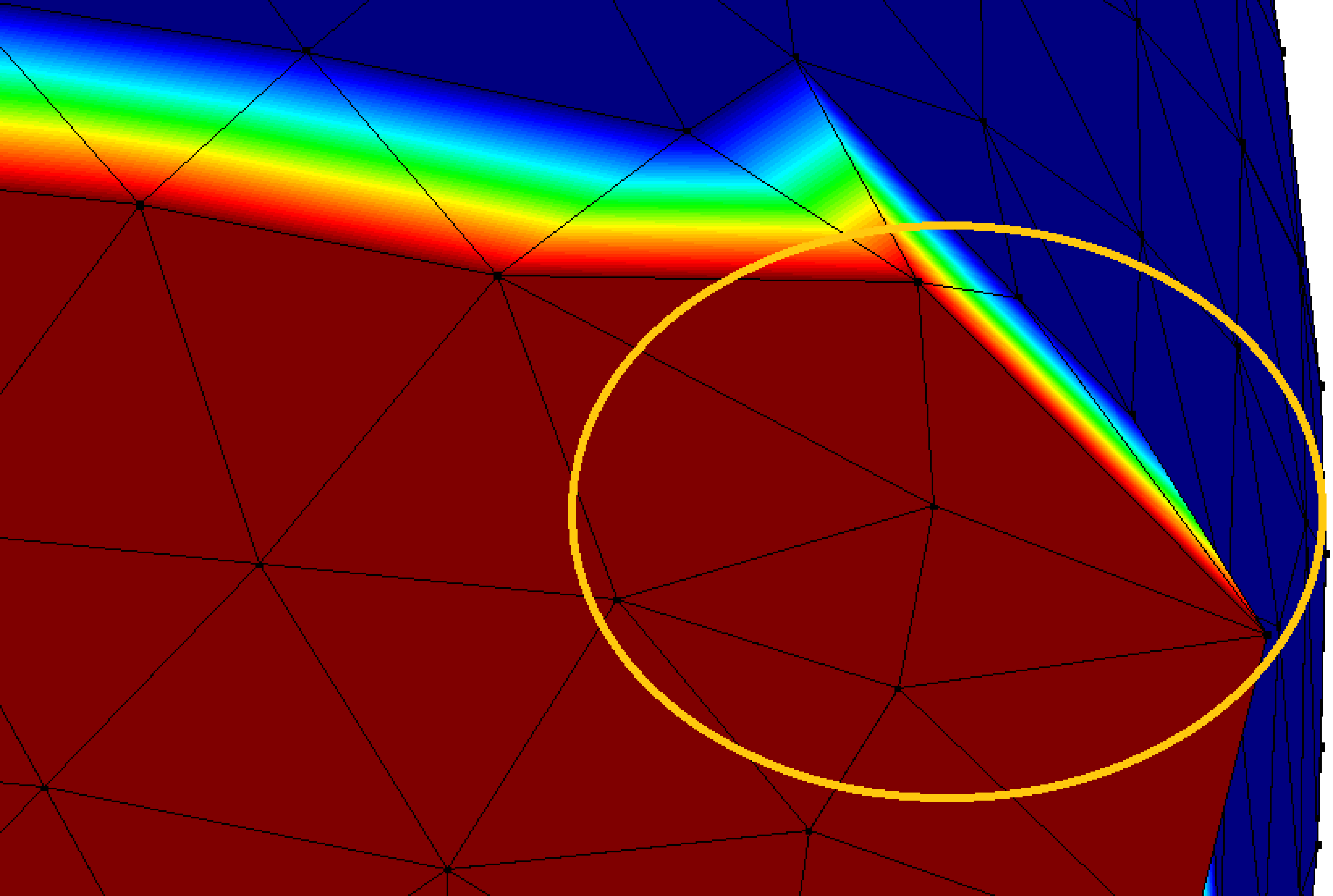

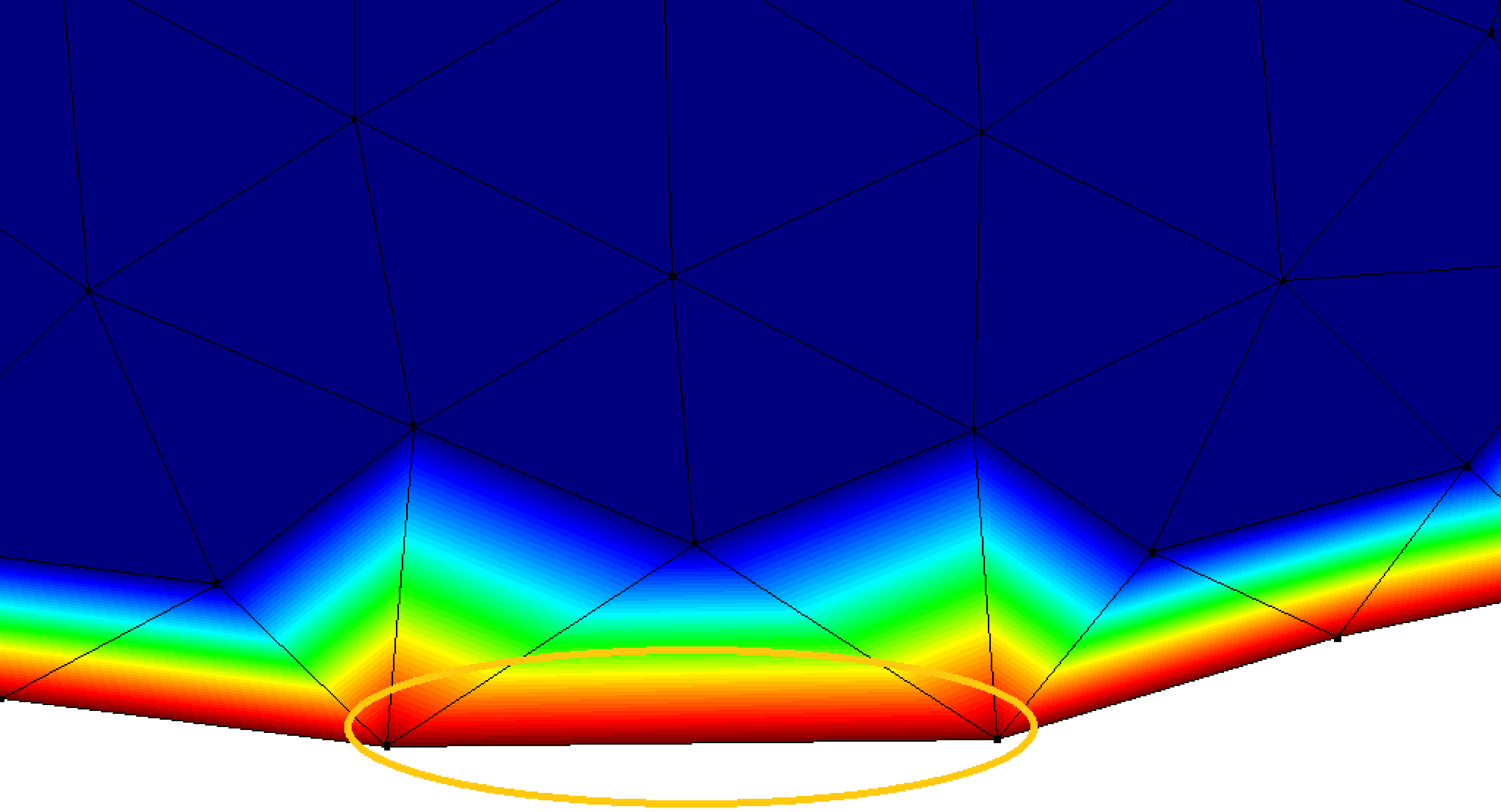

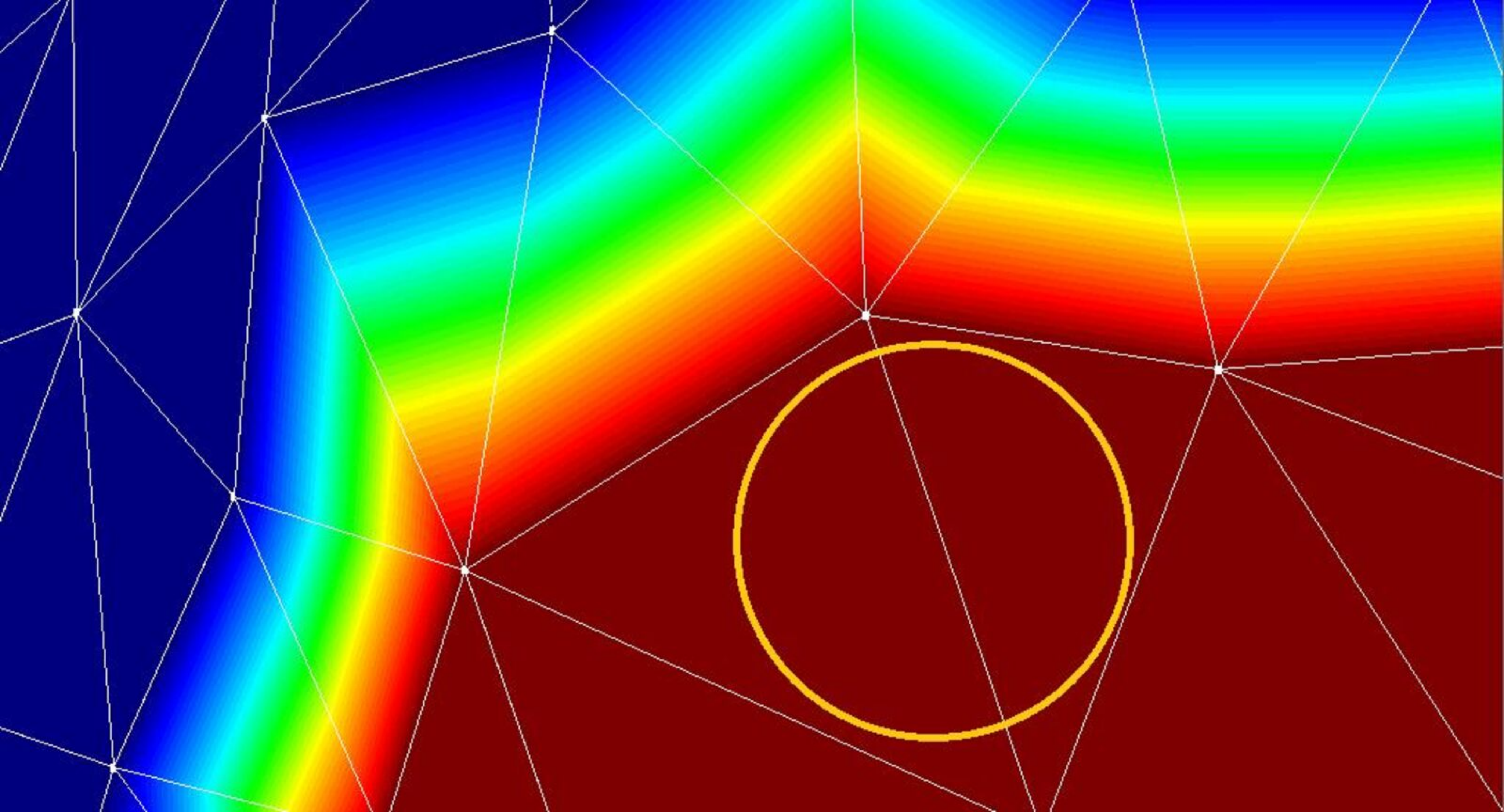

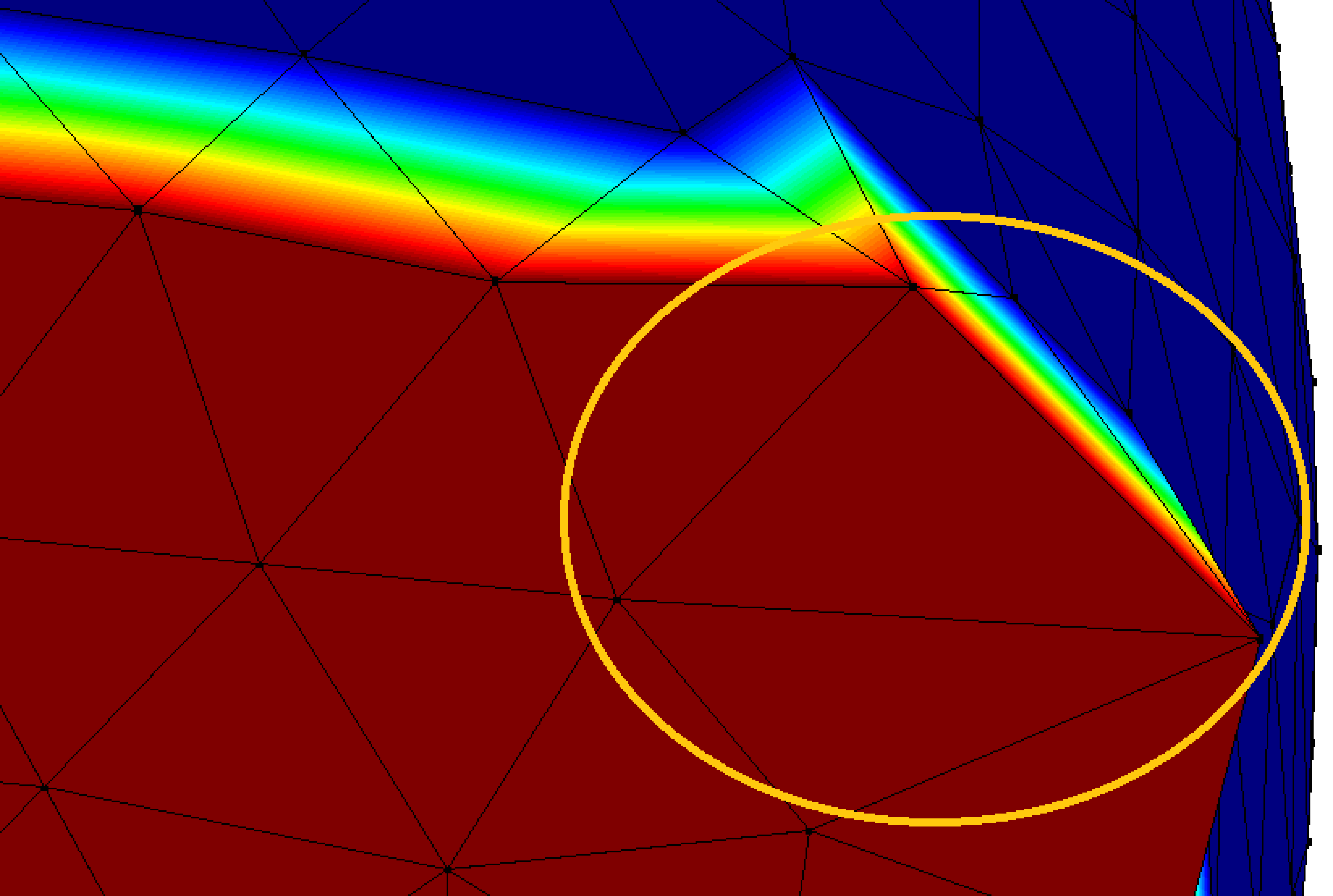

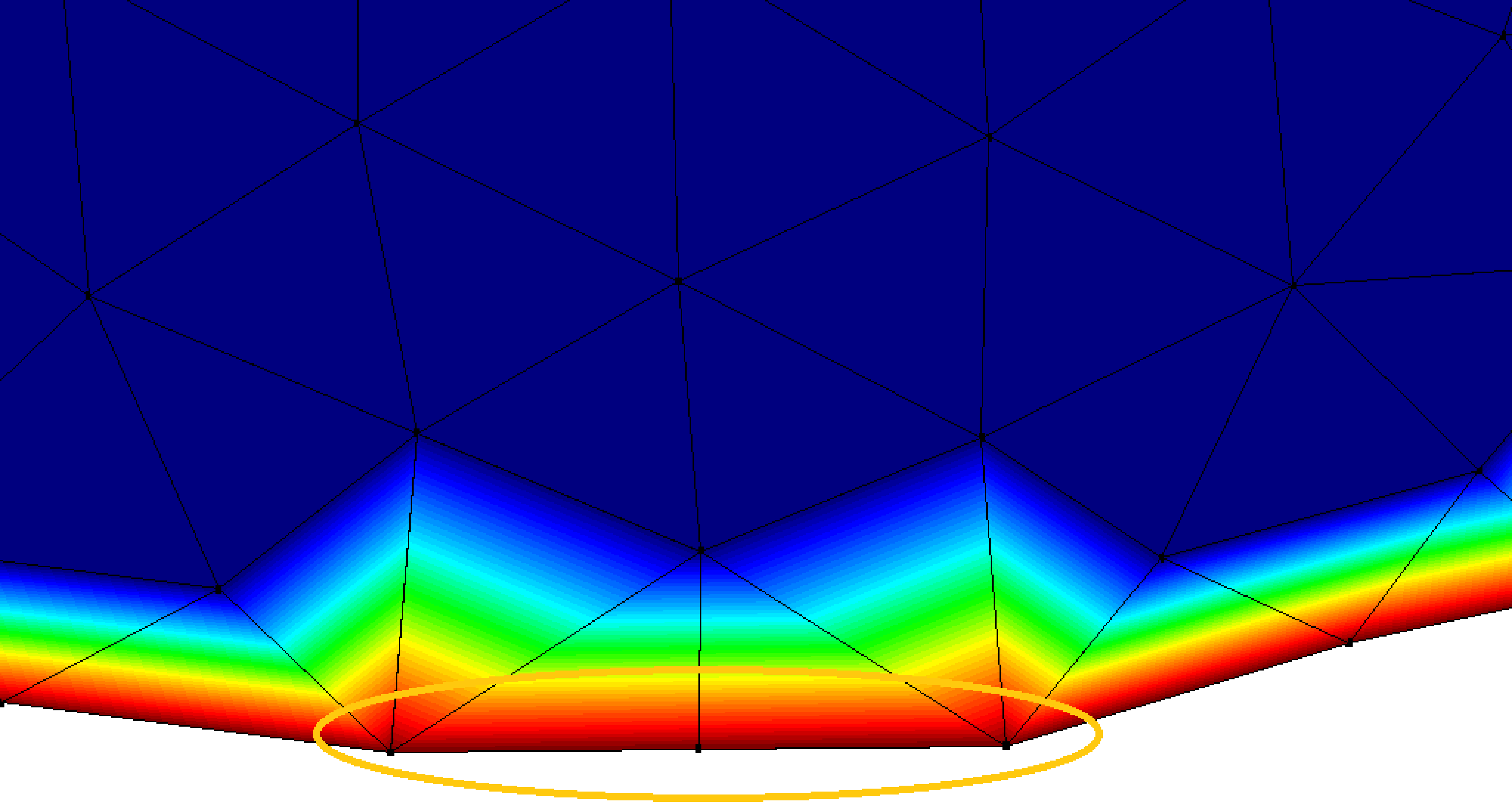

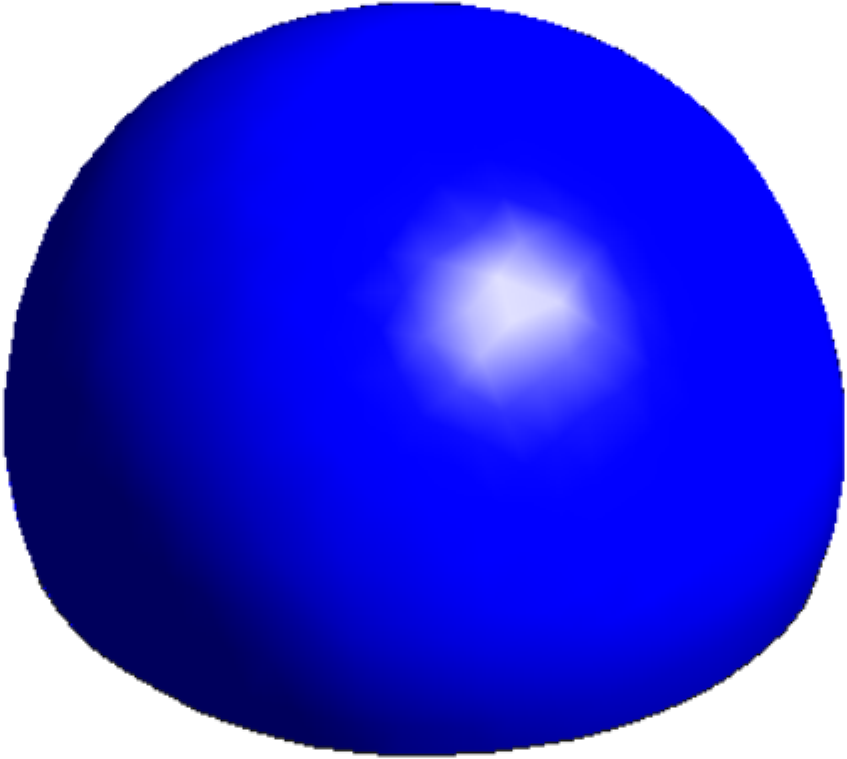

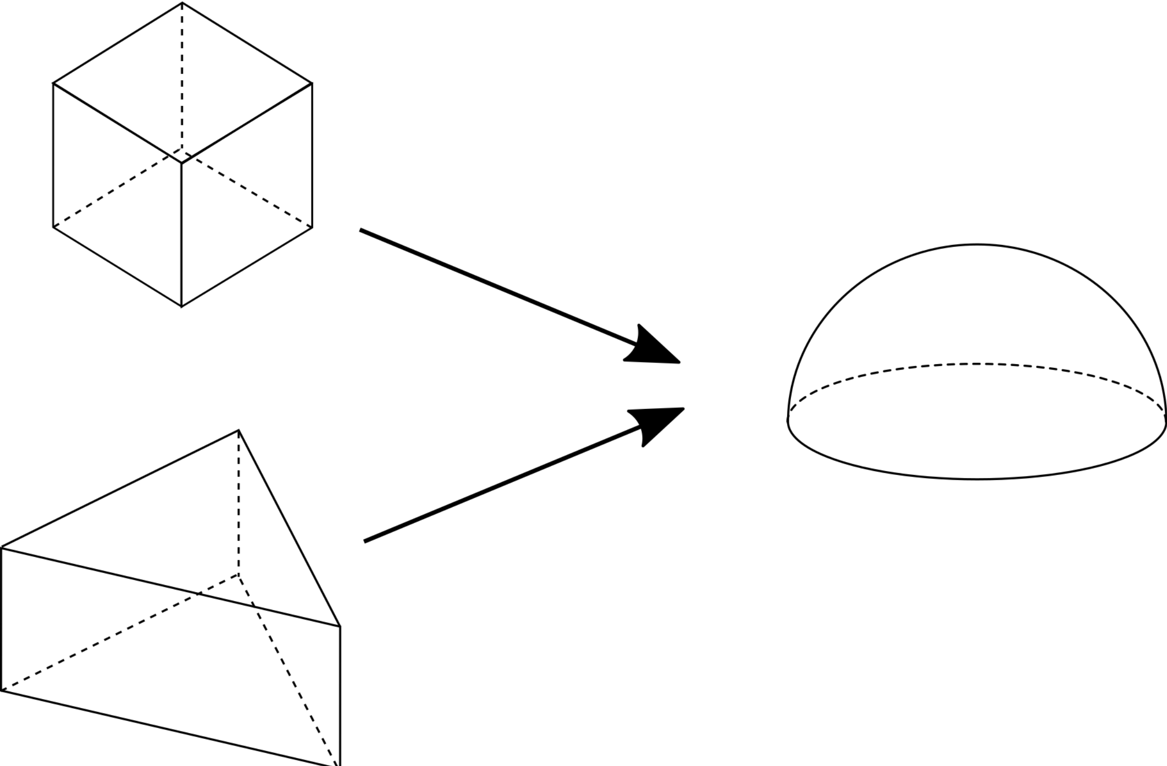

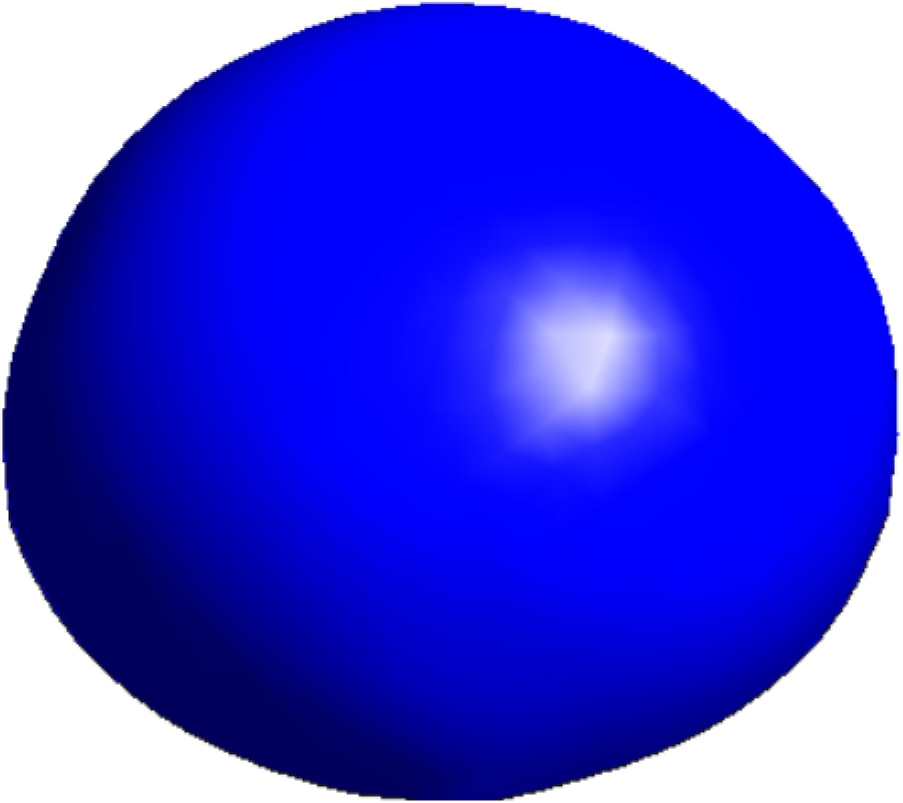

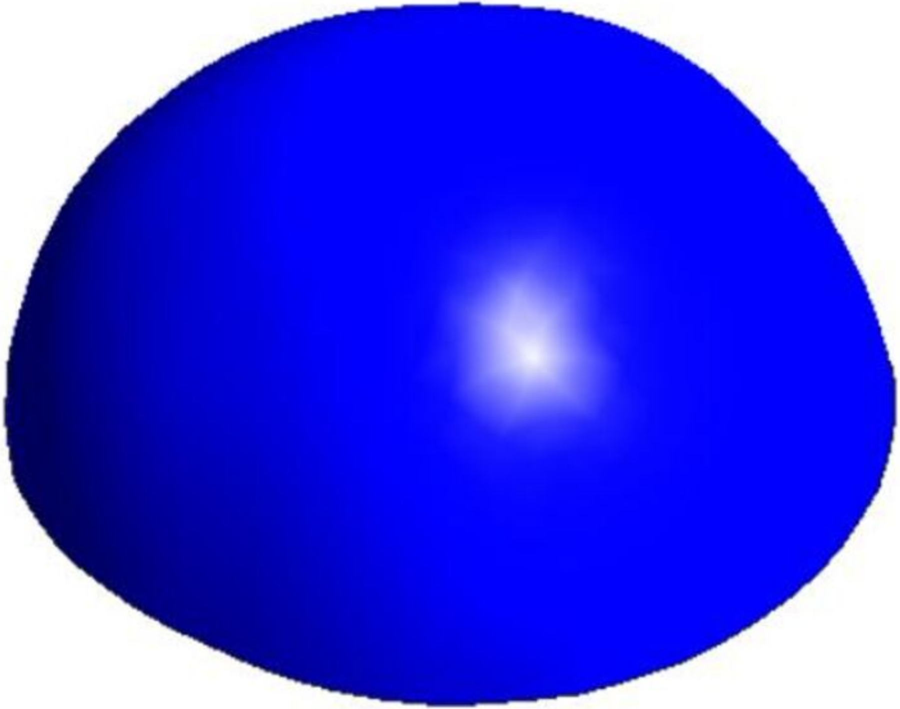

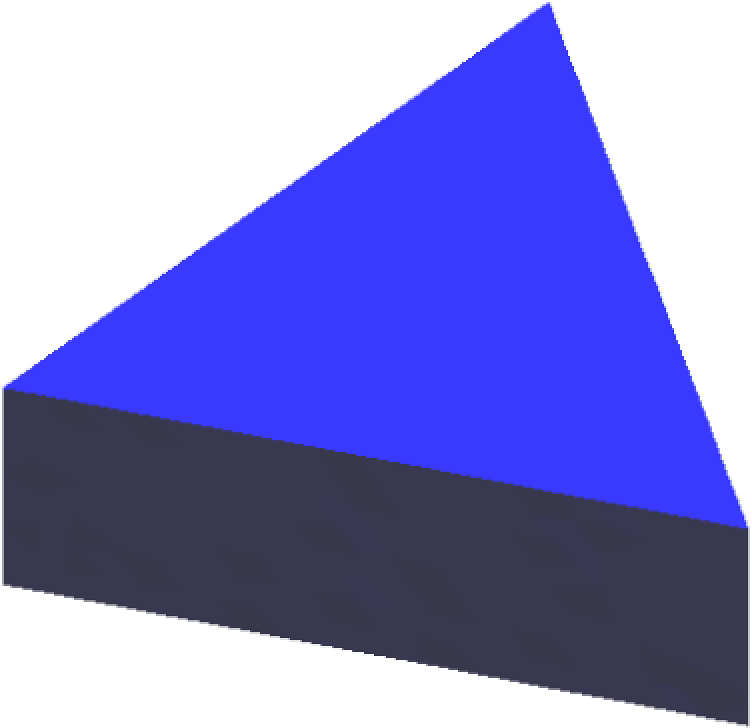

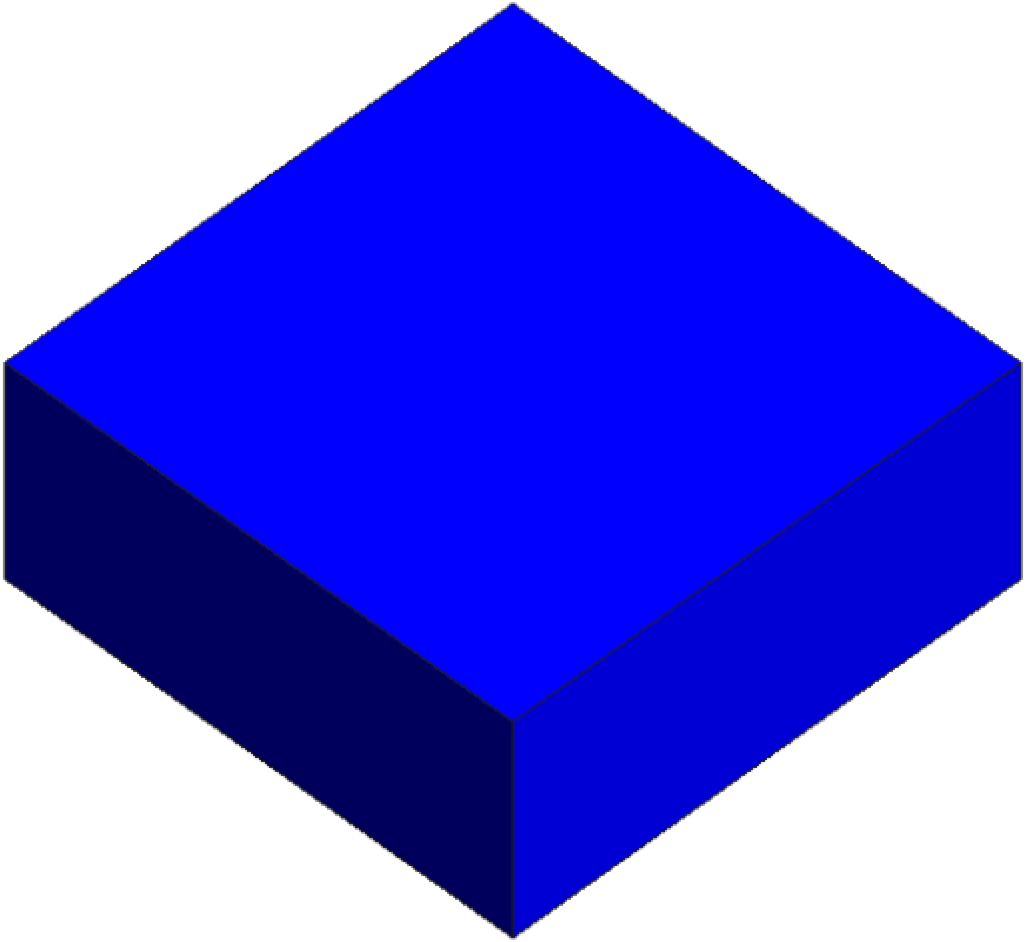

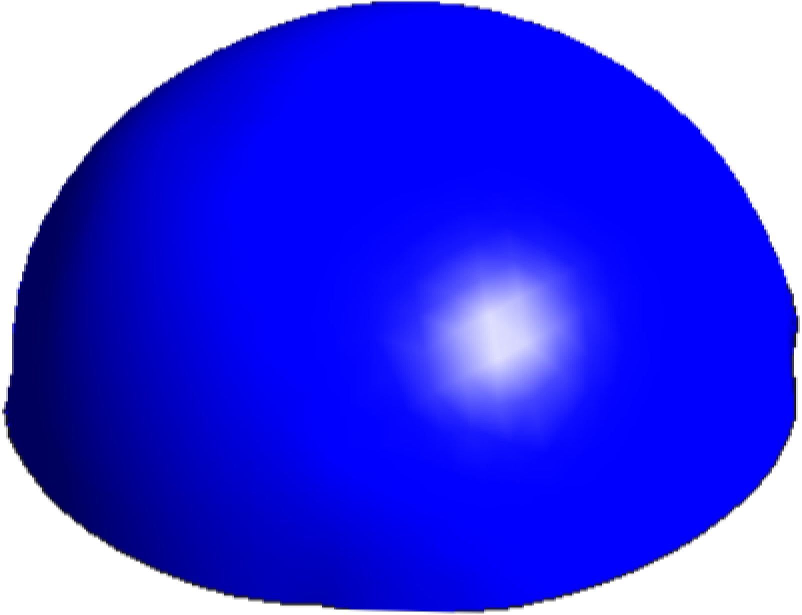

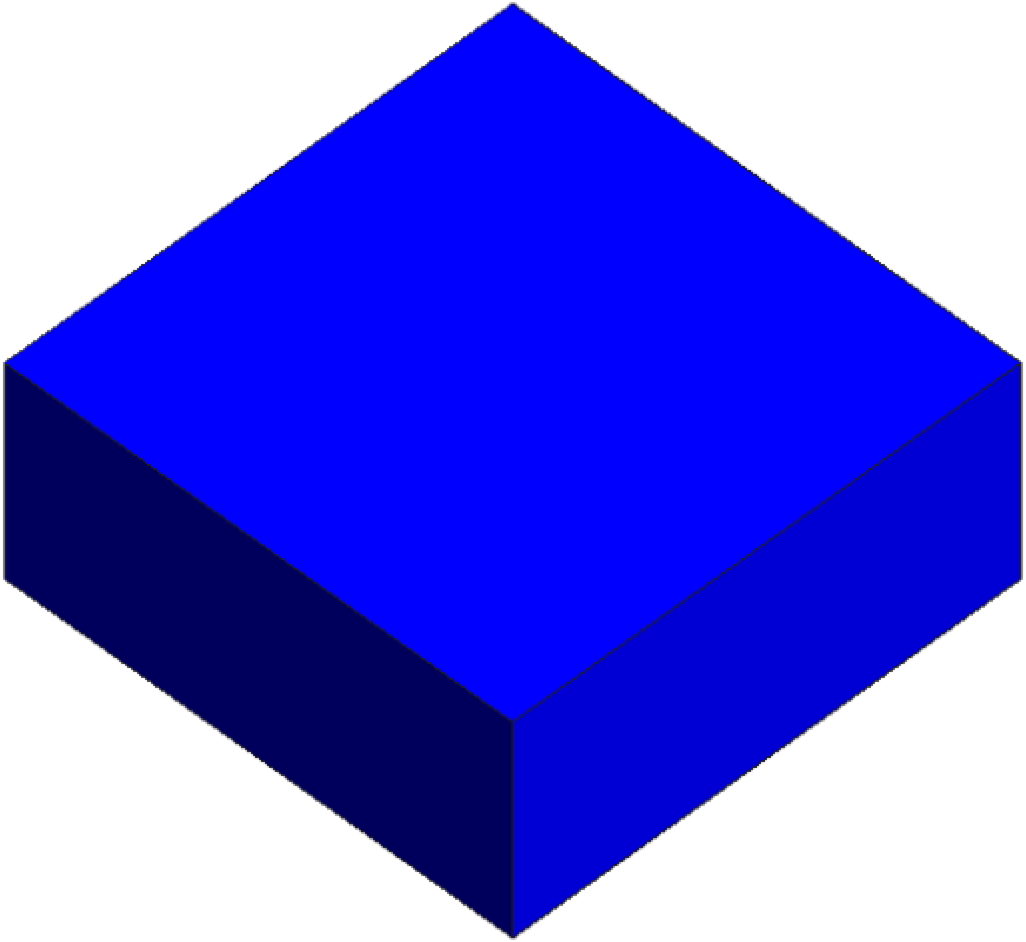

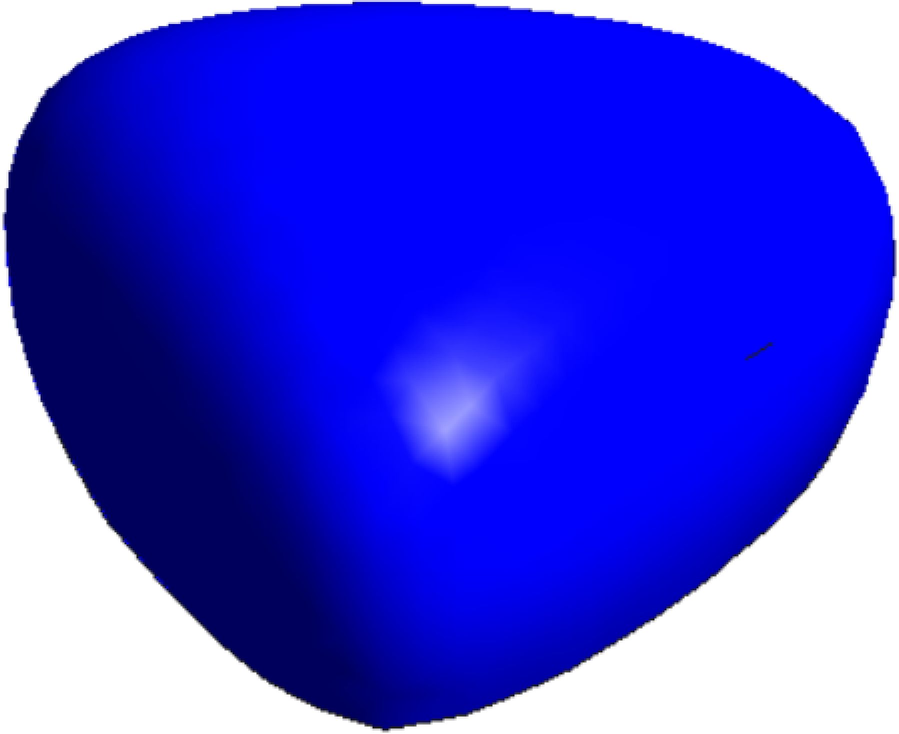

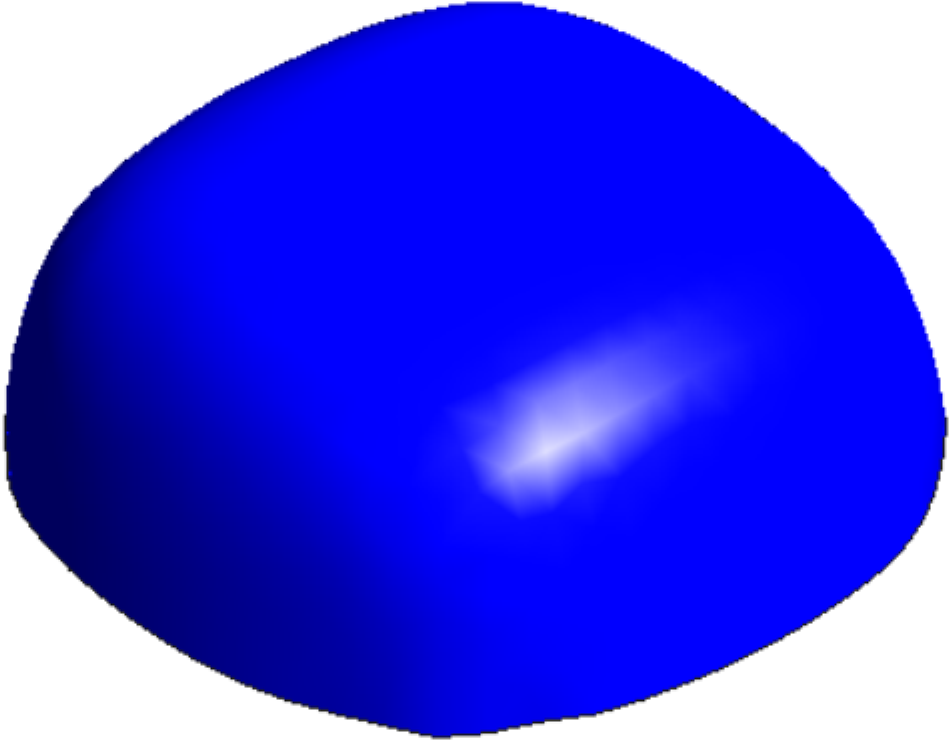

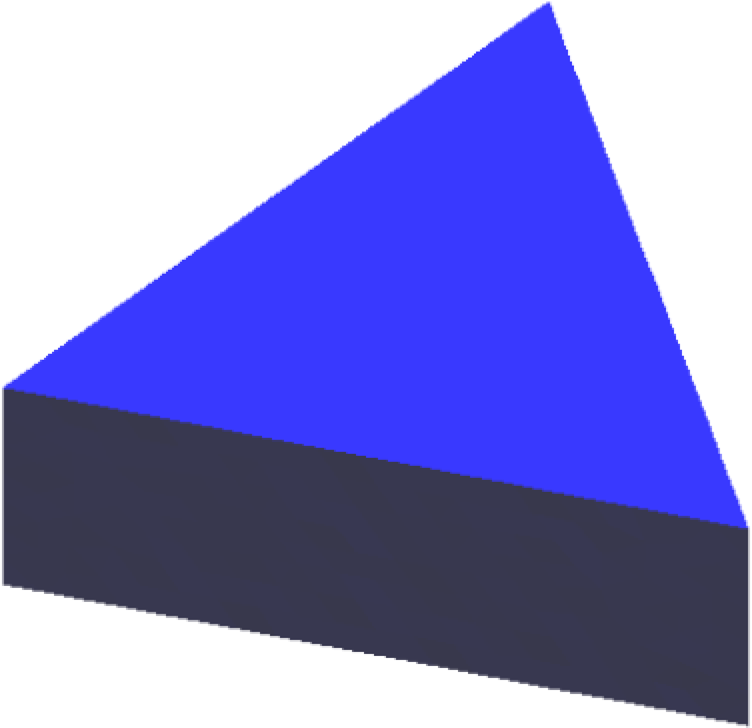

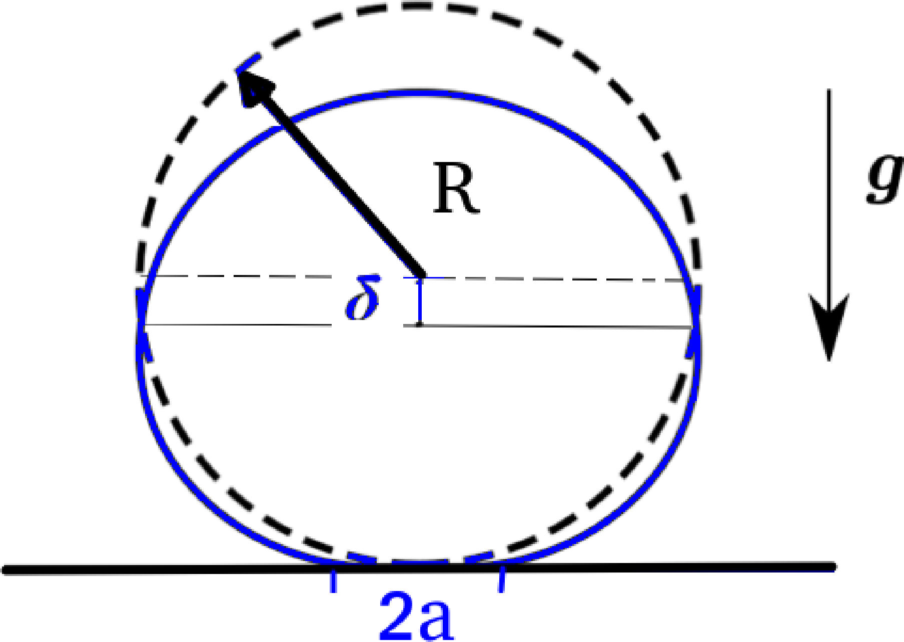
R
δ
2a
g

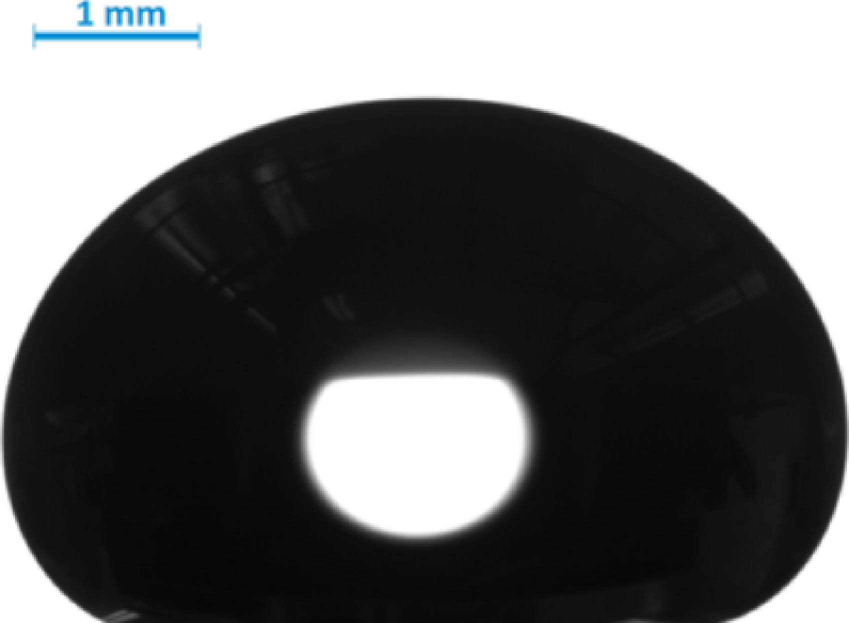
1 mm

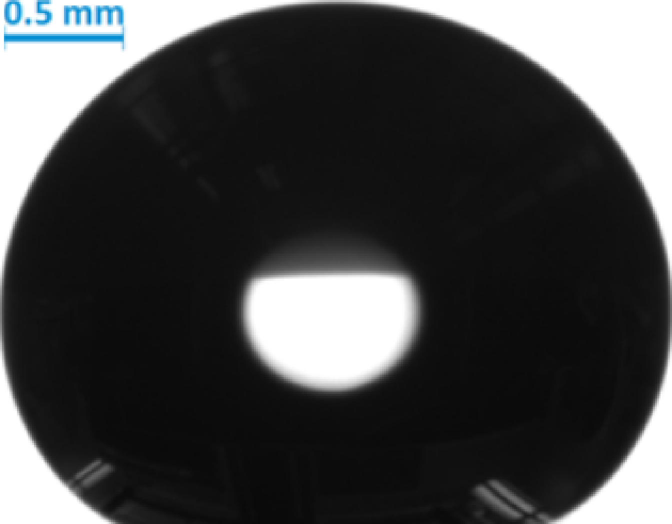
0.5 mm

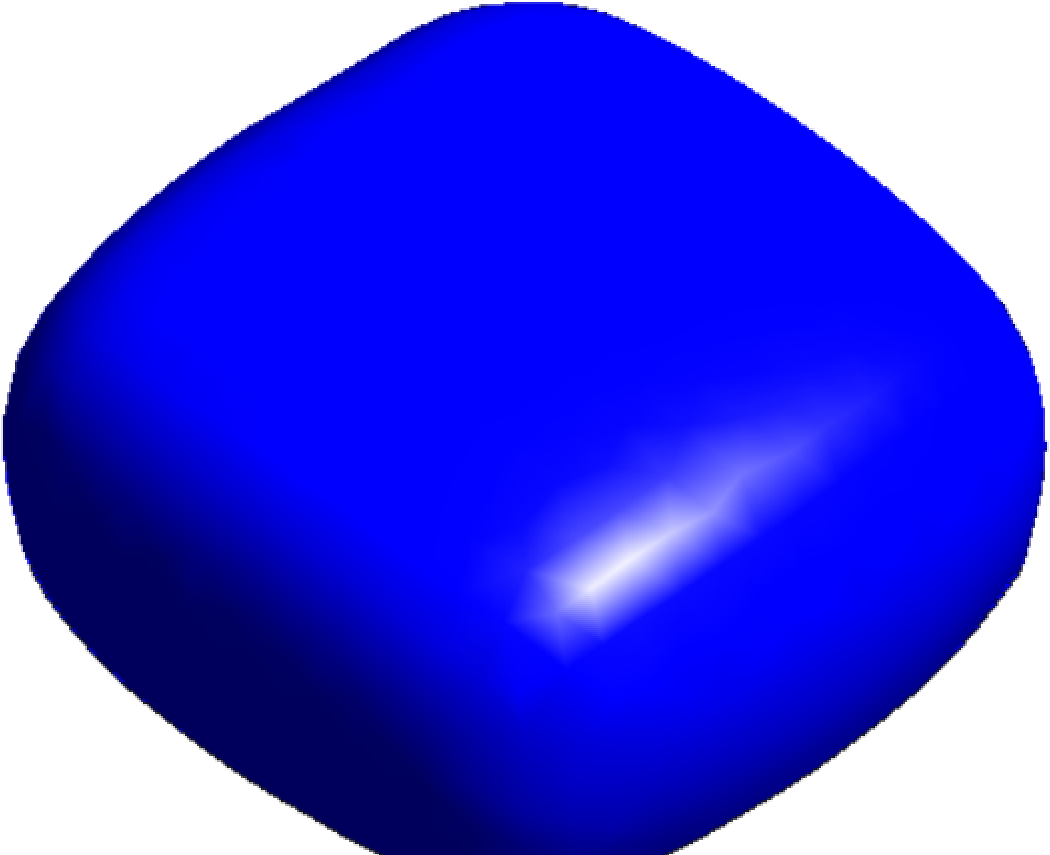

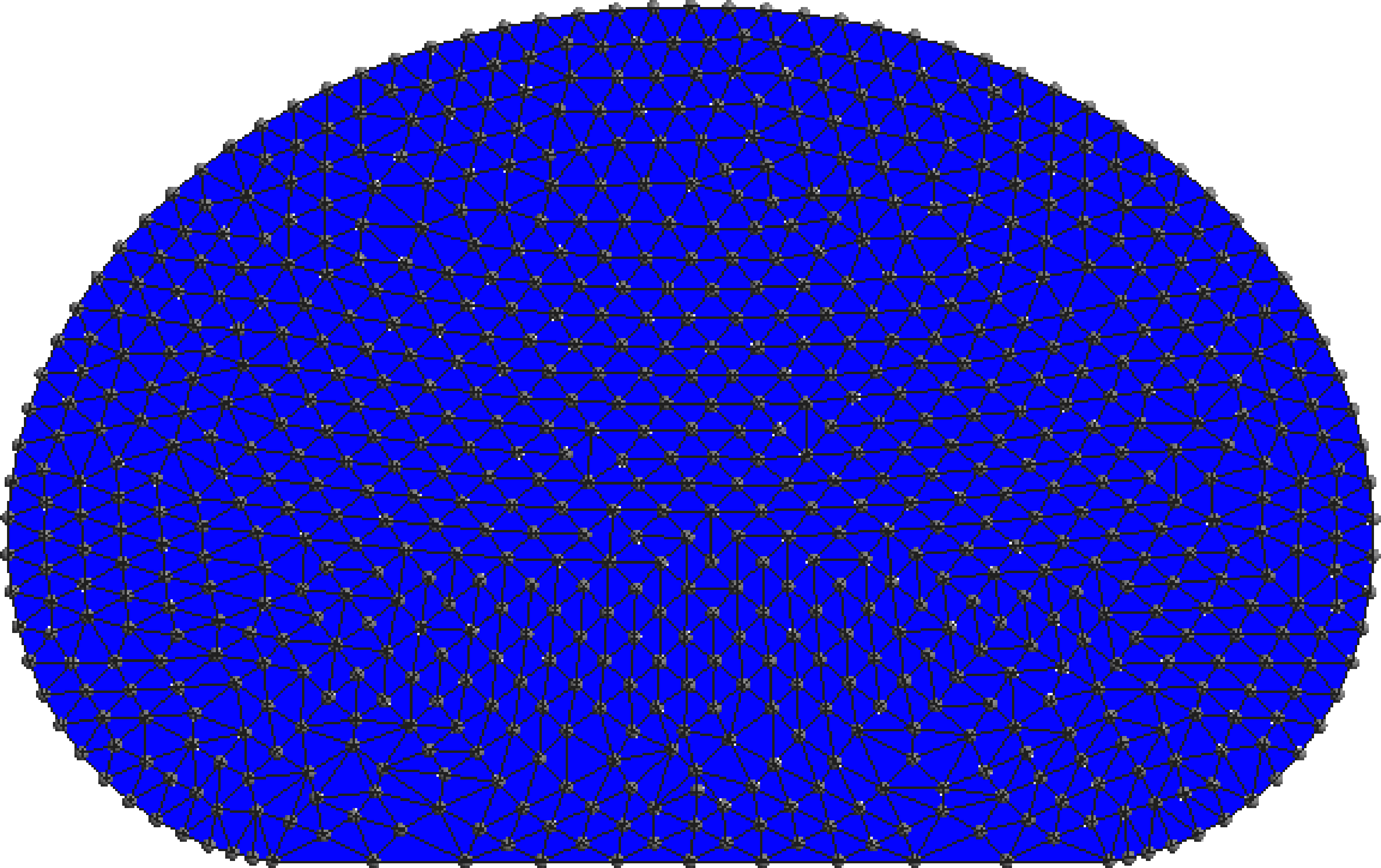

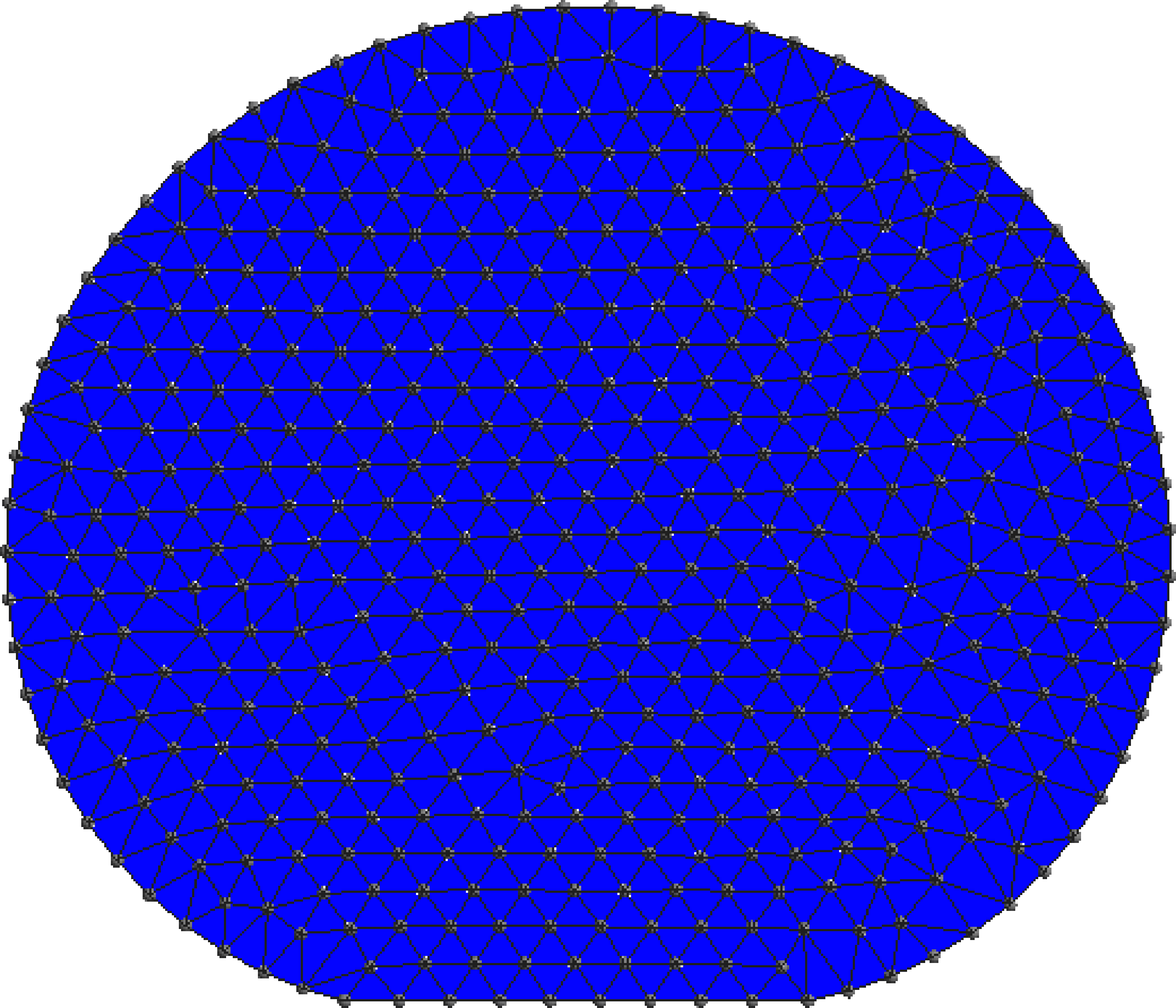

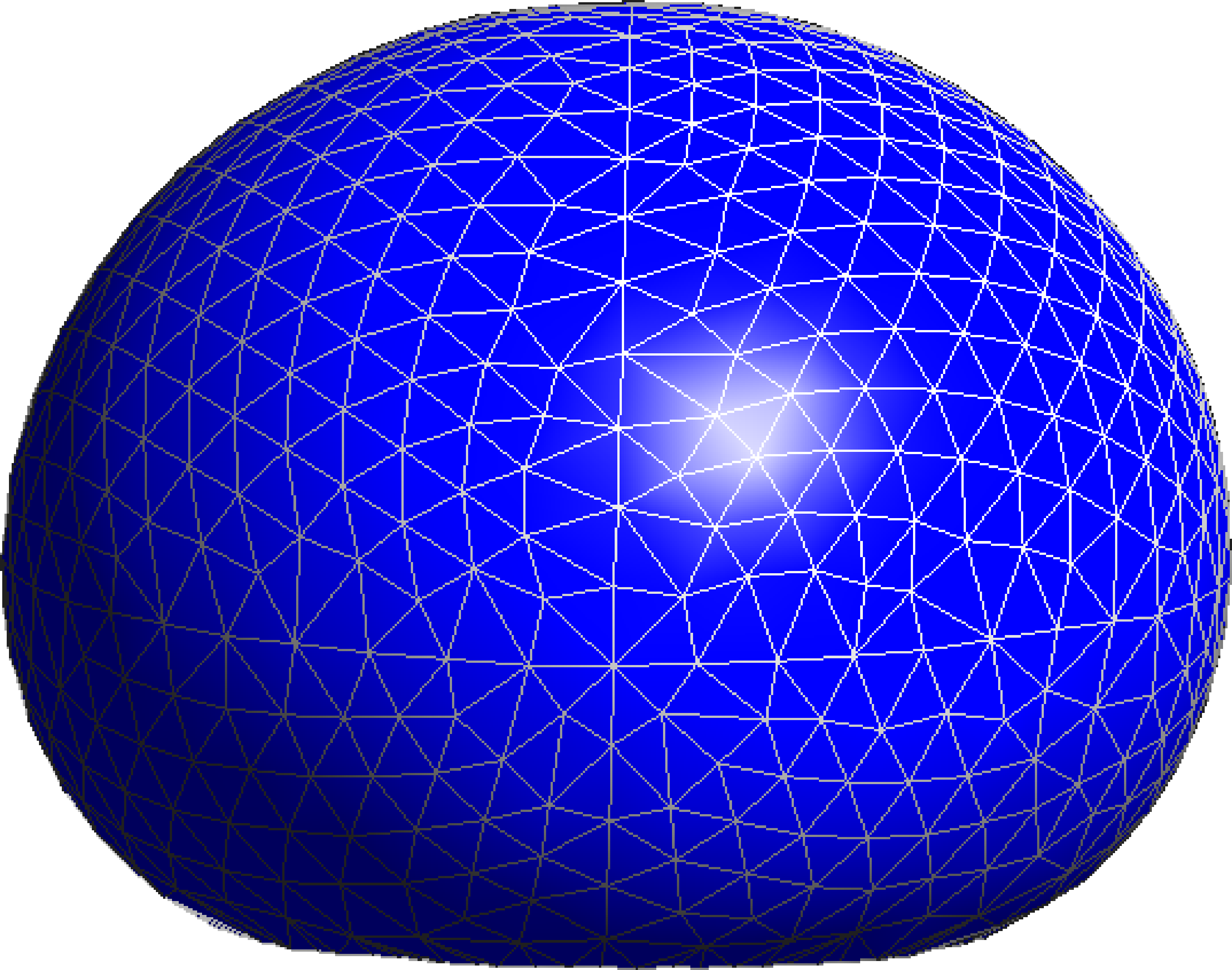

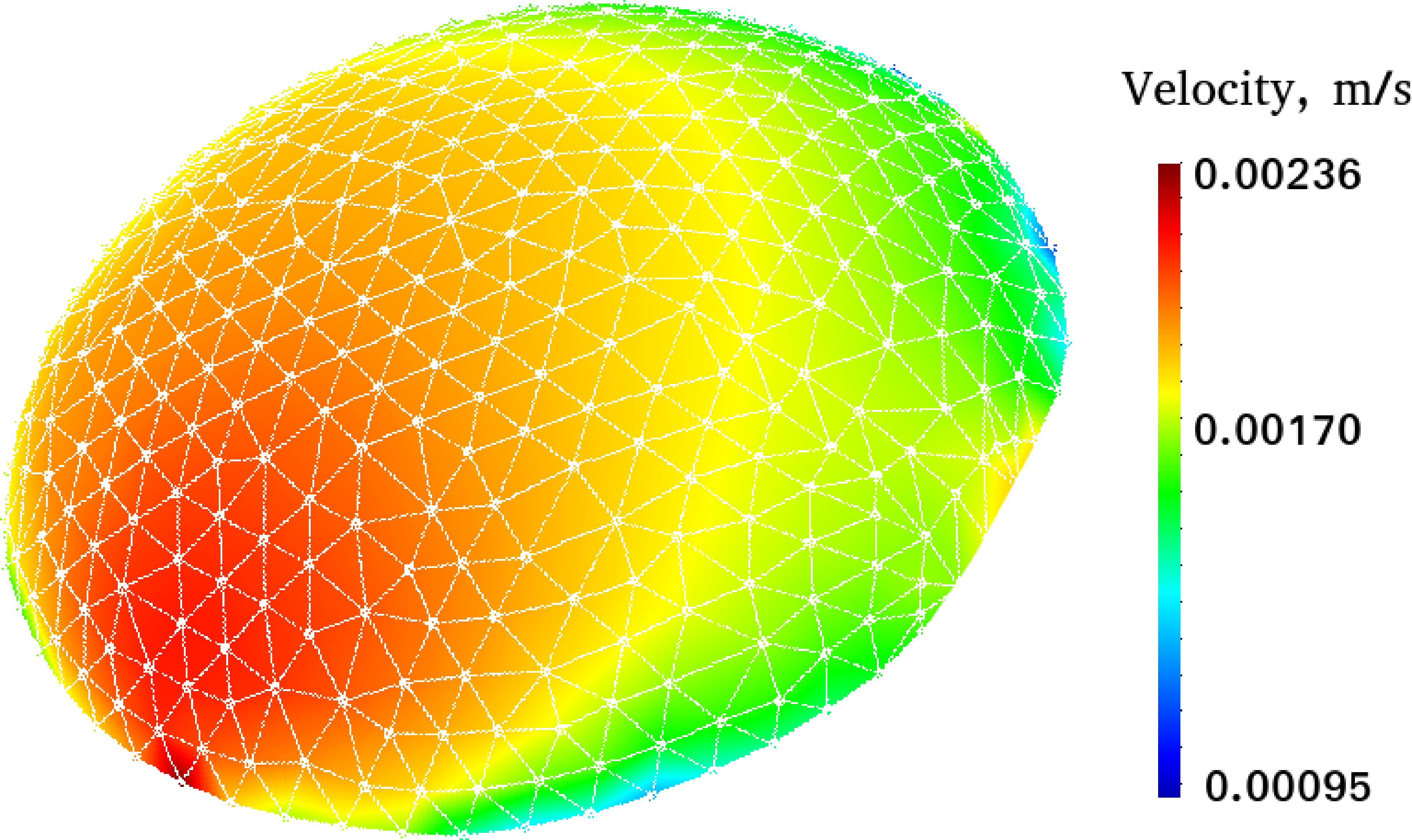
Velocity, m/s
0.00236
0.00170
0.00095

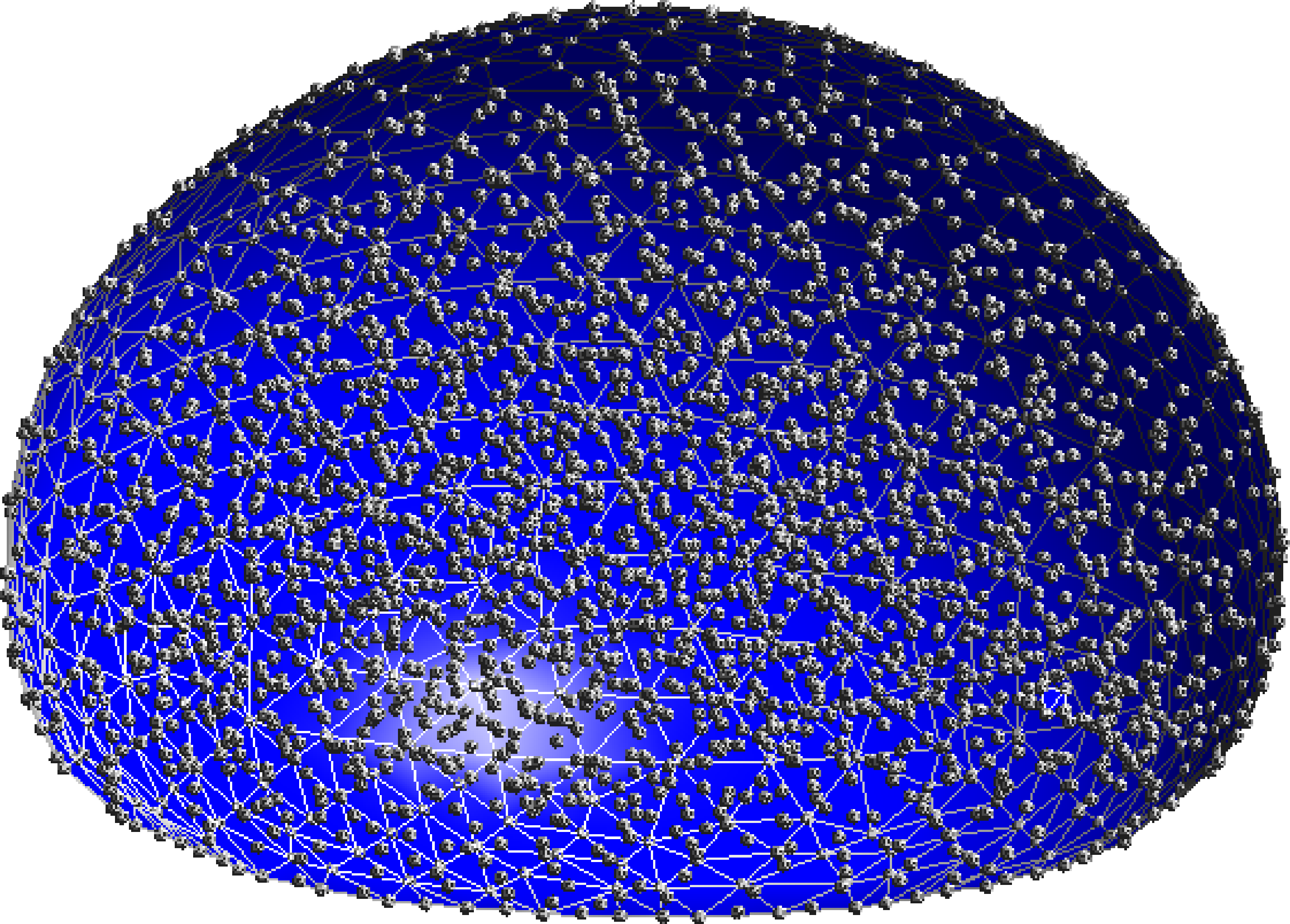

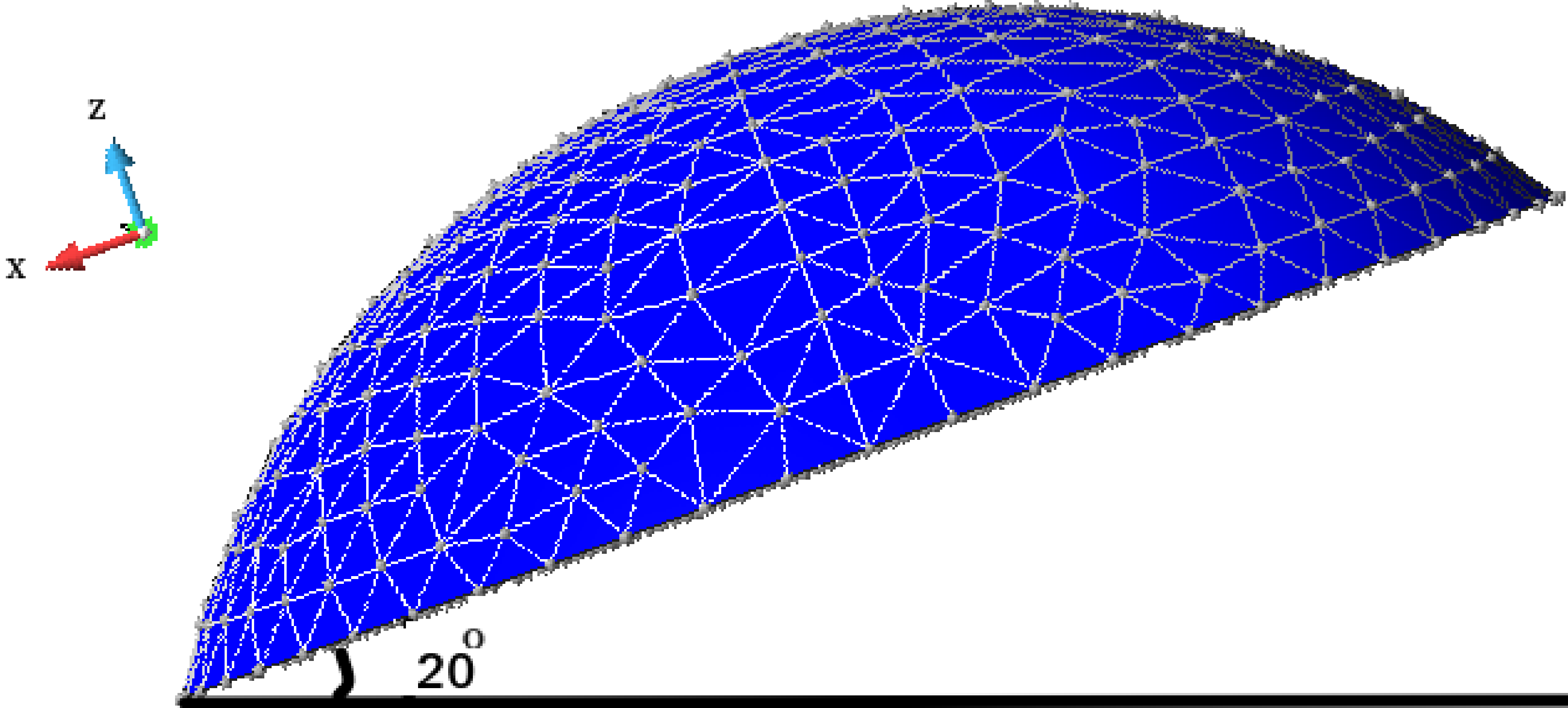
Z
X
20o

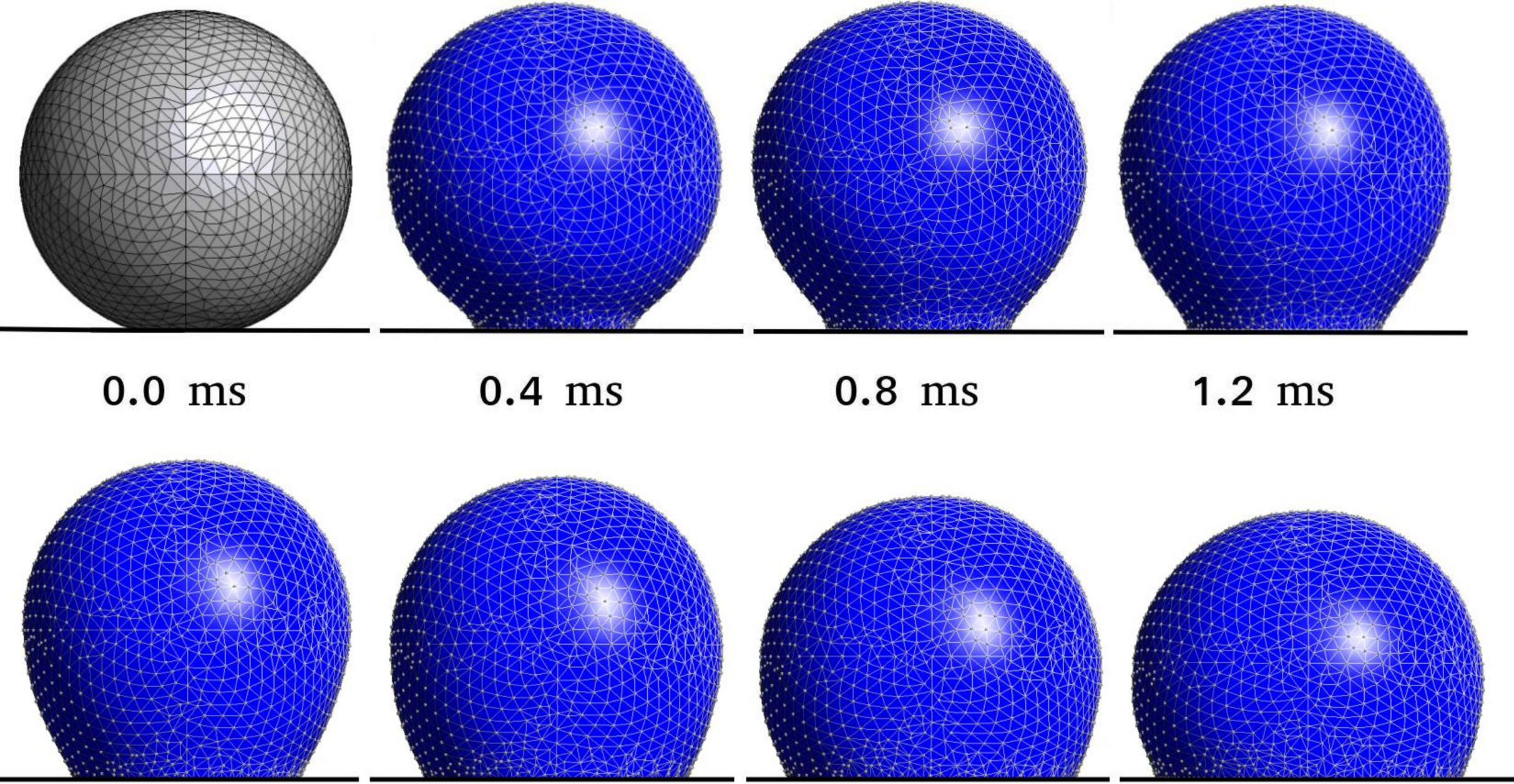

0.0 ms 0.4 ms 0.8 ms 1.2 ms

2.3 ms 3.7 ms 5.0 ms 6.3 ms

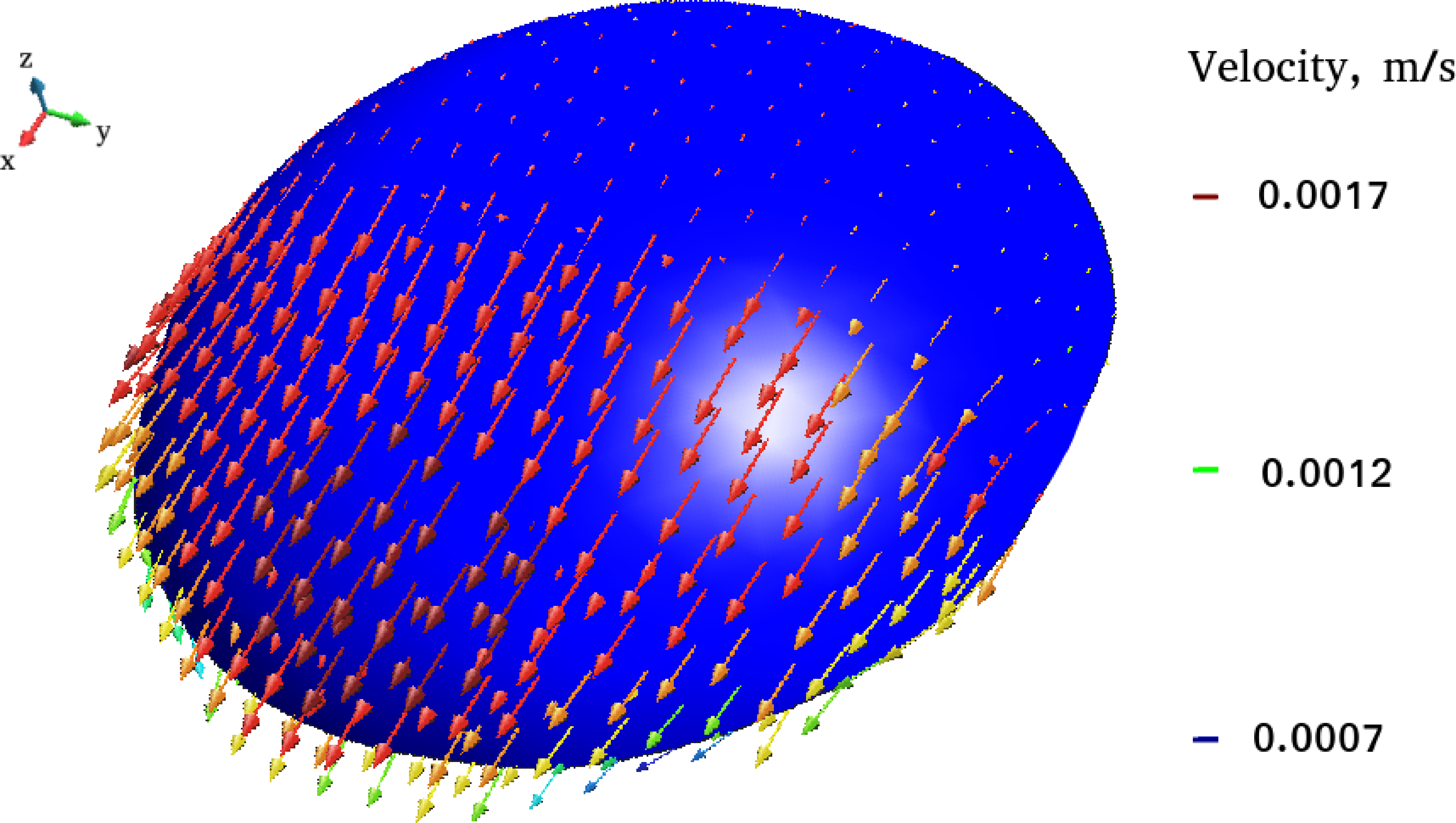
z
y
x
Velocity, m/s
0.0017
0.0012
0.0007

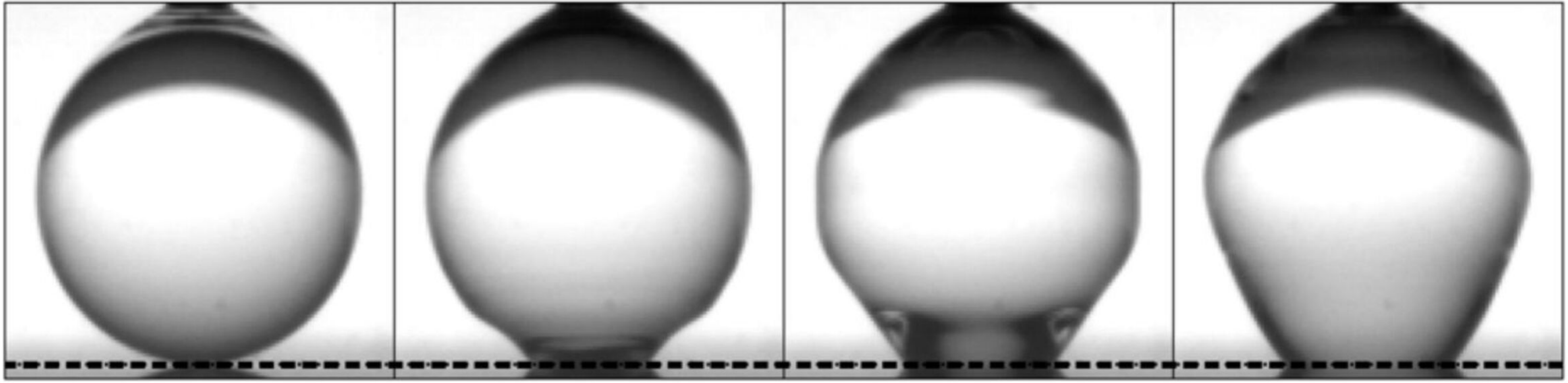
0.0 ms
0.4 ms
0.8 ms
1.2 ms

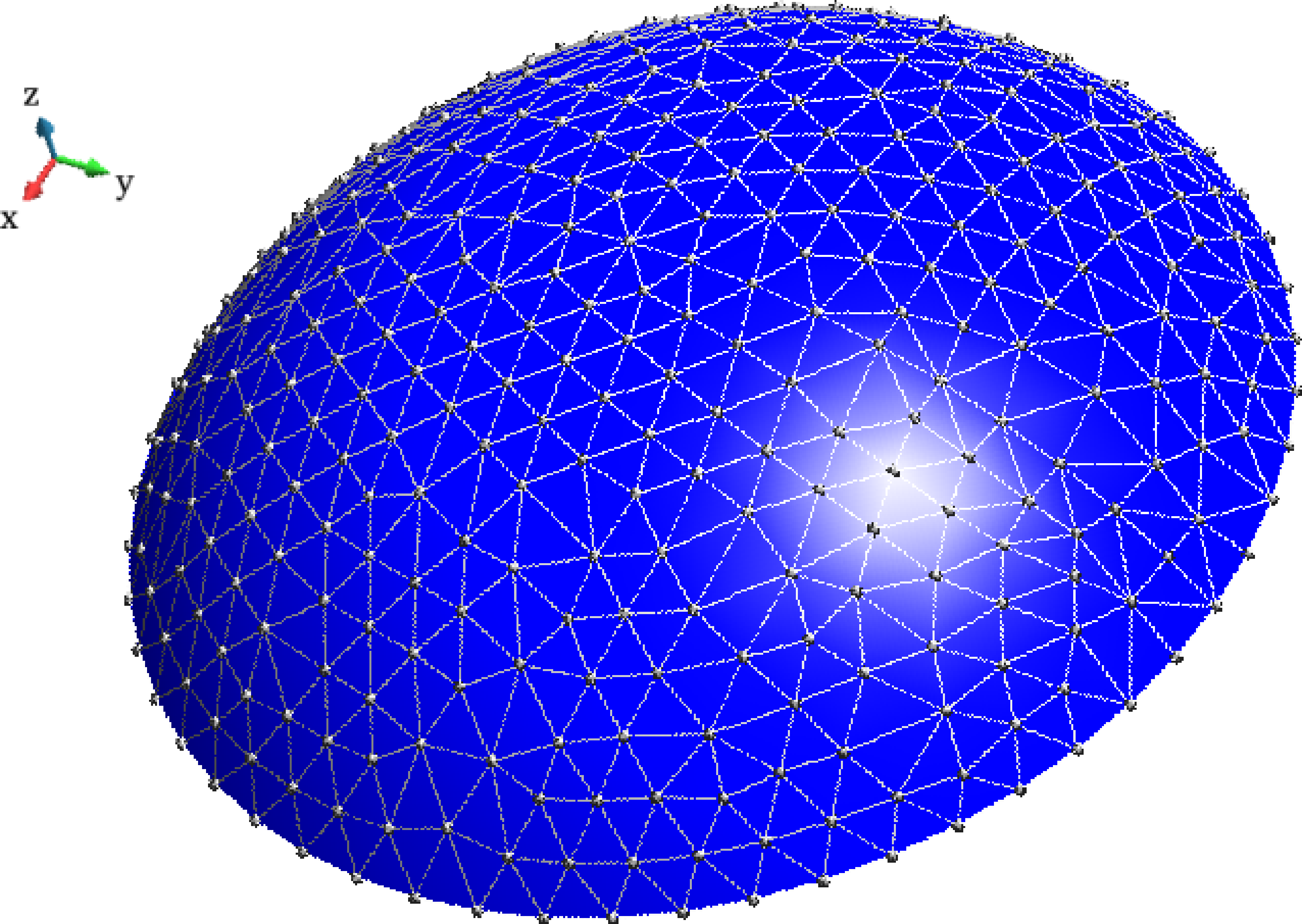
z
y
x

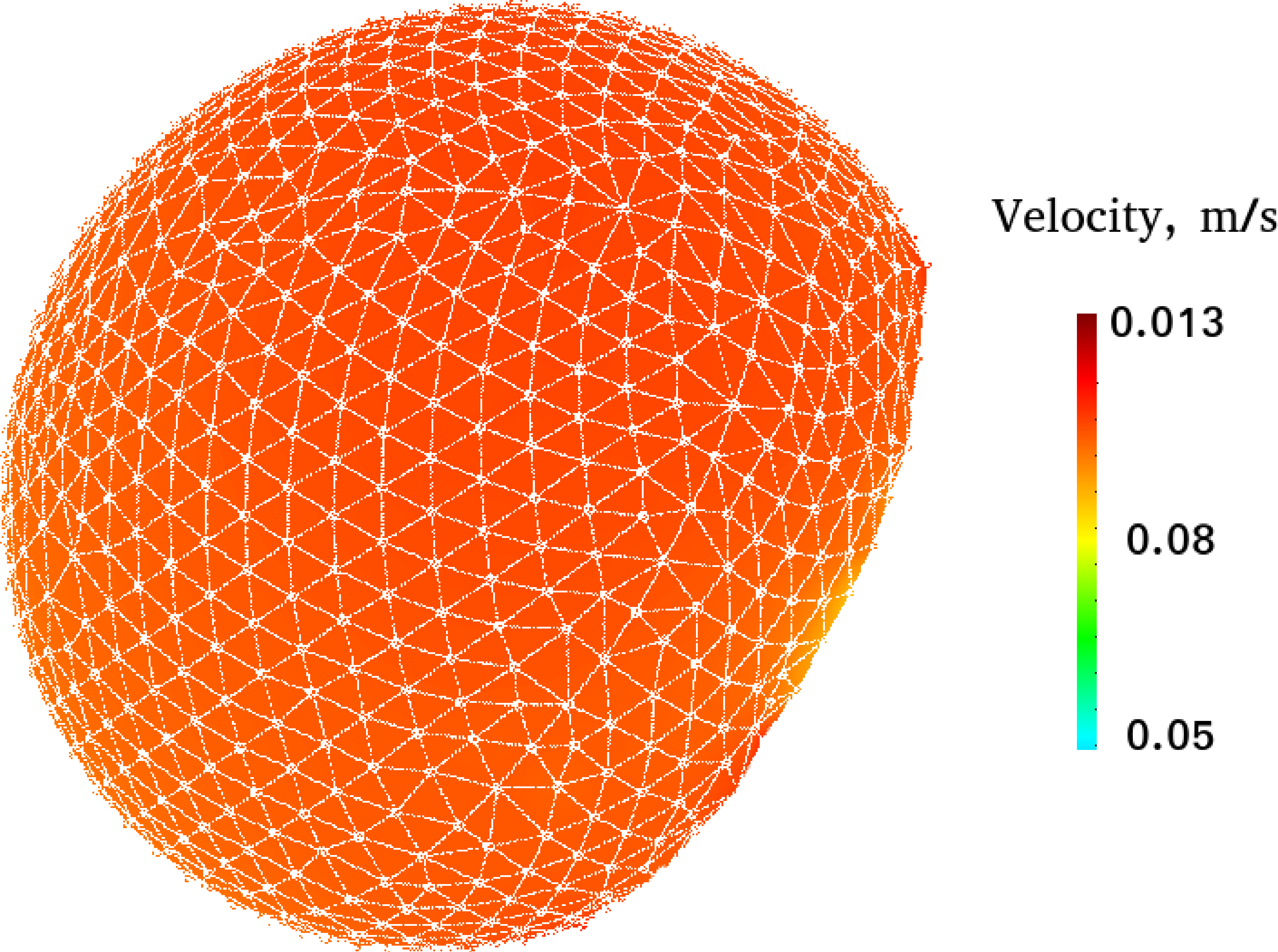
Velocity, m/s
0.013
0.08
0.05

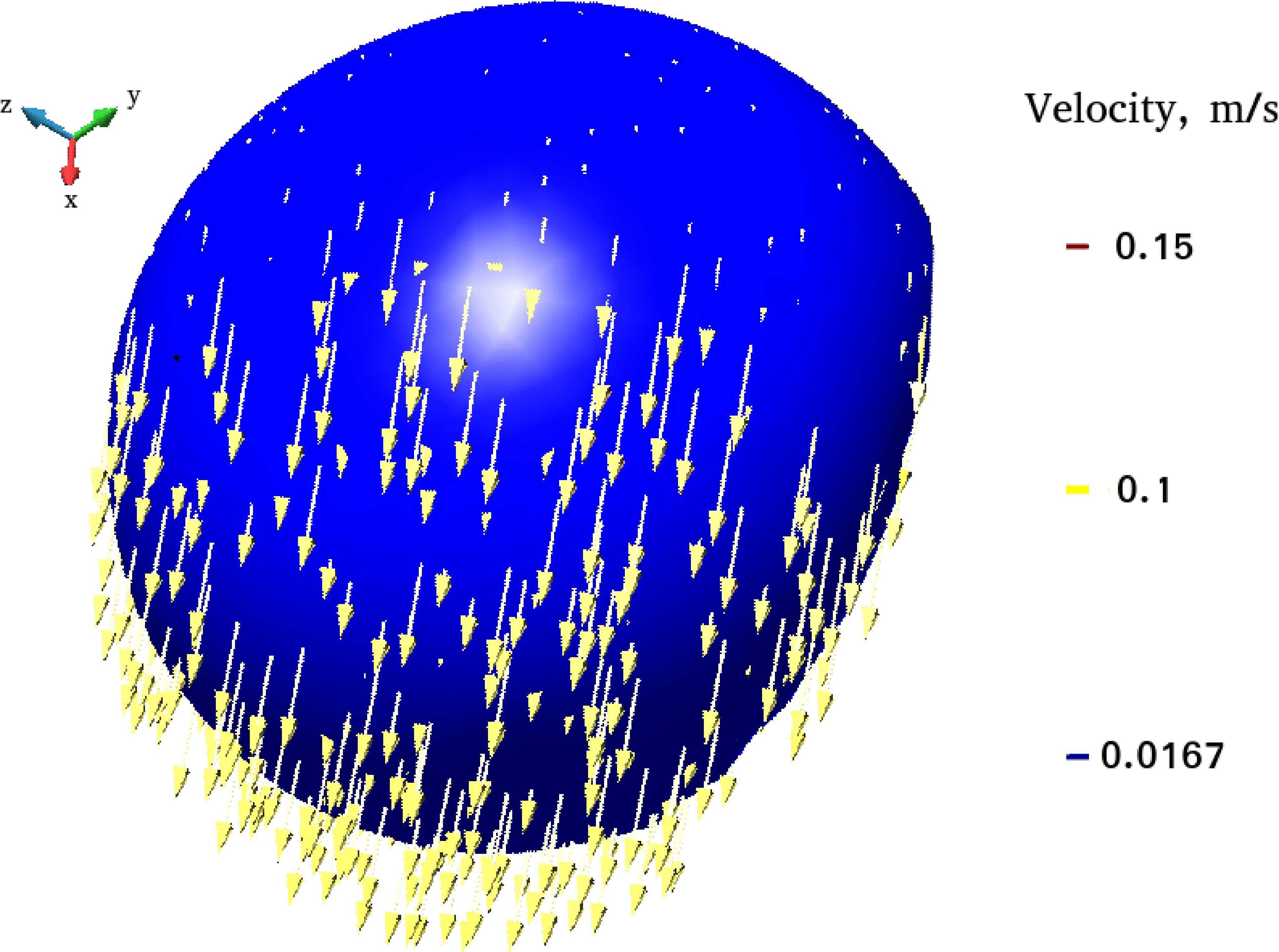
z
y
x
Velocity, m/s
0.15
0.1
0.0167

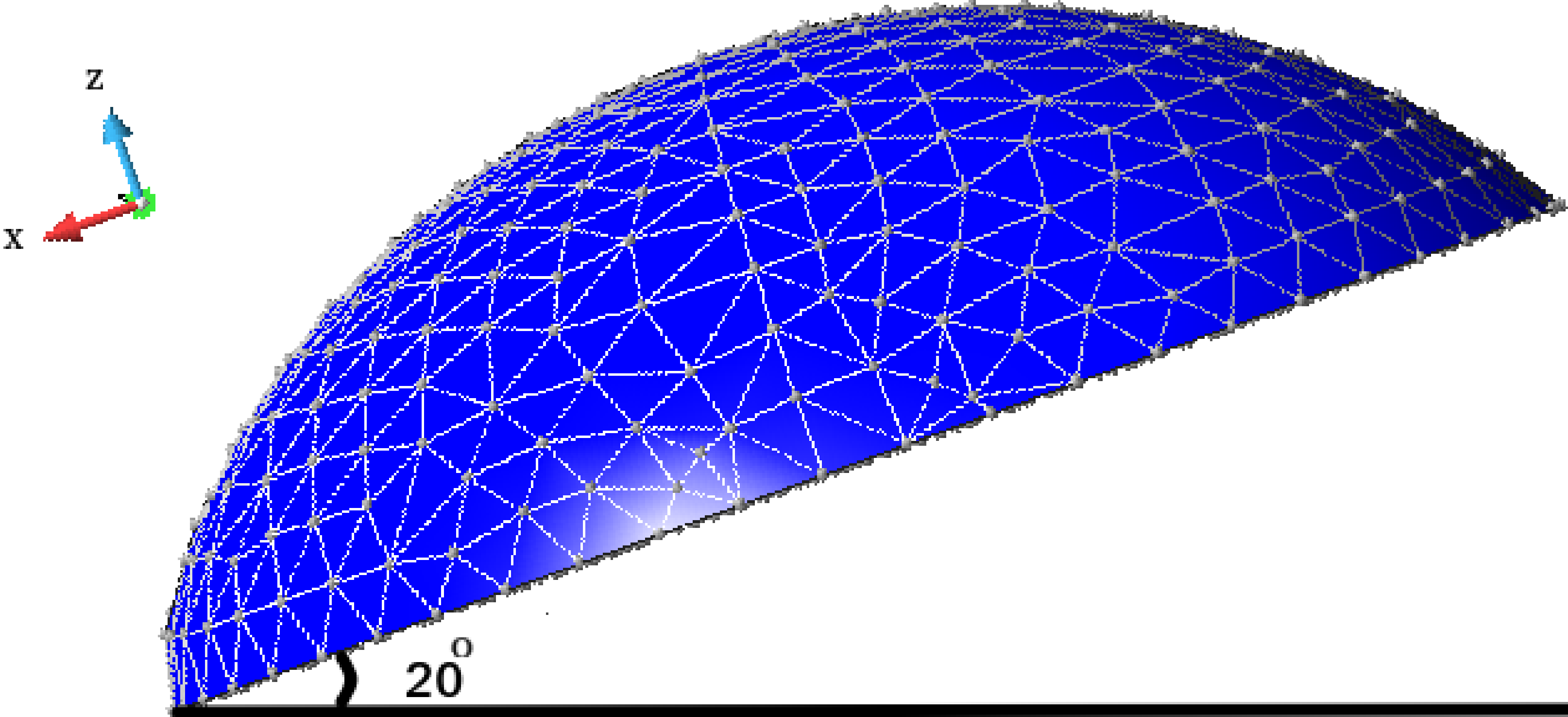
Z
X
20°

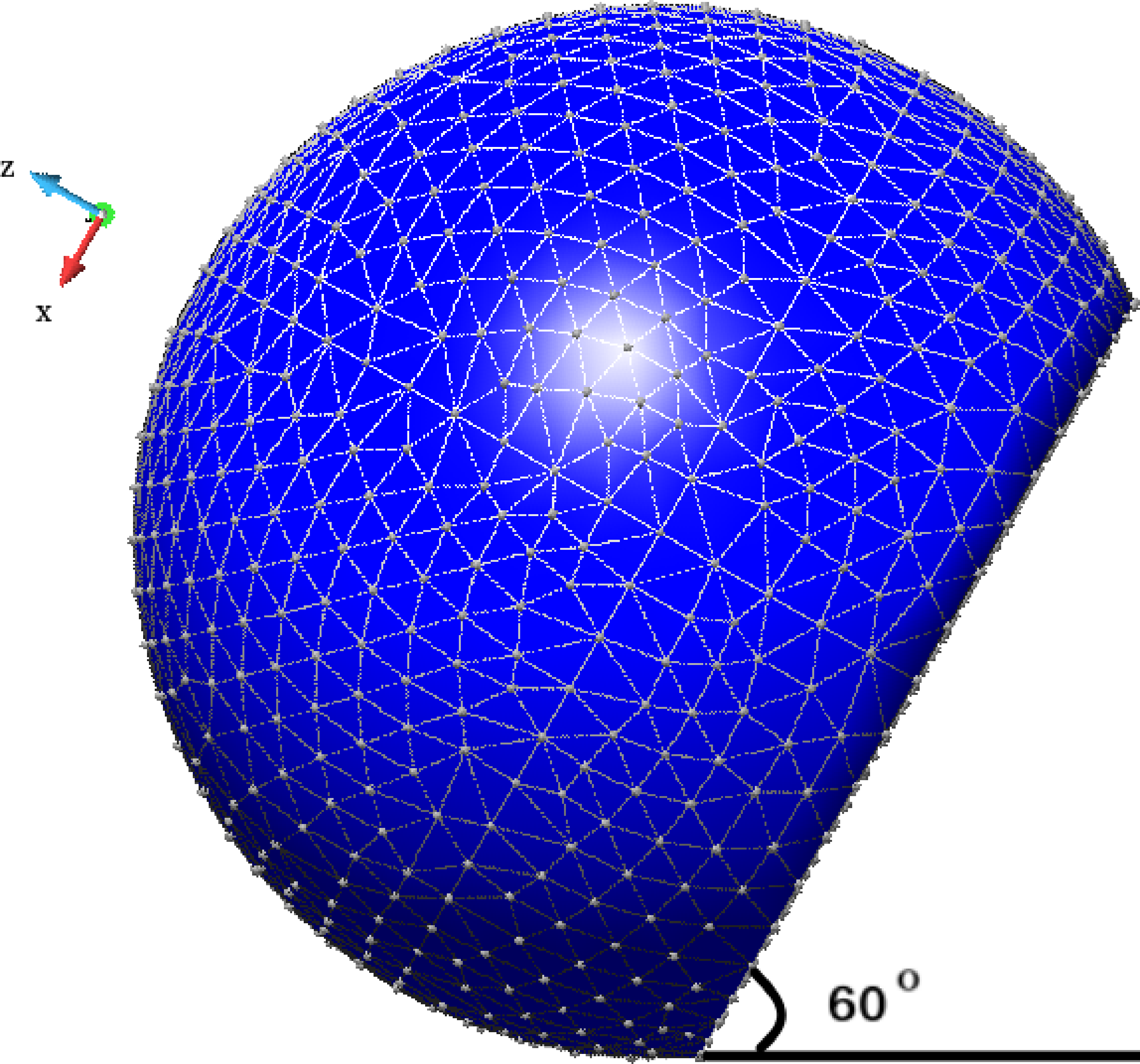
Z
X
60 °

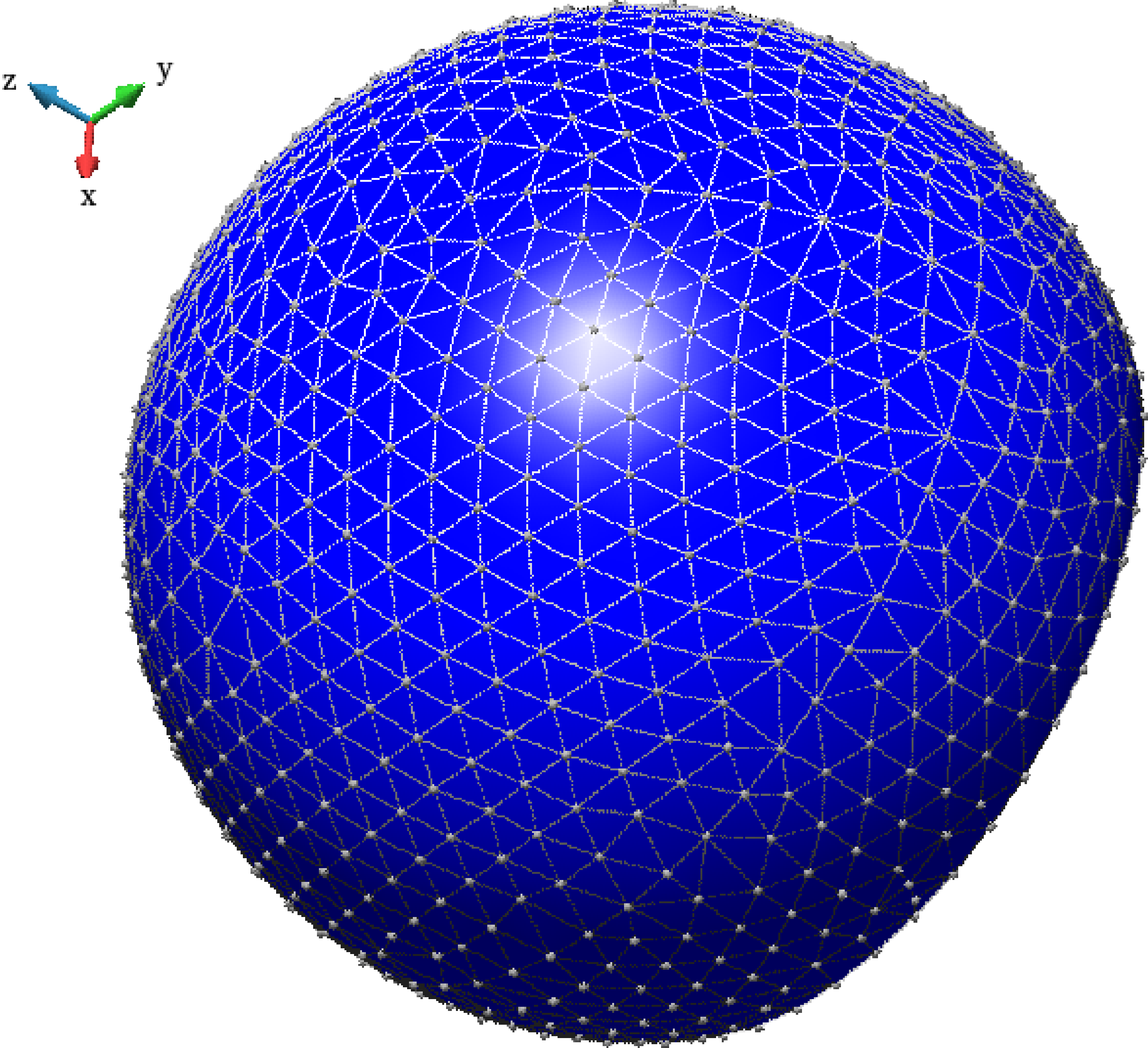
z
y
x

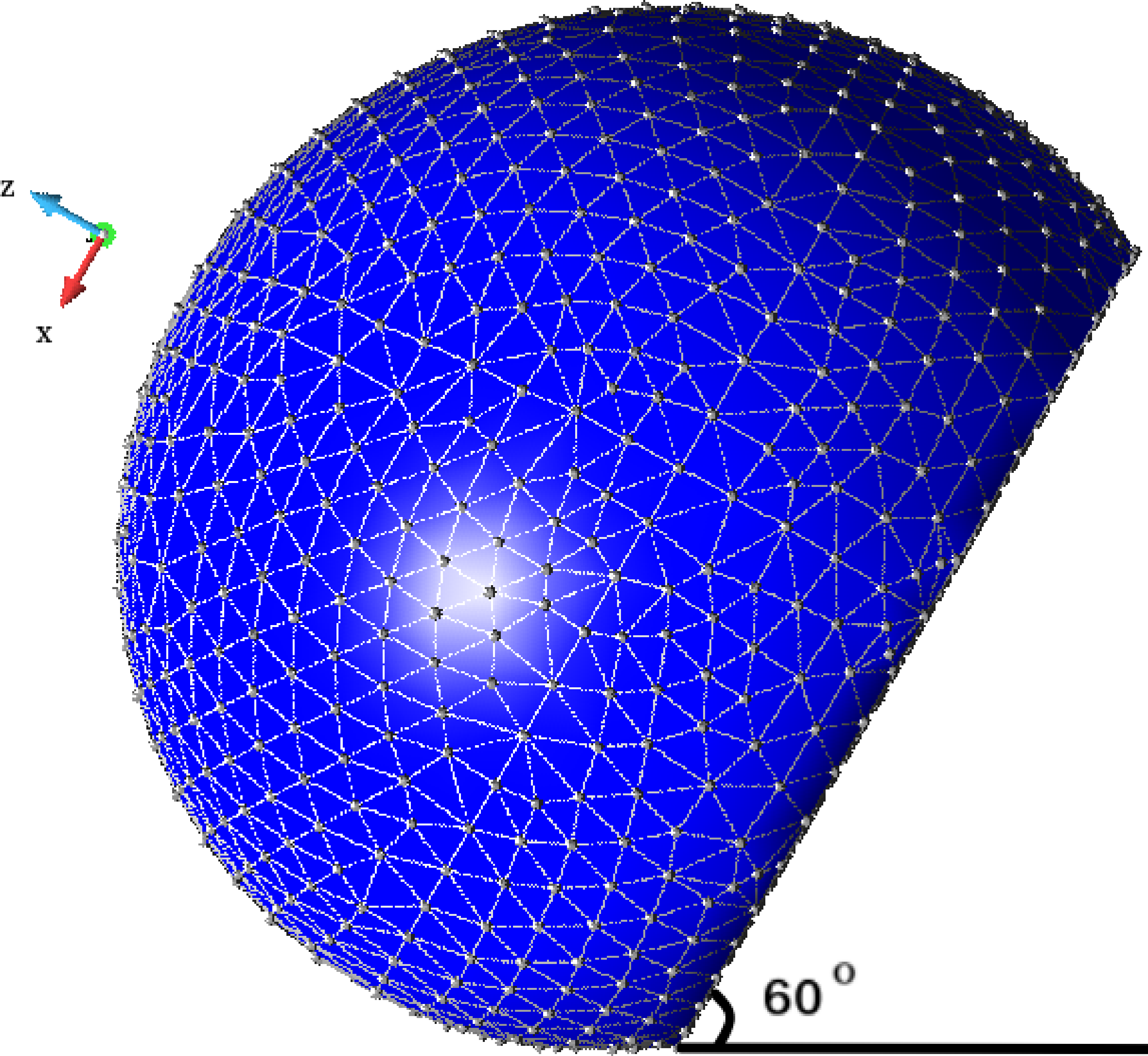
z
x
60 °

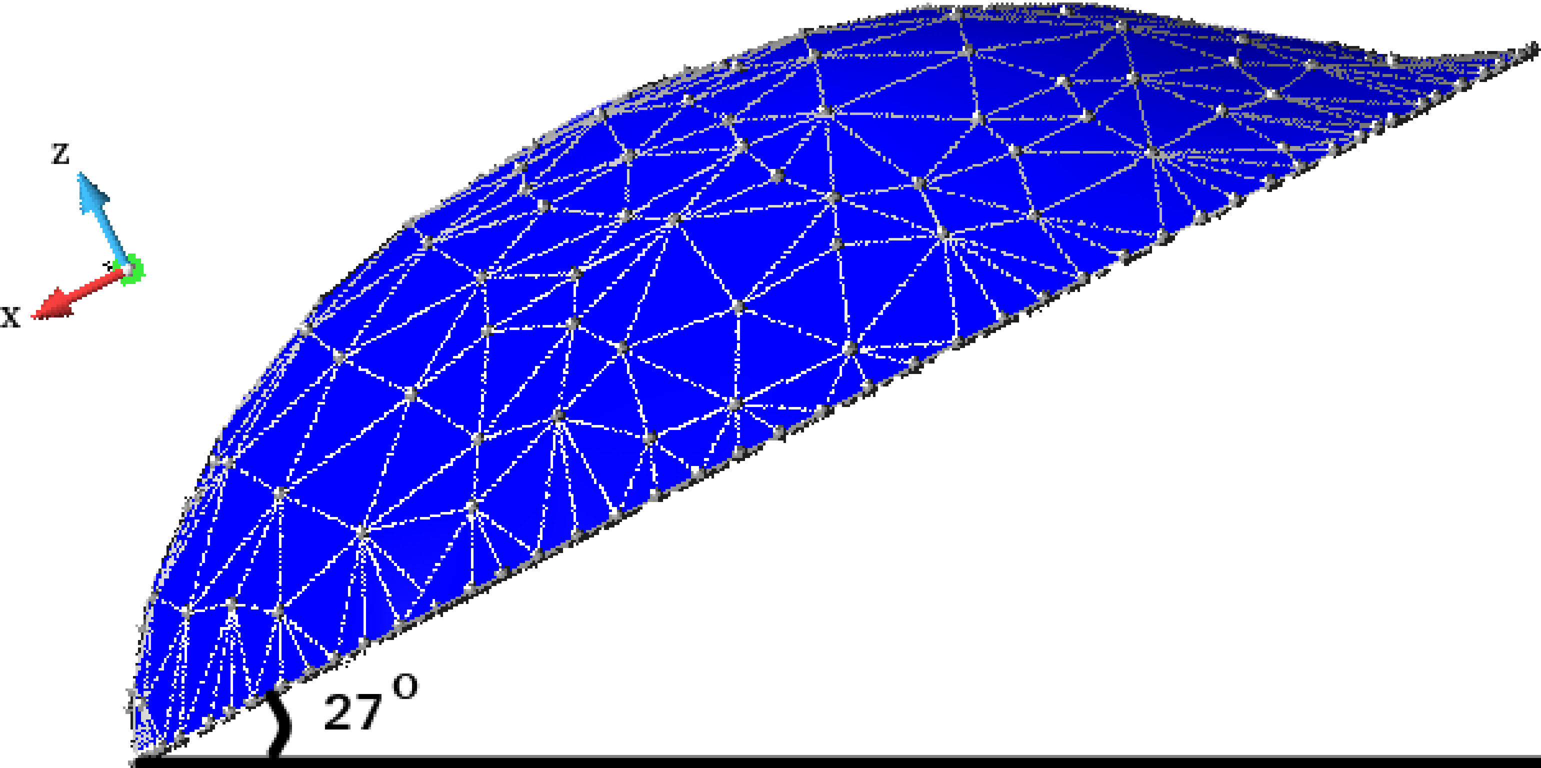
Z
X
27°

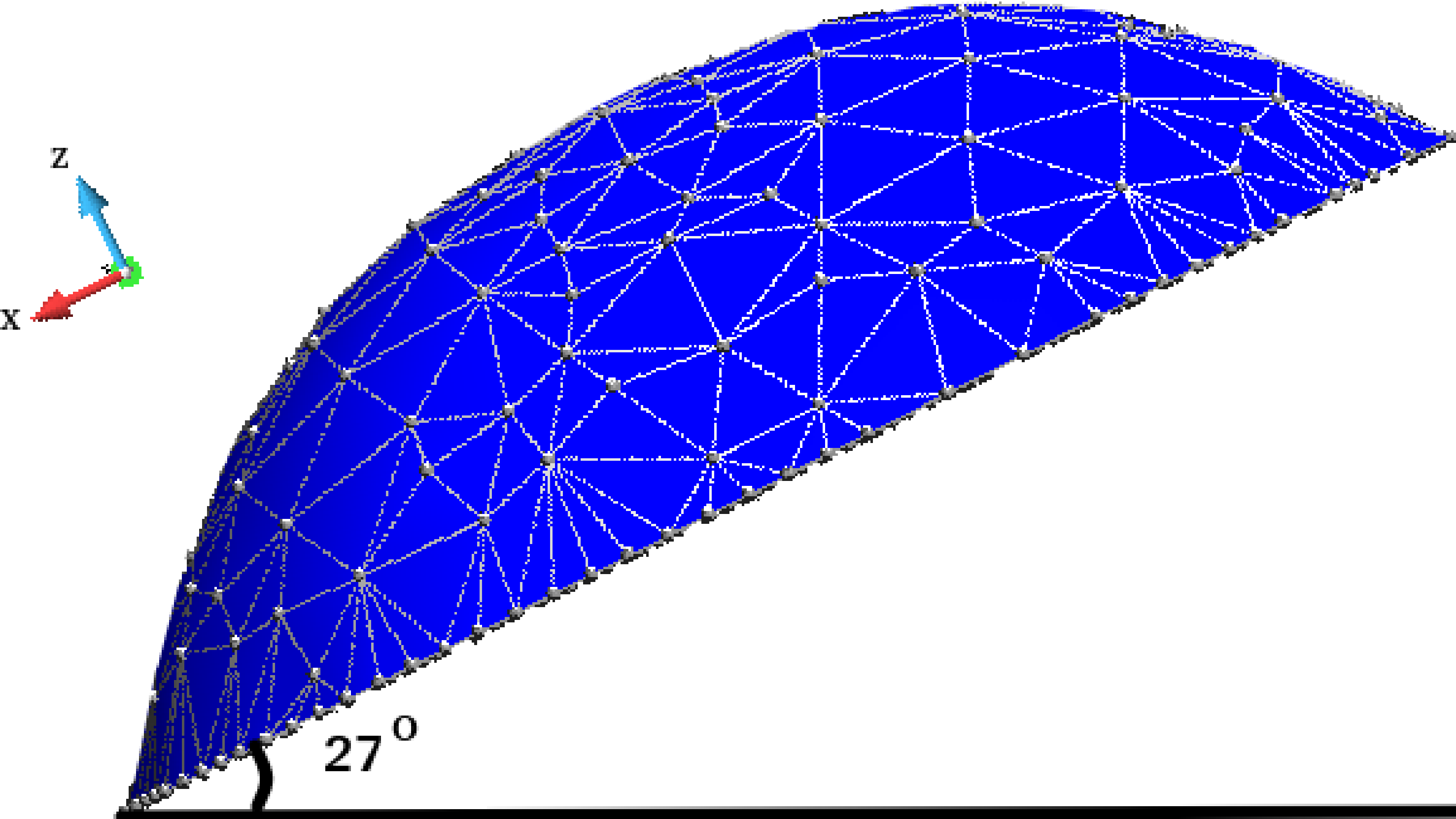
Z
X
27°

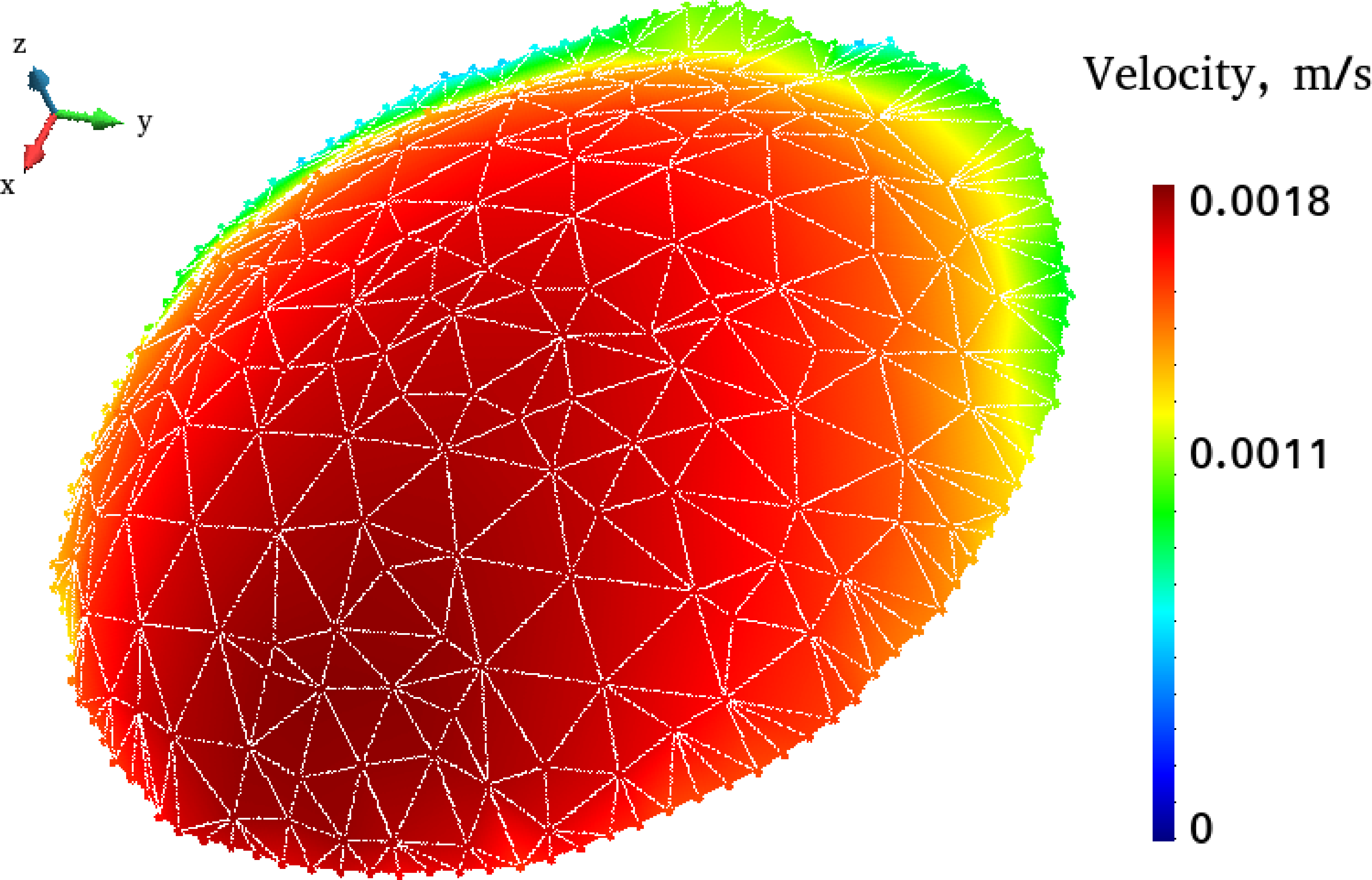
z
y
x
Velocity, m/s
0.0018
0.0011
0

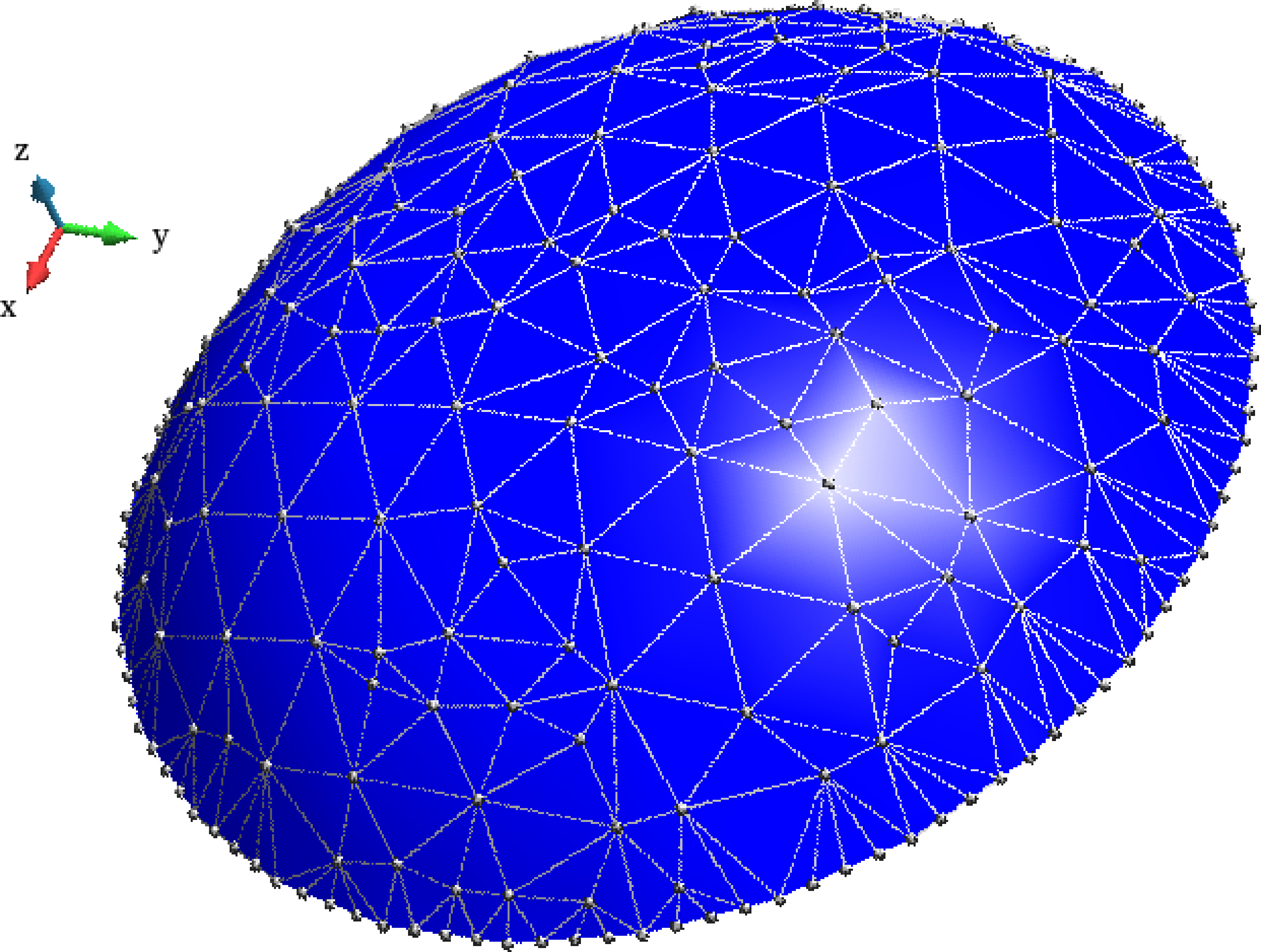
z
y
x

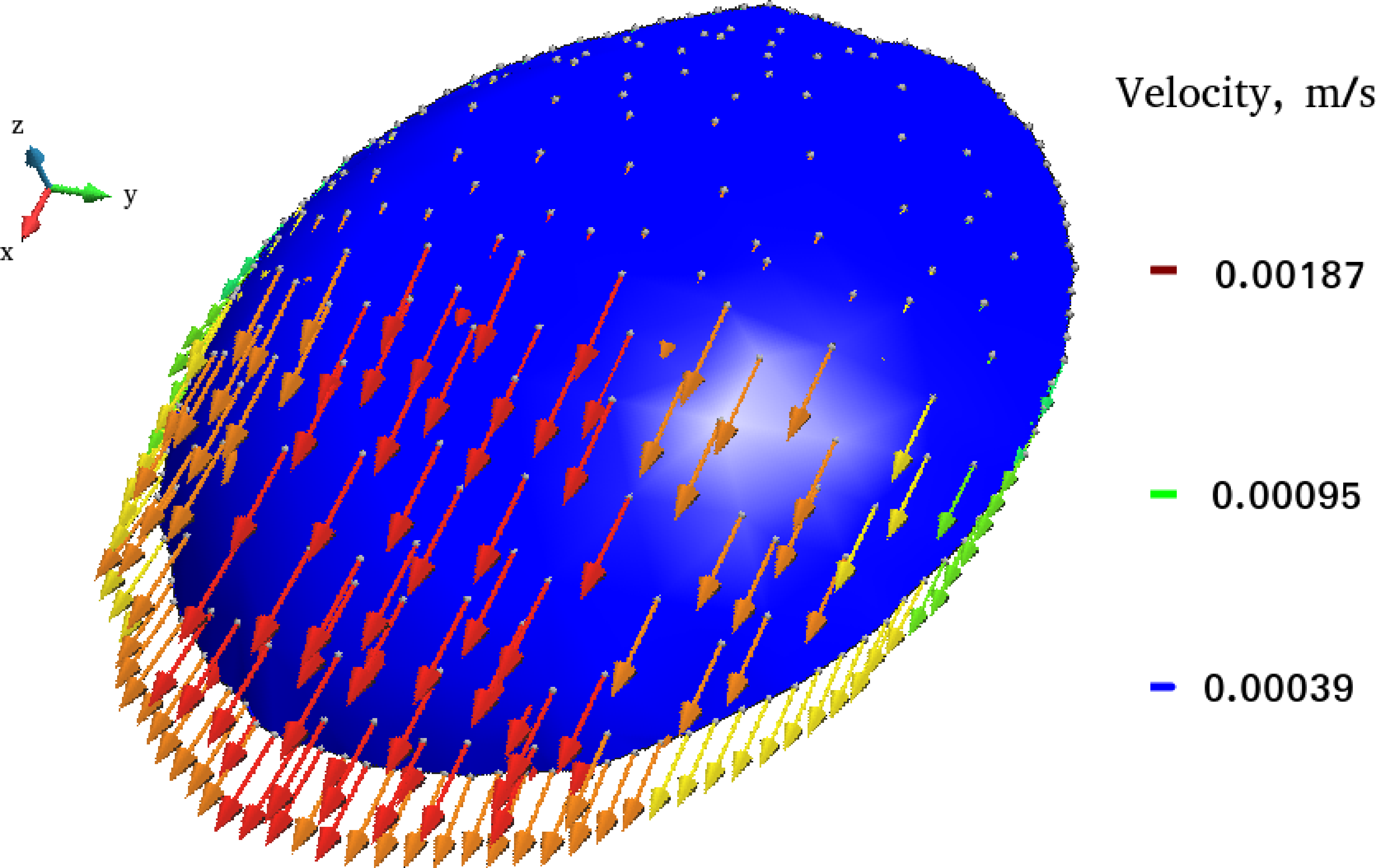
z
y
x
Velocity, m/s
0.00187
0.00095
0.00039

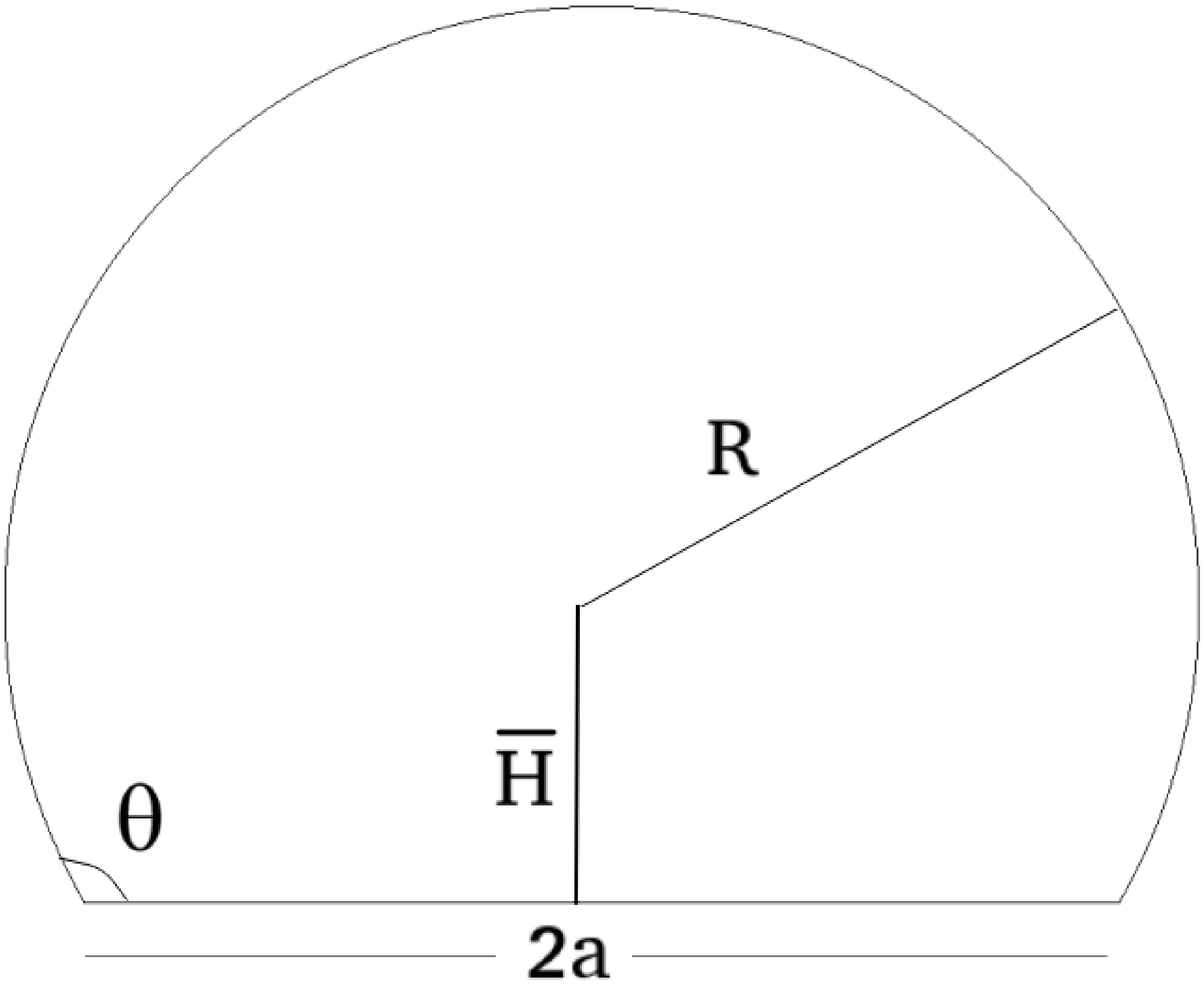
R
$\bar{H}$
θ
2a

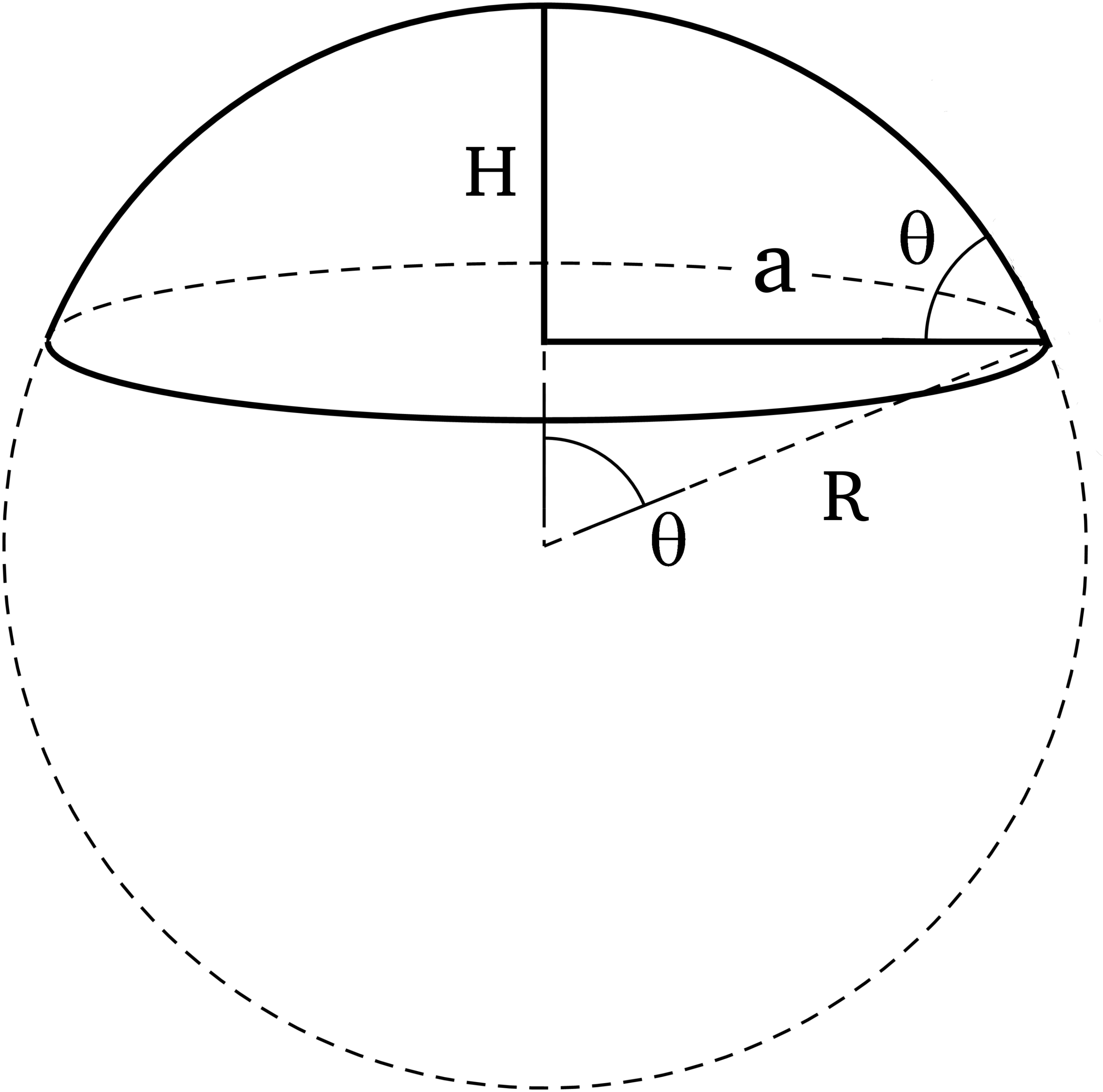
H
θ
a
R
θ